CFD BASED MICROSCALE NUMERICAL STUDIES OF OIL SEPARATION FROM SAND PARTICLES

by

Xiaomeng Li

A thesis submitted in partial fulfillment of the requirements for the degree of

Master of Science

in

Chemical Engineering

Department of Chemical and Materials Engineering
University of Alberta

Abstract

This work is devoted to CFD-based numerical studies of oil separation from sand particles under the influence of water flow velocity. A single micro-scale (diameter of 100nm) particle is covered by a thin oil film which is immersed in a uniform flow. The oil-particle separation has been modeled at different contact angles of 0^o, 90^o, 170^o and different Reynolds numbers of 1, 3, 5, 7, 10, 20, 100, 150, 200. Different Reynolds number (Re) indicates different inlet velocities, meanwhile, different contact angles indicate different hydrophobicities. The desired status is when the oil completely moves away from the particle. A commercial computational fluid dynamics (CFD) software called ANSYS Fluent 14.5 [1] is used to perform all modeling works. Applied to the micro-scale modeling, Volume of Fluid (VOF) serves as the major method. This work is unique at the time, because, for the first time, a 2D numerical modeling has been done for Newtonian laminar flow on a micro-scale particle. The bounce-back phenomenon due to the sudden pressure drop is first-ever investigated and described. There is a critical Reynolds number (Re_{crit}) to be found at different contact angles. The definition of Re_{crit} is a Reynolds number of the particle when the complete oil separation happens. Additionally, the oil separation from a porous particle is first-time modeled by introducing an artificial roughness of 17%. As a result, oil stays in the pore at Re of 5 with contact angle of 170^o and Re of 200 with contact angles of 0^o, 90^o, 170^o. The influence of the model dimension (2D and 3D), model parameters (interfacial tension, volume of oil, diameter of particle, fluids' properties), and computational grids are investigated.

The models have been validated against experimental data in Mehrabian et al. [2]. Good agreement between numerical predictions and experimental data is observed. A typical experiment is repeated numerically using CFD-based numerical simulation, but with a different submodel. One valuable finding from the validation case is that while retaining the same situation, the separation occurs easily when a higher water viscosity than the oil. Different from Mehrabian et al. [2], this work is renovated and performed under normal water phase conditions, specifically the assumption of that the viscosity of water phase is the same with it is in the oil phase (1mPa s).

Acknowledgements

I would like to express my deep appreciate to many people who have supported and helped me with their expertise.

I would first like to thank my mentor and supervisor **Dr. Petr A. Nikrityuk** of the Chemical and Materials Engineering Department at University of Alberta for his encouragement for my research throughout my study. His door is always open whenever I encounter troubles on my research, courses or even writing problems. His extensive knowledge on CFD and Numerical Modeling provided insights and expertise that assisted my research. His guidance helped me at all times of research, as well as many study skills for the lifetime learning.

Beside my supervisor, I would like to thank my colleague, Hongbo Shi, who has shared his wisdom with insightful comments and encouragement. I am grateful to Hongbo Shi for helping me to well control and understand the commercial software of ANSYS FLUENT [1]. I pay my deepest gratitude to him.

Last but not the least, I would like to thank my parents: Ming Li and Shuping Zuo, for giving birth to me at the first and give me an opportunity to feel the wonderfulness of knowledge and the spiritual world.

Table of Contents

List of Tables

List of Figures

List of Symbols

a_q	volume fraction of q^{th} fluid
C_D	drag coefficient
d_s, d_p	diameter of solid particle
$\dot{m}_{qp}$	mass transfer from phase q to phase p
V	volume of cell
g	gravitational acceleration
$g_{0,ss}$	radial distribution function
Ca	capillary number
f	volume fraction
Re_s	Reynolds number
U_∞	free stream velocity
l	reattachment length
P	pressure
R_0	radius of particle
r	radial position
t	time
u	radial component of velocity
V	velocity
p	viscosity ratio
c	specific heat
h	oil film thickness
$U_{O/W}$	interfacial velocity between water and oil
Re_{crit}	critical Reynolds number
Greek letters	
μ	dynamic viscosity

ν	kinematic viscosity
σ	interfacial tension
ε	dimensionless film thickness
ρ	density
$\dot{\gamma}$	shear rate
ψ	stream fuction
δ_{ij}	Kronecker symbol
α	contact angle
η	volume ratio of (oil) to (oil+particle)
k	curvature
λ	bond number
ζ	dimensionless volume

Index

g	gas phase
l	liquid phase
p	particle
s	solid phase
∞	outer boundary
n	index for previous time step
$n+1$	index for new/current time step
f	face value
x	x direction component
y	y direction component
z	z direction component
x, y, z	Cartesian coordinates

Chapter 1

Introduction

1.1 Background Study

Canada is the sixth-largest producer of crude oil in the world with extensive oil and natural gas reserves across the country [6]. Canadian energy production has almost doubled since 1980s [7]. Canadian oil reserves total 171 billion barrels, of which 165 billion barrels can be recovered from the oil sands using today's technology [7]. As the world's conventional oil resources decline, developing new recovery technology for unconventional crude oil, namely oil sands, is more favorable [7]. Alberta has the largest oil sand deposits in Canada, but with the current extraction technologies, the large energy input and tailings waste management are still major issues for both the industry and government to focus on. There are two types of extraction methods [8]. One is open-pit-mining extraction which is widely used in the oil sands industry to recover bitumen at greater than 90% recovery [9]. The other one is in-situ technique, such as Steam Assisted Gravity Drainage (SAGD) which is suited for deeper mines. Both method require a large amount of energy inputs.

Since oil sand is a mixture of bitumen, water, clay, and quartz sand and the grade of oil sand is categorized by its bitumen content, the purer the extracted oil, the more valuable it is [10]. One common classification scheme of oil sands is as follows: greater than 12% bitumen by weight for "rich oil sand", 10-11% for "average", 6-9% for "lean", while less than 6% is not of "ore-grade" quality [11]. Thus, the major focus is to separate sand particles from oil by using less energy. At present, this process is achieved through hot water extraction [12], filtering [12], gravitational sedimentation [13], and adding diluent or chemical treatments [14]. For Alberta's unconventional crude oil, there are three crucial challenges the industry faces when considering a more advanced and comprehensive oil sands extraction technique [12].

A favorable technology should consider the following factors.

1.1.1 Pollution

A large percentage of extra-heavy oil has to be produced by open-pit-mining or in-situ techniques [11]. The standard Hot Water Extraction Method requires significant amounts of heat and water than the extraction of conventional oil. At the same time, SAGD or other thermal methods also end up polluting many tailings ponds [15]. As mentioned, the extraction process contains water processing and adding diluent; as a result, tailings ponds potentially contain naphthenic acids [16]. According to Alberta Energy Regulator's Directive 085: Fluid Tailings Management for Oil Sands Mining Projects, each tailings pond must have a detailed fluid tailings management plan submitted [10].The aim is to have every tailings pond de-watered and containing no hazardous chemicals. The interest in waterless and chemical-free extraction is very popular. Next, oil spills are the most common issue on oil production sites.

In 2010, the Deepwater Horizon spill [17] drew widespread public attention and raised awareness of the environmental impact of oil extraction as well as led to an increase in research activities. The fundamental issue is a more advanced understanding of the interaction between oil and particles. For onshore sites, ocean waves could sweep away the contamination area. However, it is much more difficult to clean up oil spills on soil [18]. Soil would absorbs the oil which causes irreversible harm to the environment and to human health. Thus, oil separation from soil is an extremely important issue for which a solution needs to be achieved [19].

1.1.2 Safety

A critical threat in oil production is the presence of sand particles. The oil and/or water flowing from oil-reservoirs through perforations into the main wellbore can be affected by the presence of sand particles and their clusters [20]. Indeed, one of the most severe well–bore problems in the petroleum industry is the sand production that occurs when the reservoir sandstone fails under in-situ stress. Sand debris can be transported by the flowing liquid and cause problems in the downstream operation such as the abrasion of equipment or flow obstruction by sand deposits [21]. The exact mechanisms of sand production and transport are still not completely understood at the level of individual grains, where capillary forces between grains due to liquid bridges (oil/water wet systems) may play a significant role [22].

1.1.3 Efficiency

In order to achieve high energy efficiency, the initial oil–sand contact is crucial for oil extraction and recovery. Due to its high viscosity and adhesive nature, high density oil could pick up sand particles of any size within a short contact time, as low as several milliseconds [23]. Nevertheless, the resulting detachment of sand particles from oil would vary under different conditions. Therefore, this study aims at investigating the interactions between oil and sand to further understand the detachment process between oil and sand in a flotation process under various conditions including pH, temperature, sand particle size and wettability [23].
Over all, the petroleum industry demands an efficient and economic separation technology which could improve the environmental performance of mineable oil sands. This target ultimately includes a reduction in energy requirements (e.g. CO_2 emissions, hot water production, diluent usage).

1.2 Existing Technologies

1.2.1 Hot Water Extraction Process

The earliest recorded separation method was in 1930. The photographs of oil sands separation at Fitzsimmons's camp show an outdoor set-up, with open troughs and men manually stirring, skimming and scooping [24]. After years of experimentation, Clark et al. [24] developed the Clark Hot Water Extraction Process. At the 1951 Athabasca Oil Sands Conference in Edmonton, Clark et al.[24]. stated that "Freshly mined Alberta oil sand contains about 2 to 5% water and 10 to 17% oil, the balance being mineral matter [24]. The hot water separation process as practiced by the Research Council of Alberta involves increasing the water content to about 12% by means of hot water and/or steam while the oil sand is being heated to a temperature of about 80 ^{o}C, during which time a certain amount of mixing or kneading of the oil sand takes place. A residence time of 15 minutes in the conveyor and mixer is sufficient [24]. When the pulp reaches a temperature of about 80 ^{o}C, it is dropped into a turbulent stream of circulating plant water. In the case of the separation plant at Bitumount, it is dropped into what has been termed the sand distributor. The circulating plant water passing through the sand distributor washes the pulp into a comparatively large body of hot water, in what is called the separation cell, the temperature of which is about 85 ^{o}C. In the separation cell the oil floats as a froth on the surface of the water and is skimmed off, while the bulk of the mineral matter sinks to the bottom and is removed and discarded [24]."

The effectiveness of oil separation from sand would decrease by around 40% if the separation process does not take place as soon as excavation [24]. Secondly, at such high temperatures, there are many bubbles forming and carry fine sand particles rising to the oil surface. However, if there are too many bubbles, it would cause sand particles to be carried up into the oil froth [24]. As much as five times the optimal amount of mineral matter can end up in the separated oil as a result.

Over the years, Sycrude and Suncor have developed the Clark's hot water separation process into a modified process [11]. First, the blended slurry is subjected to aeration resulting in three layers in a primary separation vessel (PSV): a bitumen froth on top; a mixture of bitumen, sand, clay, and water in the middle (middlings); and sands at the bottom. The sands are pumped into a settling basin where they are known as tailings. The middlings are further separated and cleaned by air injection and by steam de-aeration [24]. After the bitumen froth is de-aerated, it becomes a highly viscous fluid typically consisting of 60% bitumen, 30% water, and 10% solids. This mixture is not suitable for pipelines; therefore it must undergo froth treatment. The bitumen froth is first diluted with a hydrocarbon solvent (e.g. naphtha, toluene) to reduce the viscosity and density of the oil phase. This accelerates the settling of the impurities by gravity or centrifugation [11]. The bitumen is skimmed off and processed further to reject the entrained solids and water to meet the requirements of downstream pipelines and refineries. The rejected solids and water from the froth treatment process, together with all the residual water, solids, added chemicals, and unrecoverable bitumen are referred to as middlings and are the waste to be disposed of in tailings ponds [11]. Because the waste stream has economic value as well as a significant environmental impact, producers invest significant capital and operating costs in various technologies to capture as much value from the middlings as possible before discharging them to the tailings pond for long-term storage.

Generally, modified hot water extraction can recover up to 95% of the bitumen, though it has been shown that organic-rich solids or toluene-insoluble organics directly absorbed onto particle surface fraction in the oil sands are an impediment to bitumen separation and upgrading and the clay fines and polar organics can cause poor bitumen recovery [24]. Recent enhancements such as tailings oil recovery units (TOR), diluent recovery units, and inclined plate settlers (IPS) as well as centrifuges have been employed to increase recovery to higher than 90% [24].

1.2.2 Recovery of Bitumen Using Hot Water and Pressure Cycles

In 2012, Painter et al.[25] published process involves a number of pressure cycles and the use of CO_2. It accelerates the recovery of bitumen, requiring no intense

agitation, caustics, or other chemical additives that aggravate subsequent treatment and disposal issues [25]. Decompression creates expanding micro-bubbles to dislodge bitumen from the sands. About 92% recovery was achieved within 5 minutes for a solid slurry of 1:1 (water/solid) volume ratio by 4 pressure cycles of air at 6.9 atm (100 psi) and 105°C [26]. The use of CO_2 in lieu of air makes recovery at lower temperatures or pressures possible, albeit with increased number of cycles at milder conditions (e.g., more than 90% recovery with 20 cycles at 55°C and 6.9 atm, or at 85°C and 3.4 atm). The new process requires less water and heating and results in high yields and no problematic end product [26].

1.2.3 Recovery of Bitumen Using Ionic Liquids

The current technology used for the extraction and separation of bitumen from oil sands for the purpose of processing fuels is relatively expensive and not environmentally-friendly as shown above. Roughly two tons of oil sands are required to produce a barrel of oil, and the separation of the bitumen from sand and clay requires significant amounts of energy and the use of large quantities of water [25]. Some waterless-based technologies are under-studied. Methods recently proposed are hydrolysis [27], supercritical extraction [28], solvent extraction [29], and extraction assisted by room-temperature ionic liquids [25]. The ionic liquid-assisted method is particularly attractive, because it might not need an external heat and the ionic liquid can be recycled and reused. The experiment was based on a medium Canadian tar sand with about 10% bitumen content. In the initial experiments, the mixture of oil sands, toluene, and an ionic liquid (based on imidazolium ions) was stirred in the proportions 1:2:3 by weight at between 50 and 55°C [25] . However, Painter et al.[25] later found that shaking a vial containing such a mixture at room temperature also achieved a degree of immediate but incomplete separation, while stirring for two hours increased the yield to values comparable to those obtained at higher temperatures. Painter et al.[25] used a Thermo Scientific Nicolet 6700 Fourier transform infrared (FTIR) spectrometer to obtain FTIR spectra [25]. The spectra of the grinding sample were referenced against pure KBr. Spectra of bitumen were obtained by casting toluene solutions onto a KBr window and evaporating the solvent in a vacuum oven at 100°C, forming a thin film for analysis [25].

Overnight, ionic liquid stayed at the bottom of the vial. After washing with water, the spectrum of the residual sands and clays that remained in the form of a slurry without residual ionic liquid. Of a concern was the presence of any mineral fines in the bitumen extracts and the degree to which the IL can be separated from the residual minerals [25]. The bitumen/toluene layer was simply removed from the

phase-separated mixture using a pipet. Any small amounts of entrained IL were easily separated by a second washing treatment and then dried under vacuum [25]. The final toluene/bitumen layer contained almost no mineral fines. The last step was evaporation of the toluene.

The concluding results presented did not provide a good commercial value for introducing this process. Some areas still needed further exploration, namely, choice of ionic liquid, kinetics of the separation process, costs, and potentially environmental concerns.

1.3 Literature Review on Modeling

Mehrabian et al. [30] studied oil and particle separation in a falling sphere configuration which focused on fluids' viscosity ratio and interfacial tension. Mehrabian et al. [30] used a solvent to change oil density and a surfactant to change interfacial tension to find out how the separation rate changed with the ratio. The object of investigation was a single oil-coated spherical particle falling through an aqueous solution. The experiment included two stages [31]. The first stage was the deformation of the oil film, followed by the formation of a "tail" of the particle. The second stage was the breakup of that tail. They observed that the maximum separation occurred when the capillary number is close to 1 [30]. At a very low capillary number, the viscous shear forces are not strong enough to overcome the interfacial tension forces, or the viscosity ratio is very high and longer shearing time is required for the separation to take place. During the first stage, with a low viscosity ratio (μ_2/μ_1), the oil layer coating the sphere instantly begins to deform and separate [30]. Then the normal stresses at the oil-water interface become high, which leads to a high interfacial velocity and explains the rapid deformation/separation that is observed. Increasing viscosity ratio increases the tangential stress at the interface which enhances separation [30]. However, if the viscosity ratio increases much further, the interfacial velocity decreases, which would lead to a delay in the separation process. Thus, when the viscosity ratio is between 0.1 and 1, both the normal and tangential stresses contribute to deformation and separation. It indicates the capillary number close to 1 [30]. For the second stage, it was observed that the larger the tail is, the faster the separation process would be.

Smith et al. [32, 33, 34] studied regarding separation of a liquid drop from a sphere in late 1980s. In a number of industrial processes for the treatment of mineral slurry, the interaction of solid surfaces with liquid/fluid interfaces is of great importance [33].

Smith et al. [32] classified the question into a three-phase interactions [33] involving solid particles and fluid drops in an immiscible liquid medium. These interactions rarely occur without any fluid motion. Smith et al. [32] added an immiscible fluid phase without any external force. However, gravity and interfacial tension were the only focus. The major problems encountered in the analysis were the mechanics of the particle motion, drop deformation, and three-phase solid-oil in a continuous fluid contact [33]. By investigating an oil-coated particle submerged in a continuous phase fluid, the equilibrium was simply predicted. The ratio of gravity to surface tension was critical. Meanwhile, the contacting angle between the water phase and oil film was an important indicator[34]. There were two equilibrium: one happened naturally without any outside effects, and the was the maximum angle for which an equilibrium of the oil could exist. At the second equilibrium, oil separation most likely occurred. In conclusion [33], the particle shape was related to the oil separation when there was no external shear force. Last but not least, Smith et al. [33] observed the oil film starting deforming when the contacting angle was nearly zero. It resulted in less than 0.1% of the remaining oil film [33].

1.4 Benchmark Experiments

1.4.1 Initial Modeling

As mentioned above, there is a series of experiments conducted by Fan et al.[3]. The very first experiment studied configurations of drops attached to spheres immersed in a uniform laminar flow [3]. Fan et al.[3] used numerical modeling to model a spherical solid immersed in a uniform fluid. A finite volume approach was used to solve flow equations and the Volume of Fluid (VOF) method was used to track the oil/water interface. By ignoring the gravitational force, this became a 2D problem. In 1985, Smith et al. [32] also investigated a similar problem. They studied the behavior of a single tesphere solid particle partially/entirely coated by a fluid in a linear shear flow [3]. Smith et al. [32] used an axisymmetric oil-coated particle and let it immerse in a continuous flow. Gravity and interfacial tension were both present and considered (as Figure1.1).

The model involved two parameters: the ratio of gravity to interfacial tension and the oil volume. They both yield contact angle versus equilibrium plots [3]. The contact angle was defined as the angle between the boundary and the interface of interest, shown in Figure 1.2. After comparison between experimental data and theoretical values, it was found that oil separation occurs the higher the contact angle. It was concluded that for the partially-coated particle, the liquid/solid separation

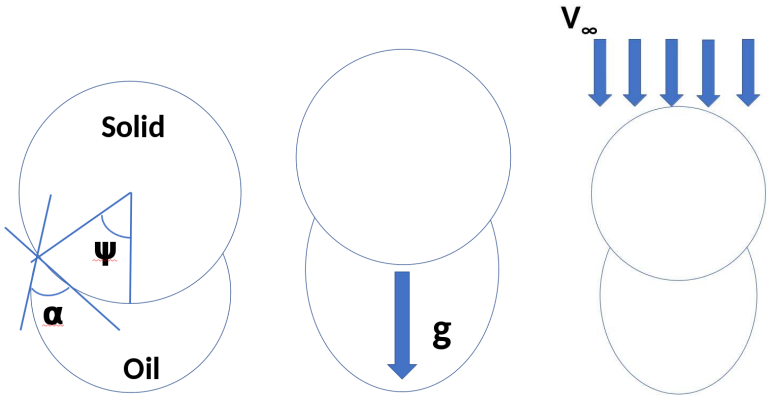

Figure 1.1: The solid/oil configuration under different forces, adapted from [3]

depended strongly on the system properties; meanwhile, the fully-coated particle, was found to have a high shear rate between the solid/liquid interface [3].

Smith et al. [33] paid more attention to the external forces rather than gravity in 2010. Based on the previous work, the contact angle (α) still plays the main role, as well as the oil volume fraction (η). Bussmann et al. [30] has selected 30 ^{o} and 90 ^{o} as the contact angle. In the mesh, it is shown as Figure 1.2.

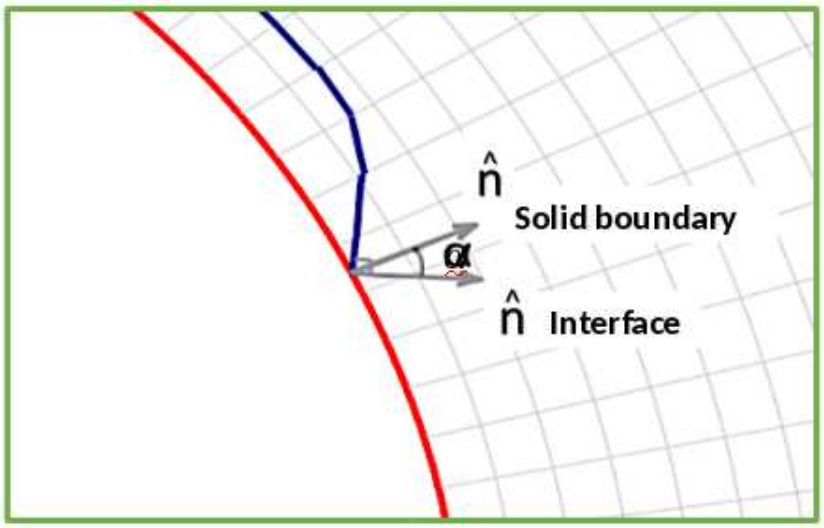

Figure 1.2: Contact angle between two flows, adapted from [3]

And the oil volume fractions are 0.2 0.4 and 0.6 respectively [33].

$$\eta = \frac{Oil\ Volume}{Oil\ +\ Particle\ Volume} \tag{1.1}$$

adapted from [3]

They have used a flow solver of Volume of Fluid (VOF). It is a surface tracking technique by using calculating the fluid volume instead of interface itself [3]. In the CFD simulation software they used, the governing Navier-Stokes equations (finite volume method) are to discretized domain and VOF is to track oil/water interface. The mesh contains number of small cells and each cell has its own volume fraction recorded [3]. Once the volume fraction of one cell is 0, it indicates the cell is empty. Since applying the same strategy to start the first modeling work, more details will be discussed in Chapter Two. The mesh used in Bussmann et al. [3] experiment is shown as below. The interfacial cells have volume fractions between 0 and 1.

$$Re = \frac{\rho_{water}\ U_\infty\ d}{\mu_{water}} \tag{1.2}$$

adapted from [3]

In order to compare results with different parameters, there are two dimensionless quantities being used, namely, Reynolds number (Re) and Capillary number (Ca).

$$Ca = \frac{\mu_{water}\ U_\infty}{\sigma_{water}} \tag{1.3}$$

adapted from [3]

where U_∞ is the free-stream velocity, σ_{water} is the surface tension, d is the diameter of the droplet, ρ_{water} is the water density, μ_{water} is the water viscosity.

By applying the same velocity, surface tension changes as time goes on. The force difference between surface tension and interfacial shear force makes the movement of the oil. The following figures 1.3, 1.4 were generated by the Bussmann et al.[3]:

Some important findings from their study are as follow [3]:

- As everything else is equal, the oil acting at the smaller contact angle will wet a larger portion of the surface, creating a greater surface tension, by comparing both figures 1.3 and 1.4. Then it gets harder to remove the oil.

- When the Ca is much less than 1, shear forces are too small to be considered; when the Ca is approaching 1, the shear force would overcome the interfacial tension. In the end, the oil film would eventually slip away from the sphere top.

In Bussmann et al. [3], the understanding of changing oil volume fraction is not

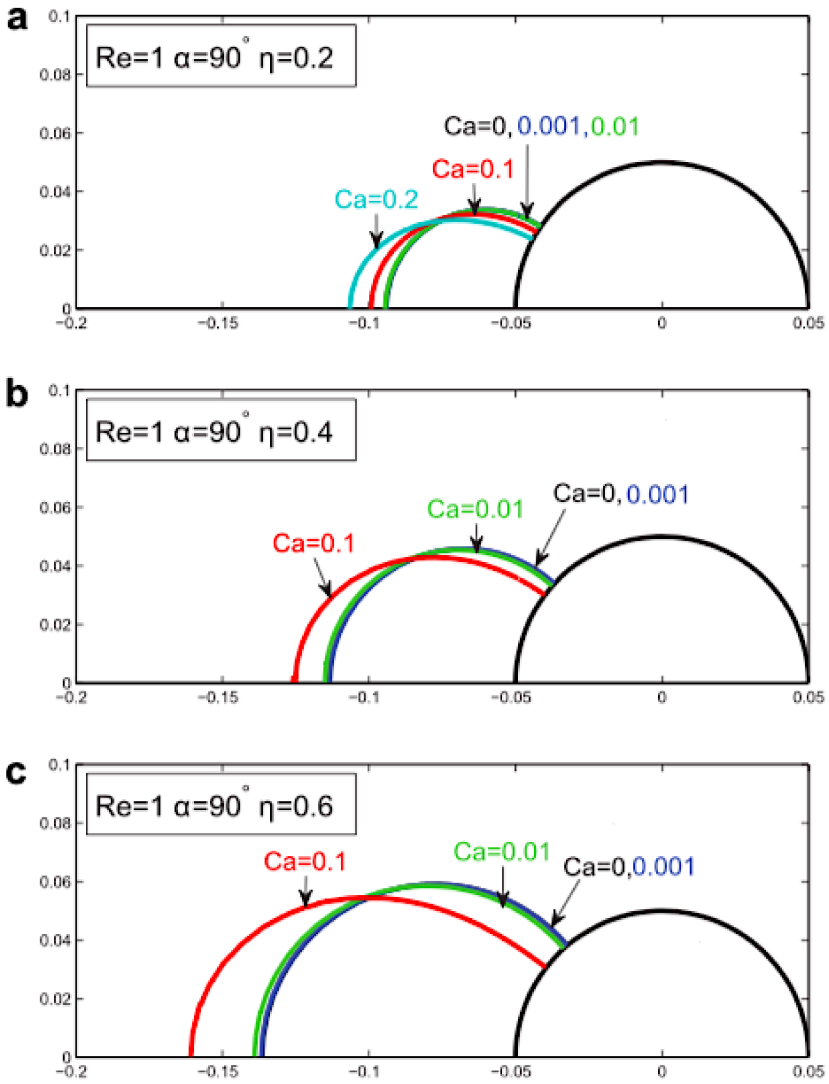

Figure 1.3: Equilibrium configuration for Re=1, $\alpha = 90$, (a)$\eta = 0.2$, (b)$\eta = 0.4$, and (a)$\eta = 0.6$, redraw from [3]

comprehensive enough. It relates to another topic on how the oil film rupture, or in the other word, "oil film rupture mechanism" [3]. Five years later, Bandara et al. [35] studied breakup of high solid volume fraction oil-particle cluster in simple shear flow. It examined oil-covered particle samples which are preferred in the oil/particle separation process. The oil volume fraction is high and the solid particle is relatively large and is immersed in a uniform aqueous flow at contact angle of 90°. This experiment [35] focused on the breakup of oil-particle clusters and the separation of particles from the clusters. It evaluated as a function of viscosity ratio of the

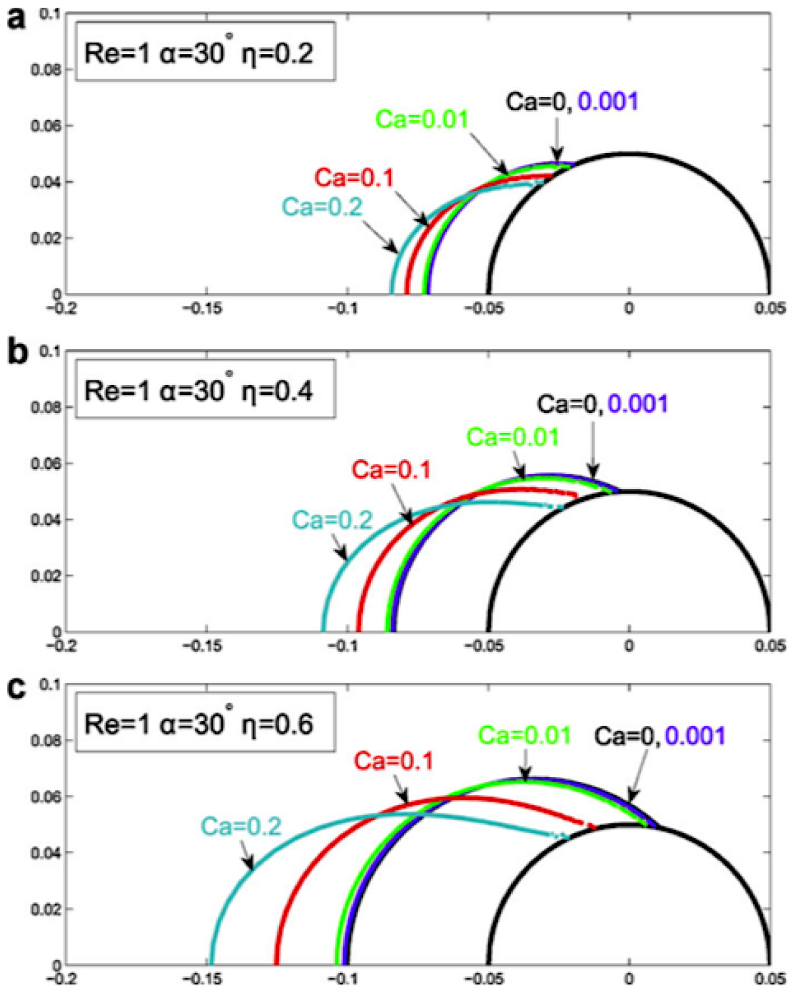

Figure 1.4: Equilibrium configuration for Re=1, $\alpha = 30$, (a)$\eta = 0.2$, (b)$\eta = 0.4$, and (a)$\eta = 0.6$, redraw from [3]

oil phase to the aqueous solution, interfacial tension, and shearing time [2]. It also confirmed that lowering the interfacial tension facilitates the liberation of oil droplets from particles. Furthermore, the conclusion suggested the separation of oil clusters from particles is closely related to a critical capillary number and the viscosity ratio [35]. The critical capillary number is where clean particles are obtained [2]. Since our objective is on the microscale particle, this experiment will not be described in detail here.

1.4.2 Experimental Apparatus Setup

Based on the previous modeling, Bussmann et al. [2] set up an experiment to investigate more closely into three main factors: oil film thickness, viscosity ratio, and interfacial tension. The experiment apparatus was a 10 x 10 x 42 cm^2 acrylic tank as Figure1.5. The experiment was to examine the oil separation from the particle in a falling sphere configuration, shown as Figure 1.6. The rectangle tank was used instead of a cylindrical tank due to optical distortion minimization. The top electromagnet acted as a free releasing device of a sphere solid [2]. Beside the tank, there was a high-speed camera which recorded the falling particle and the movement of the oil film. After recording, all data was captured into a MATLAB image processing tool-box. All experiments were performed at room temperature (25 ± 1 °C) [2].

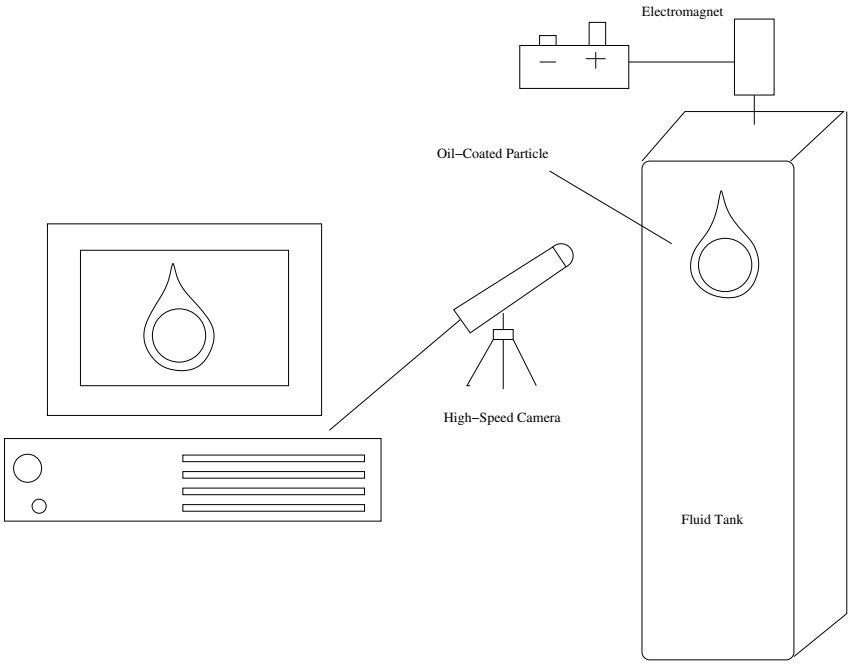

Figure 1.5: Schematic of the experimental apparatus, adapted from [2]

The sphere particle was made of steel with a diameter of 4.26mm (±0.0238mm). The steel has a density of 8302.7 kg/m^3 ($\pm 123 kg/m^3$). The controllable variables were dimensionless oil film thickness ($\varepsilon = h/R_0$), viscosity ratio between oil and water (p $=\mu_{oil}/\mu_{water}$), and interfacial tension (σ).

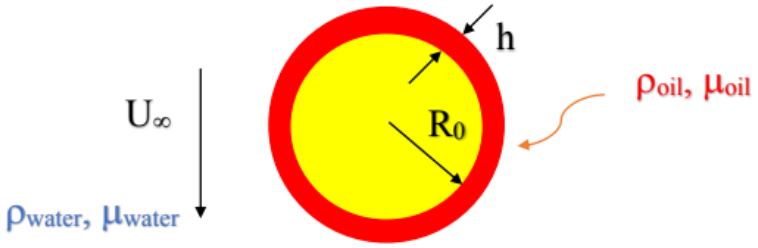

Figure 1.6: Schematic of the falling solid sphere particle

1.4.3 Effects of Oil Film Thickness

The density of the oil phase is 970 kg/m^3 and the density of the aqueous solution is 1040 kg/m^3. The viscosity ratio p is calculated as p=0.08. The aqueous phase contains about 2.5% of the water-soluble polymer carboxymethyl cellulose (CMC) solution. Due to its high viscosity than pure water, it will slow the falling of the solid particle in order to have better pictures of the sphere movement [2]. The measurement of equilibrium interfacial tension is 27.6 ± 1.4 mN/m. The terminal velocity of the oil-coated-particle is 6.5 cm/s. As the particle falls, the velocity will increase about 1.5 times greater than the initial velocity [2]. The target measurements in this experiment are: velocity of oil-coated sphere; the amount of oil separated during the fall; and the amount of oil left on the sphere at the bottom of the tank. A weight boat is used to weigh the mass of sphere at the top and the bottom of the tank. First, an oil-coated sphere is dropped freely by the electromagnet and gently suck into the aqueous phase [2]. MATLAB toolbox records high-speed videos of each experiment. Secondly, the high-speed video converts to high-solution (3256 x 2592) images. The following sketches are regenerated from the high-solution images. The dark blue represents the thicker fluid which is oil phase; while the light blue represents the thinner phase, which is water. Every image could cover around 2 cm in length [2]. Thirdly, the velocity of oil droplet can be calculated and masses of the sphere at the top/bottom are obtained from the weight boat reading. Four sample images are shown in Figure 1.7 and Figure 1.8. The first illustration is an oil-coated droplet just about reaching the bottom of the tank. The remaining three illustrations show droplets at the bottom of the tank under different velocities.

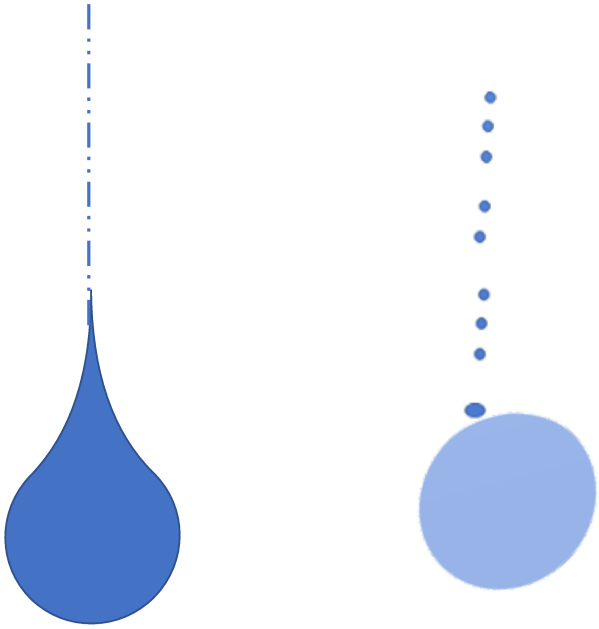

Figure 1.7: An oil-covered droplet movement at about reaching the bottom of the tank and at the bottom of the tank with the remaining oil deformations, adapted from [2]

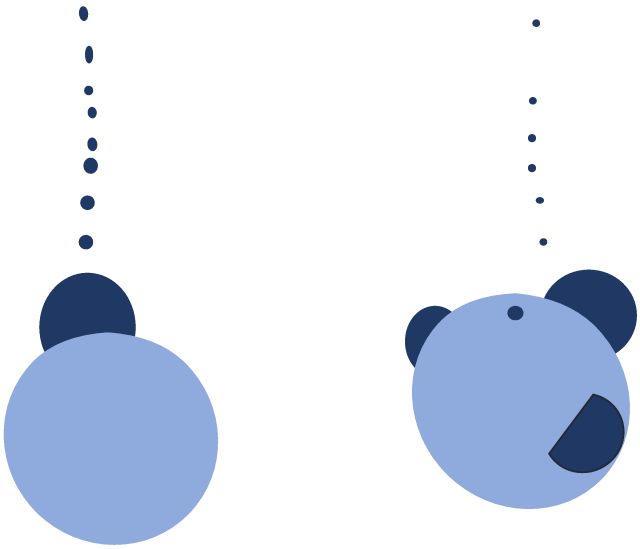

Figure 1.8: An oil-covered droplet movement at the bottom of the tank with the remaining oil deformations, adapted from Bussmann et al.[2]

With various oil film thicknesses, there are sequences that are observed. For the sphere covered by a relative thick oil film, the oil starts to move to the edge of the sphere almost instantaneously following by a thick oil tail [2]. The tail becomes

thinner and thinner until it reaches an equilibrium. In this falling process, much oil will be removed. For the sphere covered by a relative thin oil film, a very thin oil tail deforms as long as it releases. However, it takes a much longer time for the eventual oil separation or for even very few (negligible) amounts of oil to be removed. The instantaneous velocity measurement answers this phenomenon [2]. At high oil loading, the velocity is much higher than at low oil loading. Apparently, while holding everything else to be the same, a high oil loading will promote a better separation process. Bussmann et al. [2] classified three loading groups, namely, low loading ($0.028 < \varepsilon < 0.056$), intermediate loading ($0.047 < \varepsilon < 0.066$) and high loading ($0.077 < \varepsilon < 0.100$) (All data are based on p=0.08) [2].

Note that the analytical data also indicates that there is a critical Ca value for oil separation close to 0.4 when p is 0.08 [2]. The critical Ca is where the most oil deformations begin as well as the time where the sphere reaches the calculated terminal velocity.

1.4.4 Effects of Viscosity Ratio and Interfacial Tension

Another set of experiments were performed two years later to study the effect of oil viscosity and oil/water interfacial tension [30]. In this experiment, the viscosity ratio becomes a variable with different oil thickness. The experimental apparatus remains the same. Furthermore, the experimental methodology is the same as the previous work [30]. In this experiment, the focus is the viscous shear stress and interfacial tension. Low Re values (< 1) are used so that inertial forces can be negligible [30]. Similar to the work Bussmann et al.[2], the target measurements in this experiment are: velocity of oil-coated sphere; the amount of oil separated during the fall; and the amount of oil left on the sphere at the bottom of the tank [30]. MATLAB image processing toolbox takes 1000 frames every second to provide sufficient high-resolution images. To measure interfacial tensions, two methods are used: When is greater than 1 mN/m, the Du Nouy Ring method [36] is used; when σ is less than 1 mN/m the spinning drop method [37] is used. There are four different types of oil used to examine different droplet behaviors within four different aqueous solutions (see Tables1.1and1.2).

After a set of experiments with five viscosity ratio, the following velocity data are obtained as Table 1.3.

In the observation, similar to the work in 2016 [30], each falling process can be classified into two steps: oil tail formation and oil separation. It leads to a different characteristic length when calculating Re. In the tail deformation step, the radius

Table 1.1: Aqueous phase properties

[Fluid	CMC(wt%)	SDHS(ppm)	NaCl(wt%)	μ_1 K(pa.s^n)	μ_1 n	σ (mN/m)
1	2.5	0	0	2.6	0.69	27.6
2	2.5	0	3	4.2	0.61	13.1
3	2.5	800	3	4.9	0.54	4.5
4	2.5	3000	3	4.9	0.54	0.02

Table 1.2: Oil phase properties

Oil	Bitumen(wt%)	Toluene(wt%)	μ_2 (pa.s)	ρ_2 (kg/m^3)
1	100	0	48	1000
2	90.9	10.1	1.8	987.1
3	83.3	16.7	0.43	975.9
4	76.9	23.1	0.1	968.4

Table 1.3: Terminal velocity data

Oil in Fluid 1	p=$\frac{\mu_2}{\mu_1}$	Velocity (m/s)	Convergence Starting Time (s)
1	39.22	0.053	0.37
2	1.44	0.054	0.39
Oil Free	0	0.062	0.40
3	0.36	0.064	0.30
4	0.08	0.071	0.1000

of the sphere is L, however, once the tail gets stable, the radius of the tail is L.

$$Re = \frac{\rho\, U_\infty L}{\mu} \tag{1.4}$$

To summarize, the following conclusions are made.

- With Re equals to 1, at low viscosity ratio, the oil portion begins to deform and separate. At high viscosity ratio, it takes longer for the oil to deform and separate, but the separation occurs at a faster rate.
- The optimum viscosity ratio in this case is between 0.1 and 1, it is where both the normal and tangential stresses contribute the most to deformation and separation.
- The optimum Ca is close to 1. At a very low Ca, the viscous shear forces cannot overcome the interfacial tension to make the oil move.
- Meanwhile, low interfacial tension would reduce the rate of oil removal.

Chapter 2

Model and Numeric Description

2.1 State of the Art in Droplet Modeling

Computational fluid dynamics (CFD) has become a widely used engineering tool for analyzing, optimizing and verifying the performance of designs [38], meanwhile predicting action of thermos-fluids in a system [39]. In this section, it briefly discusses some commonly used numerical methods to model droplet, namely, Coupling of Level Set and Volume of Fluid (CLSVOF), Continuum Surface Tension (CSF) and VDROP.

2.1.1 CLSVOF

One popular method to model two-phase flows in CFD is the coupling of level set and volume of fluid (CLSVOF). This model results in improved mass conservation while retaining the straightforward computation of the curvature and the surface normal [40]. In this section, we briefly discuss CLSVOF model. CLSVOF benefits from both volume of fluid method and the level set method. It is generally superior to either method alone [41]. namely, the Volume of Fluid (VOF) function provides the size of portion that the interface may pass through, and the interface normal vector $\overrightarrow{n}$ calculated by Level Set (LS) function ($\overrightarrow{n} = \frac{\nabla\phi}{|\nabla\phi|}$) determines the direction of the interface [42].

The basic continuity and Navier-Stokes equation for the incompressible flows are given as (rewrote from [43]):

$$\nabla \cdot \overrightarrow{u} = 0 \tag{2.1}$$

$$\rho\frac{\partial(\overrightarrow{u})}{\partial t}+\rho\nabla\cdot(\overrightarrow{u}\,\overrightarrow{u})=-\nabla p+\nabla\mu[\nabla\cdot\overrightarrow{u}+\nabla\cdot\overrightarrow{u}^{T}]-\sigma k\delta\cdot(\phi)\nabla\phi+\rho g \tag{2.2}$$

where, k is the interface curvature [43],

$$k=\nabla\frac{\nabla\phi}{|\nabla\phi|} \tag{2.3}$$

The distance function is $\delta(\phi)$ and equation is given as (rewrote from [43]):

$$\delta(\phi)=\frac{1+cos(\pi\phi/a)}{2a};when|\phi|<a \tag{2.4}$$

$$\delta(\phi)=0;when|\phi|\geqslant a \tag{2.5}$$

where $a=1.5w$ and w is the minimum size of a cell.

Sussman et al. [41] tested the CLSVOF and standard VOF on a 3D and axisymmetric incompressible two-phase flows, with and without viscosity problem in 2000. One difficulty of incompressible two-phase (eg. air and water) flow modeling is the high density ratio (around 1000:1) at the free-surface between the gas and liquid; especially, when surface tension is present and when a change of topology occurs. In this problem, it was observed a 4-mm air bubble rising to the surface of an air-water interface then bursting due to stiff surface tension effects [41]. It is similar to a microscale jetting problem (e.g. inkjet printing). The surface tension is dominant in such dynamic system. In this case, CLSVOF provides a more accurate surface tension model. By the end of testing, it is shown that CLSVOF has conserved mass within a fraction of one percentage for all cases [41].

By compare CLSVOF with the standard VOF in thermal droplet modeling, Lorenzini et al. [44] have conducted a set of simulations to investigate the features of flow boiling of water in a silicon microgaps device with a flow passage 250 μm high and 1.8 mm width, populated with cylindrical pin fins of 100 μm diameter. One challenge of the experiment is the desire of detailed thermal modeling of such has lagged behind due to the complexity of the involved phenomena. After an intensive investigation, CLSVOF was decided to be used which was more cost-effective and less time-consuming. In the CLSVOF model, the advection equation for the level-set function ϕ is incorporated for the phase-tracking as (rewrote from [43]):

$$\frac{\partial\phi}{\partial t}+\nabla\cdot(V_{int}\phi)=0 \tag{2.6}$$

Results indicate that both methods predict accurate two-phase flow regimes compared with observation in the experimental studies. Enhance, the CLSVOF offers a sharper interface reconstruction than the standard VOF method. Meanwhile, CLSVOF shows mechanisms more closely to experimental observations.

In terms of two-dimensional (2D) model,Zheng et al. [45] have published an investigation in hollow droplet impacting on a dry fat surface has obvious difference in its dynamics and heat transfer behaviors comparing with continuous dense droplet impact. In the present research, CLSVOF method is to investigate dynamics and heat transfer of a hollow droplet impact on a dry flat surface in [45]. Moreover, Sussman et al. [41] proposed an issue in CLSVOF method, the distance constraint condition of LS function sometimes cannot be met after several time steps as the nature of equations [46]. One possible solution is to adopt re-initialization process after every time step by coupling values of VOF and LS with a geometrical PLIC(piece-wise linear interface construction) method [46].

2.1.2 Combination of VOF and CSF

In order to solve a droplet formation problem within multi-phase fluids, combination of two or more numerical methods provides accurate results. Deng et al. [47] has investigated in a study of oil-in-water droplet formation in a co-flowing capillary device. This topic has a various application, such as, polymer microgels [48], cosmetics [49], food industries [50], drug delivery [51] and pharmaceutical [52]. Deng et al. [47] performed both the numerical and experimental tests. Major parameters are velocities and viscosity of continuous and dispersed phases, interfacial tension, and wall effect as well as the wetting property of the capillary on the droplet size [47]. Since the theoretical analysis would be too complicated to utilize in the understanding on the two-phase flow phenomenon with the changing droplet size distribution. In this case, the numerical modeling is a more effective and comprehensive alternative.

The objective is to correlate a dimensionless droplet diameter with two phase flow parameters and wall effect, so that the study for transition regime from dipping to jetting flow in the oil-in-water system is accomplished in Brackbill et al. [47].

Combining Volume of Fluid (VOF) and Continuum Surface Tension (CSF) method are used and compared with the experimental solution. VOF is used to track the interface of two immiscible fluids and will be discussed in detail in the next section. To calculate the surface tension for the cells containing the liquid-liquid interface, Deng et al. [47] used the CSF model. This model's main idea is to interpret surface tension as a continuous, three-dimensional (3D) effect across an interface [53]. Instead of applying a surface boundary condition as discontinuity, a

volume force due to surface tension on fluid elements lying within a finite thickness transition region is used in Brackbill et al. [53]. The original CSF formulation is given as (rewrote from [53]):

$$F_{st} = \sigma k \frac{\nabla \cdot C}{[C]} \frac{2\rho}{\rho_1 + \rho_2} \delta \tag{2.7}$$

Where, F_{st} is the surface tension body force, C is the filtered color function, σ is the fluid surface tension coefficient, ρ_1 and ρ_2 are the densities of phase 1 and 2 respectively, δ is the Kronecker delta function, k is the free surface mean curvature.

Generally speaking, there are three source terms corresponding in 3D along X, Y, Z. In this study, the formula has been eliminated into three components. The equation is given as (rewrote from Brackbill et al. [53]):

$$F_{st} = \sigma k \nabla \cdot \alpha \tag{2.8}$$

where σ is interfacial tension coefficient, k is the curvature of the interface, and α denotes a VOF volume function tracking the profile of the liquid-liquid interface [8], which is defined as the fractional volume of the continuous and dispersed phases in a computational cell. $\alpha = 0$ represents the cell is filled with dispersed phase, $\alpha = 1$ represents the cell is filled with continuous phase. When $0 < \alpha < 1$, the cell contains the interface. And in each control volume, the sum of volume fractions of all phases is 1. The interface between the two liquids is tracked by VOF method, the advection equation is given by Deng et al. [47]:

$$\frac{\partial \alpha}{\partial t} + u \nabla \cdot \alpha = 0 \tag{2.9}$$

The model input description are given below. Firstly, both fluids are assumed to be Laminar flow, because the Reynolds number in the co-flowing capillary is very small. The iteration time step is 10^{-8} s. The maximum number of each time step is 20. The inlets of water and oil phases were defined by normal speed calculated by volume flow rate, and the outlet was set as the opening boundaries with an atmospheric pressure. Second order upwind differencing scheme and the Green-Gauss Cell methods are set. Also, the no-slip condition is used [47].

To simplify the idea of CSF, it converts numerical models of discontinuities in finite volume and finite difference schemes are continuous transitions within which the fluid properties vary smoothly from one fluid to another fluid. Therefore, volume force is calculated by taking first and second order partial derivatives of the characteristics data [53].

2.1.3 VDROP

Another popular CFD method to study the oil-water separation characteristics for both macro and micro scale problem is the population balance method [54]. It provides better undertsanding on the droplet size distribution (DSD) and separation efficiency. In 2017, Zhao et al. [55] has presented VDROP model which is based on the population balance method in the International Oil Spill Conference [55]. This VDROP model take various forces into consideration, such as drag froce, buoyancy, lift, and added mass force [55]. In order to match with the experimental data, particle movement is essential. Thus, Zhao et al. [55] introduced the Lagrangian Particle Tracking (LPT) [55] to track the movement of the droplets. This model was validated in 2014 [55]. VDROP is to predict DSD in turbulent regimes while considering interfacial tension and oil viscosity. It is valid for both transient and steady droplet size distribution [55]. Since the model is based on the population balance models, it takes the advantage of it which provide the transient DSD of oil's different properties. Therefore, the steady-state DSD is just simply running the model with a long enough time [56]. Based on the research [57], we have concluded a brief summary with some major equations (rewrote from [55]).

$$\frac{\partial n(d_i,t)}{\partial t} = A + B \tag{2.10}$$

$$Term\text{–}A = \Sigma_{j=j+1}^{n}\beta(d_i,d_j)g(d_j)n(d_j,t) - g(d_i)n(d_i,t) \tag{2.11}$$

$$Term\text{–}B = \Sigma_{j=1}^{n}\Sigma_{k=1}^{n}\Gamma(d_j,d_k)g(d_j)n(d_k,t) - n(d_i,t)\Sigma_{j=1}^{n}\Gamma(d_i,d_j)n(d_j,t) \tag{2.12}$$

where, n the is number of droplets divided by volume; d_i is the droplet's diameter at a given time t. $\beta(d_i,d_j)$ is the dimensionless breakage probability density function for the creation of d_i due to breakage of d_j. $g(d_j)$ is the breakage frequency of d_j. For droplet breakup, term A represents d_i resulting from the breakup, while term B represents the death of d_i into smaller droplets. $\Gamma(d_k,d_j)$ is the coalescence rate (m^3/s), term A represents the birth of d_i. As a results of coalescence events occurring between d_k and d_j to form drops. While term B represents death of d_i due to the coalescence of d_i that forms larger drops.

The breakage rate is $g(d_i)$ that based on the mechanism of droplet breakup. It is caused by collision with eddies during the mixing. This equation is given from

Zhao et al. [55]:

$$g(d_i) = K_b \int_{n_e} S_{ed}(u_e^2 + u_d^2)^0.5 BE(d_i, d_e, t) dn_e \tag{2.13}$$

where, S_{ed} represents the collision cross section of eddy and droplet, u_e is the turbulent velocity of an eddy, u_d is droplet velocity, n_e is number concentration of eddies (number of eddies/m^3). In the inertial subrange of the energy spectrum [58], u_e is the turbulent velocity of an eddy and u_d is the drop velocity, they are given as [59]:

$$u_e = 2.27(\varepsilon d_e)^1/3 \tag{2.14}$$

$$u_d = 1.03(\varepsilon d_i)^1/3 \tag{2.15}$$

where, ε is the energy dissipation rate (W/kg). The velocities are average of the eddy and droplet velocities.

In summary, the results generated by VDROP model for both transient and steady-state DSD are compared with the available literature experimental data [60], [35]. Both show good agreement.

2.2 Volume of Fluid (VOF) Theory

In order to achieve better equipment design and enhanced operations, this work makes use of mathematical models for a single oil droplet within a continuous medium. Due to symmetry of flow field within the tank, a section in the axial direction is taken in CFD calculation, and thus the 3D simulation can be simplified to a two-dimensional [61]. For a 2D multiphase problem, ANSYS FLUENT [1] is one of the best software to conduct numerical simulation. This requires some critical parameters to provide accurate outputs, such as grid size, mesh design, oil properties and water/air properties [1] . When solving this problem, a sub-grid might be used to keep a comparable size difference of the interested interface. Based on the demand, ANSYS FLUENT is the best fit modeling software to use. Before model any matter, it is essential to plan a clear procedure. The life cycle study [62] is a good way to understand the main issue and list all main concepts. In the practical situations, discussion with clients about a simulation should be taken at the first place. A general logical diagram visually provides a better understanding below, as Figure 2.1.

Standard steps needed before proceeding to model [1]:

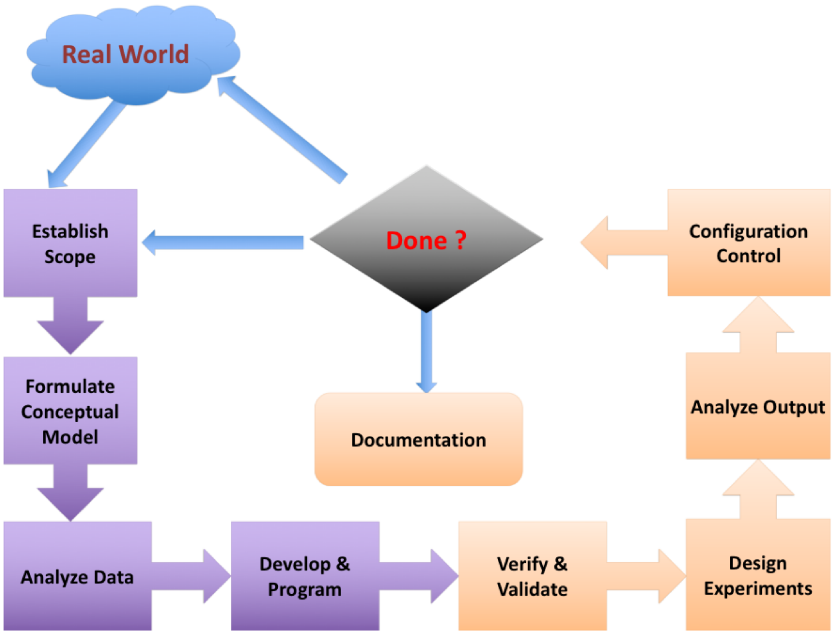

Figure 2.1: General modeling process

- Establish purpose and scope
- Formulate the conceptual model
- Acquire and analyze data
- Develop simulation model and program
- Verify and validate the model and simulation
- Design experiments
- Execute simulation and analyze output
- Configuration control
- Develop documentation

The objective of this study is to investigate a favorable technology of oil particle separation and compare existing technologies. The major observed object is a single oil-coated particle within a uniform water flow of an unknown inlet velocity under the same surrounding temperature conditions. The interaction between a thin-oil-film covered droplet and surrounding continuous water is a microscale problem. By applying an unknown velocity on the thin-oil-film, the desire outcome is the reduction on interfacial tension. Once the external shear just overcomes the interfacial

tension, then the oil portion will not be held in the particle surface and starts to slide away. It will require multiple trials of experiments [1]. Meanwhile, it is difficult to observe such small movement in real experiments and also be costly through whole process. Based on such facts, Computational Fluid Dynamics (CFD) is the reasonable technique to assess the performance of a microsized particle covered by thin oil film.

In this chapter, the main goal is to model a microscale single particle within the practical surrounding condition in Figure 2.2; to determine an optimal inlet velocity which can separate oil film from the particle surface; to further modify current modeling based on analysis. All modeling works would have performed by ANSYS FLUENT 14.5 [1]. The major inputs are particle size and oil film thickness, fluid properties, and facility conditions. The output is the complete oil separation.

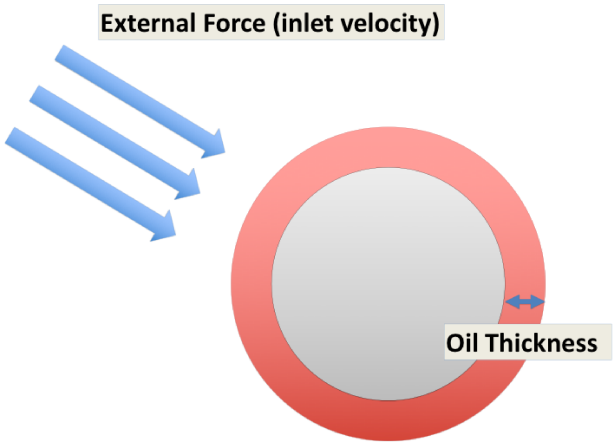

Figure 2.2: Single particle covered by a thin oil film

There are few literature investigating on separation sand particles from oil on the microscale, such as a single oil-coated droplet. The fine sand particle size is range from $1\mu_m$-$100\mu_m$, while both oil and water phases present. Thus, Volume of Fluid (VOF) is selected as the most appropriate CFD model technique to use. With a multiphase flow and microscale framework; assuming a finite size of the droplet. The shape of droplet is assumed to be sphere, because of the microsize. Whereas the tracking of the interface is the interest.
The main components we need to consider before using VOF:

- Defining target interface
- Tracking of immiscible liquid-liquid interface
- Computational grid size
- Surface tension
- Boundary conditions
- Selection on solver options available for modeling

ANSYS FLUENT 14.5 [1]has provided its users a comprehensive theory manual. It is important to read through the selected model method chapters. It is clearly stated several restrictions of VOF model in ANSYS FLUENT [1]. Firstly, VOF can only be solved with the pressure-based solver instead of the density-based solver. Void regions where no fluid of any type cannot be utilized in the model, all control volumes must be a single fluid phase or a combination of phases [1]. Among all the phases, only one can be applied as a compressible ideal gas. When the VOF model is used, stream- wise periodic flow cannot be modeled. "The second-order implicit time-stepping formulation cannot be utilized with the VOF explicit scheme." Also, the DPM model cannot be adapted with the VOF model when tracking particles in parallel if the shared memory option is enabled [1].

The VOF model can be applied to compute time-dependent and steady-state solutions [1]. When your solution is independent of the initial conditions and the inflow boundaries for the individual phases are different, you can use a steady-state calculation in problems where only a steady-state solution are concerned [1]. To be noted, mesh adaptively was shown to play a key role in resolving the boundary layer at the interface between the water phase and the oil phase without the increase in computational power that uniformly sized fine meshes would demand [63].

2.3 Model Formulation

A good approach is for the simulation analyst to connect with the real-world problem is to set up assumptions about the real-world system associated with the problem statement [62]. Furthermore, validation is a must for all steps. If any results are stated without validation, it is possible to be not used eventually. VOF is a surface-tracking technique applied to a fixed Eulerian mesh [1]. Since the interface between oil and water is our interest (immiscible), VOF is the most appropriate method to use.

In this numerical simulation, we do not have a source term, then the equation of mass conservation equation can be written as (rewrote from [1]):

$$\frac{\partial \rho}{\partial t} + \frac{\partial (\rho v_i)}{\partial x_i} = 0 \tag{2.16}$$

In the 2D axisymmetric geometric, the continuity equation is given as

$$\frac{\partial \rho}{\partial t} + \frac{\partial}{\partial x}(\rho v_x) + \frac{\partial}{\partial r}(\rho v_r) + \frac{\rho v_r}{r} = 0 \tag{2.17}$$

There are two main calculation systems: steady-state and transient in VOF. As the time suggested, steady-state indicates a situation which does not strongly depend on time. In VOF, steady-state calculation is sensible only when the solution is independent of the initial conditions and there are distinct inflow boundaries for the individual phases [1]. Transient calculation is used to compute a time-dependent solution. If the shape of the free surface inside a rotating cup depends on the initial level of the fluid, using the time-dependent formulation, such as Transient Calculation is a must. On the other hand, if the flow of water in a channel with a region of air on top and a separate air inlet can be solved with the steady-state formulation [1].

When the VOF is tracking the interested surface, it is calculating volume fraction for each cell. Every single cell has its own index and the size of cell is determined by the user. When a_q=0, it means the cell of q^{th} fluid is empty. Likely, if a_q=1, it means the cell of q^{th} fluid is full. And a_q is always between 0 and 1. Based on the local value of a_q, the appropriate properties and variables will be assigned to each control volume within the domain [1]. The Volume Fraction Equation is used to track the interface between two phases. It can be solved by both implicit and explicit time discretization (rewrote from [1]).

$$\frac{1}{\rho_q}[\frac{\partial}{\partial t}(\alpha_q \rho_q) + \nabla \cdot (\alpha_q \rho_q \vec{v_q}) = \sum_{p=1}^{n} (\dot{m_{pq}} - \dot{m_{qp}})] \tag{2.18}$$

The primary phase volume is computed by (rewrote from [1]):

$$\sum_{q=1}^{n} \alpha_q = 1 \tag{2.19}$$

Implicit scheme and explicit scheme are both time discretization techniques [1]. The critical difference is that the implicit scheme requires the volume fraction values at the current time step, whereas the explicit scheme requires the volume fraction

values at the previous time step. Standard finite-difference interpolation is used for both scheme.

Implicit scheme includes QUICK, Second Order Upwind and First Order Upwind, and the Modified HRIC schemes. The equation is shown as the following (rewrote from [1]).

$$\frac{\alpha_q^{n+1}\rho_q^{n+1} - \alpha_q^n \rho_q^n}{\Delta t} V + \sum_f \left(\rho_q^{n+1} U_f^{n+1} \alpha_{q,f}^{n+1}\right) = [\sum_{p=1}^{n} (\dot{m_{pq}} - \dot{m_{qp}})]V \tag{2.20}$$

The formulation of explicit scheme does not require iterative solution of the transport equation during each time step [1]. It means that the explicit scheme has to compute the time-dependent solutions for each previous time step (rewrote from [1]).

$$\frac{\alpha_q^{n+1}\rho_q^{n+1} - \alpha_q^n \rho_q^n}{\Delta t} V + \sum_f \left(\rho_q U_f^n \alpha_{q,f}^n\right) = [\sum_{p=1}^{n} (\dot{m_{pq}} - \dot{m_{qp}})]V \tag{2.21}$$

When adding an additional phase to the model, a new variable-volume fraction of the phase is introduced, then these two or more fluids are considered not interpenetration [1]. In each control volume, if the cell is full of one fluid, then the variables and properties are representing the one fluid in the cell. If there is more than one phases, then the variables and properties are shared by the phases, it represents volume-averaged values of all the phases in the cell [1]. Based on the volume fraction of each of the phases in the cell, the appropriate properties and variables will be assigned to each control volume within the domain [1]. Once a cell is close to the interface of two phases (Figure 2.3), the geometric scheme (Figure 2.4) is used. Convection and diffusion fluxes through the control volume faces need to be computed and balanced with source terms within the control volume itself [1].

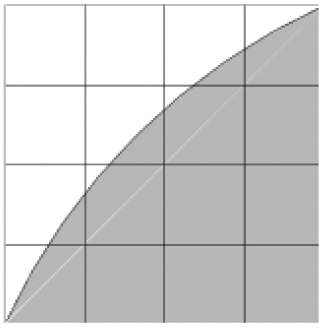

Figure 2.3: Actual interface shape, redrew from [1]

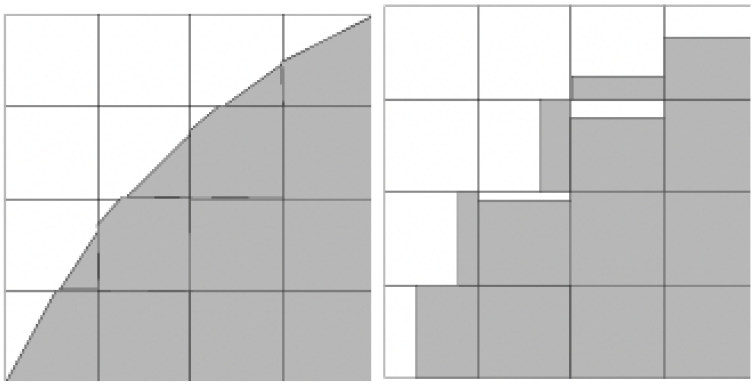

Geometric Reconstruction Scheme Donor-acceptor Scheme

Figure 2.4: Interface represented by different schemes, redrew from [1]

Geometric reconstruction assumes that the interface between two fluids has a linear slope within each cell and uses this linear shape for calculation of the advection of fluid through the cell faces [1]. It is very accurate, especially with microsized cells. To be noted, when the geometric reconstruction scheme is used, a time-dependent solution must be computed. Also, if you are using a conformal mesh (i.e., if the mesh node locations are identical at the boundaries where two subdomains meet), you must ensure that there are no two-sided (zero-thickness) walls within the domain [1].

Three steps of the geometric reconstruction [1]:

1. Calculate the position of the linear interface relative to the center of each partially-filled cell;
2. Calculate the advecting amount of fluid through each face using the computed linear interface representation and information about the normal and tangential velocity distribution on the face;
3. Calculate the column fraction in each cell using the balance of fluxes calculated during the previous step.

With the fluids' movement, it is important to keep track of the changes of properties. The properties in the transport equations are calculated by the presence of the component phases in each control volume [1]. In the two-phase system (water phase and oil phase), if the volume fraction of the second of these is being tracked, the density in each cell is given by (rewrote from [1]):

$$\rho = \varepsilon\rho_{oil} + (1 - \varepsilon)\rho_w \tag{2.22}$$

$$\rho = \varepsilon\mu_{oil} + (1-\varepsilon)\mu_w \tag{2.23}$$

There is a single momentum equation is used. It depends on the volume fractions of all phases through the density and viscosity, rewrote from [1]:

$$\frac{\partial(\rho v_i)}{\partial t} + \frac{\partial(\rho v_j v_i)}{\partial x_j} = -\frac{\partial p}{\partial x_j} + \frac{\partial \tau_{ij}}{\partial x_j} + F_{\sigma i} \tag{2.24}$$

$$\tau_{ij} = \mu \mid \frac{\partial v_i}{\partial x_j} + \frac{\partial v_j}{\partial x_i} \mid -\frac{2}{3}\mu\delta_{ij} div(\overrightarrow{v}) \tag{2.25}$$

If i=j, $\delta_{ij} = 0$, otherwise $\delta_{ij} = 1$.

The resulting velocity is shared by all phases. However, when the velocity difference among phases is too large, the velocity near interface would not be as accurate as they are within each phase. Another note in this equation is that when the viscosity ratio is greater than 1000, convergence will become difficult. VOF model treats energy (E) and temperature (T) as mass-averaged variables. The energy equation is shown below, rewrote from [1]:

$$\frac{\partial(\rho E)}{\partial t} + \nabla\cdot(\overrightarrow{v}(\rho E + p)) = \nabla\cdot(k_{eff}\nabla T) \tag{2.26}$$

The energy for each phase is (rewrote from [1]):

$$E = \frac{\sum_{q=1}^{n} \alpha_q \rho_q E_q}{\sum_{q=1}^{n} \alpha_q \rho_q} \tag{2.27}$$

Effects of surface tension along the interface can be included in the VOF model by specifying a surface tension coefficient. In ANSYS FLUENT, there are two surface tension models, namely the continuum surface force(CSF) and the continuum surface stress (CSS) [1]. CSF is the addition of surface tension to the VOF calculation results in a source term in the momentum equation; CSS avoids the explicit calculation of curvature and could be represented as an anisotropic variant of modeling capillary forces based on surface stresses [1]. CSS is slightly better to use than CSF, especially when variable surface tension is involved. The coefficient stands for the contact angles between the phases and the walls. The coefficient in this model is a constant. Surface tension coefficient is also an important factor in zero or near-zero gravity conditions [1].

Last but not least, there are three major dimensionless quantities are used to represent fluid in this simulations [1]:

- Reynolds Number $Re = \frac{\rho_w \ U \ d}{\mu_w}$

- Capillary Number $Ca = \frac{We}{Re}$
- Webber Number $We = \frac{\rho_w \ d \ U^2}{\sigma}$

2.4 Validation

Over the last three or four decades, computer simulations have been used in all scientific fields [64]. Because of its great impact on the modeling and simulation predictions, the credibility of the computational results get more and more important in the engineering designs, as well as in terms of public officials, and to those who are affected by the decisions that are based on these predictions [65]. This new scientific trend requires a user-defined and comprehensive verification and validation process. Figure 2.5 indicates a conceptual model and a computerized model which describe the relationship between the real world and prediction.

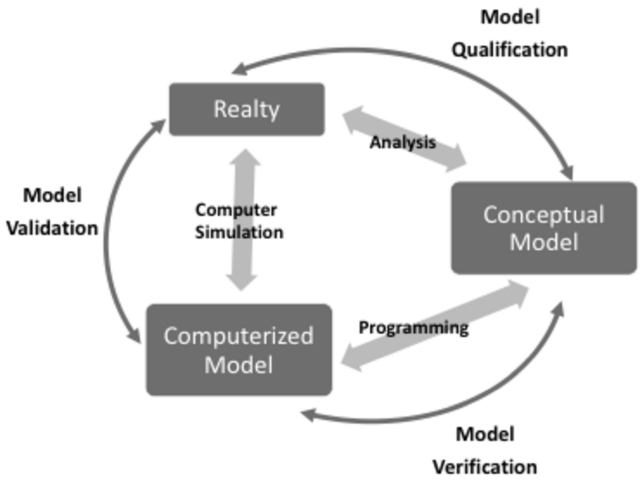

Figure 2.5: Model testing cycle, redrew from [4]

Verification is the process of evaluating the products of a software development phase to provide assurance that they meet the requirements defined for them by the previous phase. Validation is the process of testing a computer program and evaluating the results to ensure compliance with specific requirements [65]. Since we use the commercial software, ANSYS FLUENT to do the simulations. Coding verification is not presented. Oberkampf et al. [4] lists out standard procedure of

verification and validation for Computational Fluid Dynamics Simulations in Figure 2.6.

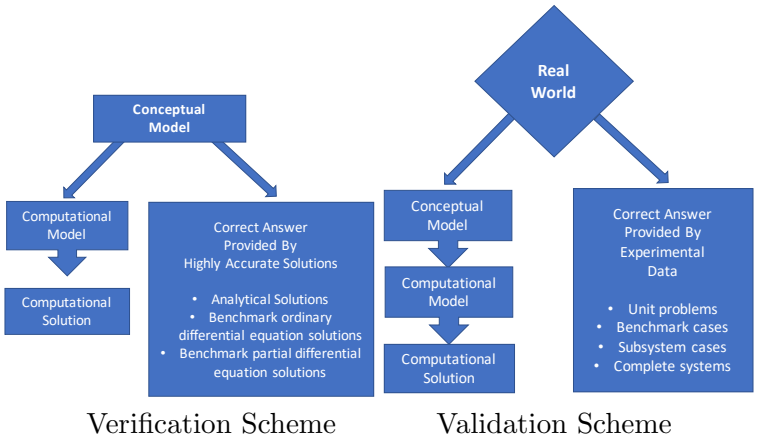

Figure 2.6: Verification and Validation testing procedures, redrew from [4]

Obviously, all CFD simulations demand high qualitative validation experiments. It is the essence to ensure that the results delivered are accurate and reliable. The process of validation is not simple like plotting an experimental data on a graph [65]. Its inadequacy especially affects complex engineered systems that heavily rely on computational simulation for future predicted performance, reliability, and safety. Such complexities of the quantification of verification and validation are substantial, from both a research perspective and a practical perspective [65]. The strategy does not include assumption of absolute true experimental measurements. The experimental data is treated as the most faithful reflection of the realty. Meanwhile, the computational data is the theoretical faithful result.

Back to present issue, it is important for this simulation is a comprehensive knowledge of the fluid behavior and interaction with particles within the aqueous medium. It is commonly recommended to start with a simple model first. Following by adding more detail and complexity as needed until reaching a representative model [1]. The first set of validation is to valid the simplest case, which only contain one solid particle within air. Different inlet velocities are applied to this single particle. With known velocities, particle size, air properties and steady surrounding condition, it is expected to obtain the drag coefficient curve for spheres. The solid particle is a 2D sphere with diameter of 0.00426 m. Particle is surrounded by air with constant temperature of 15 C (288.16 K). The solid sphere is made of aluminum with density of $2719 kg/m^3$ that is not reacted with air. The properties of air are shown below.

Table 2.1: Aerial phase properties

	ρ_{air}	μ_{air}	Temperature	Specific Heat Ratio
Fluid	(kg/m^3)	(kg/m s)	K	
Air	1.22	1.79×10^{-5}	288.16	1.4

ANSYS FLUENT [1] is used to perform such simulation and deliver force flux under each inlet velocity. The starting value of velocity is 0.00001 m/s and increases up to 0.1 m/s. In this case, the influence of buoyancy and gravity are not considered, due to a small particle size. As the inlet velocity increases, the drag force is getting larger. The SIMPLE scheme and QUICK momentum are used as solution method; run up to 20,000 iterations; reporting value for every interval. The table below shows the final results. Next, we plot the experimental data with the log-log plot, then compare with the theoretical curve of drag coefficient for a sphere. The results match with each other, shown in Figure 2.7. The first model is validated.

Table 2.2: Inlet velocity and drag force data

Velocity (m/s)	Reynolds Number	Drag Force	Drag coefficient
$\nu(m/s)$	$Re = \frac{\rho_{air}\nu d}{\mu_{air}}$	$F_d(N)$	$C_d = \frac{2F_d}{\rho_{air}\nu^2\pi(\frac{d}{2})^2}$
10^{-5}	2.92×10^{-3}	5.34×10^{-12}	6088.09
5×10^{-5}	1.46×10^{-2}	2.61×10^{-11}	1192.48
10^{-4}	2.92×10^{-2}	5.33×10^{-11}	608.41
5×10^{-4}	1.46×10^{-1}	2.63×10^{-10}	120.08
10^{-3}	2.92×10^{-1}	5.37×10^{-10}	61.27
5×10^{-3}	1.46	3.02×10^{-9}	13.77
10^{-2}	2.91	6.73×10^{-9}	7.68
5×10^{-2}	14.58	5.14×10^{-8}	2.34
10^{-1}	29.16	1.33×10^{-7}	1.51

2.4.1 Validation Test of CFD Model

This section presented the validation of CFD results for a spherical solid particle covered by a thin oil film within an aqueous phase. The model is validated against the benchmark experimental data in Mehrabian et al.[2]. The experiment is to evaluate the factors which affect oil separation process from a single aluminum spherical particle falling through an aqueous solution. The resultant function depends on viscosity ratio, oil film thickness and interfacial tension [30]. The main objective is identical with the modeling presented in this work. Unlike to the experiment, we use a characterized Reynolds number to represent the separation stages. In this

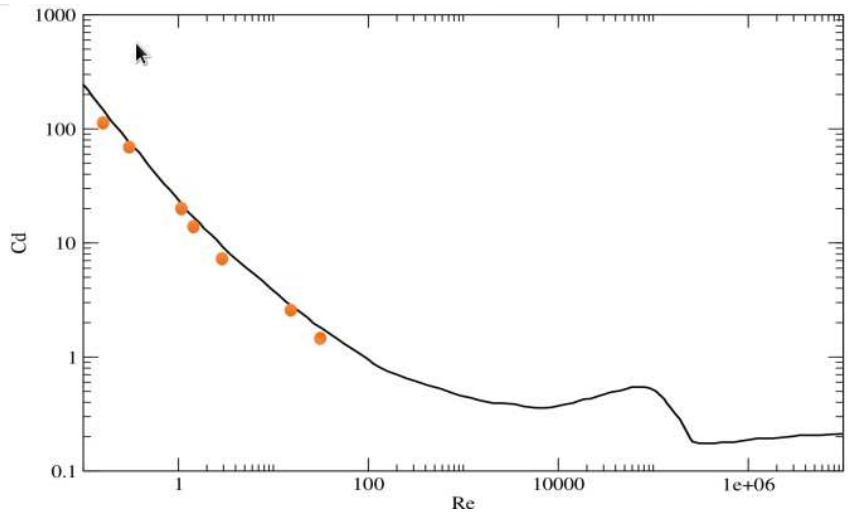

Figure 2.7: Frictional drag coefficient as a function of the Reynolds number for spheres [solid curve is extracted from Lapple and Shepherd's experiment [5]; dot points are CFD-based calculations carried out in this work using ANSYS FLUENT].

validation case, we have selected Re of 0.1 to compared with the experimental data. The physical and chemical properties of the particle, oil and water in the validation experiment and numerical modeling are the same and summarized in the Table 2.3. The experimental apparatus setup is shown in Figure 1.5.

In [30], a set of high-speed video of oil-coated solid spheres falling through an aqueous solution is analyzed. In order to compare with the literature data, we have aimed to determine the amount of oil being separated and the changing velocity of the coated sphere over certain period of time. A new equation 2.28 to calculate particle-based capillary number based on a low-Reynolds number solution is introduced. An important parameter "g" is a function of viscosity ratio and oil thickness. The following equations are all rewrote from [30].

$$Ca_p = \frac{\mu_1 U_\infty}{\sigma} g(\varepsilon, p) \tag{2.28}$$

where,

$$g(\varepsilon, p) = \frac{4\varepsilon^3 + 15\varepsilon^2 + 15\varepsilon}{2(4\varepsilon^3 + 15\varepsilon^2 + 15\varepsilon + p(20 + 30\varepsilon + 18\varepsilon^2 + 4\varepsilon^3))} \tag{2.29}$$

$$\varepsilon = \frac{h}{R_0} \tag{2.30}$$

$$\mu_1 = 2.65\gamma^{n-1} \tag{2.31}$$

Table 2.3: Data collected from [2]

Property	Magnitude	Unit
Mass of oil	11.73×10^{-6}	kg
Thickness of oil (h)	0.19	mm
Diameter of sphere (D_0)	4.26	mm
Volume of solid	40.48	mm^3
Diameter of droplet	4.65	mm
Volume of droplet	52.57	mm^3
Volume of oil	12.09	mm^3
Density of water	1040	kg/m^3
ε	0.091	
g	0.22	
Oil fraction	0.23	
Density of oil	970	kg/m^3
Density of steel solid	8302.7	kg/m^3
Viscosity of oil (μ_2)	0.097	Pa.s
Viscosity of solution (μ_1)	1.17	Pa.s
Viscosity ratio ($p = \frac{\mu_2}{\mu_1}$)	0.08	
Temperature	25	C
Interfacial tension (σ)	36	mN/m
Equilibrium interfacial tension	27.61.4	mN/m
Contact angle (θ)	90	degree

Equilibrium interfacial tension is given as:

$$\sigma = 2.65\gamma^{0.7} \tag{2.32}$$

The original Capillary equation is given as:

$$Ca_p = \frac{\mu_1 U_\infty}{\sigma} \tag{2.33}$$

In [30], the steady Stokes' flow of a viscous, incompressible Newtonian fluid (phase 1-water) past a droplet (phase 2-oil) containing an internal droplet (phase 3-solid). The oil-coated sphere is observed and analyzed by MATLAB image processing toolbox. From the experimental results, there is a critical Cap=0.4 when p=0.08 with taking the oil film thickness into account [30]. The velocity of an oil-coated sphere is higher than the velocity of an oil-free sphere due to the lubrication effect of the oil layer, shown in the Figure 2.8.

Different from the actual experiment, in the VOF modeling, only a constant inlet velocity is used. Thus, we have applied 0.07 m/s, as it is close to the average

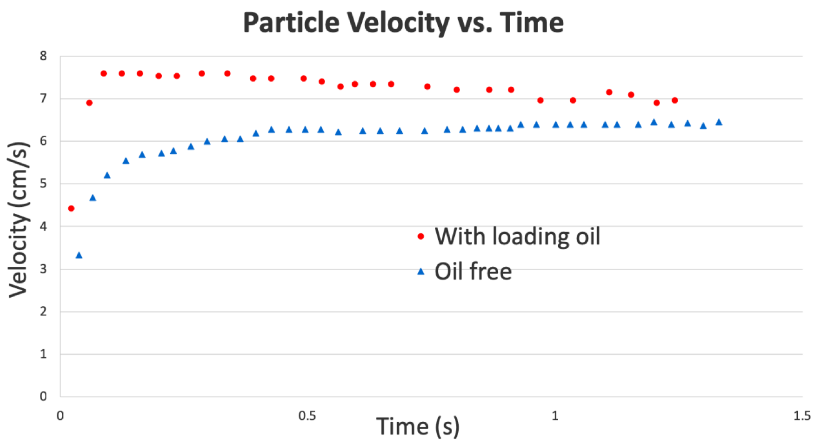

Figure 2.8: Experimental data of the particle velocity versus time, results regenerated from 'Oil-Particle Separation in a Falling Sphere Configuration' [2] by using WebPlotDigitizer

particle velocity. The CFD velocity change controls within a $3 * 10^{-7}$ range, as given in the Figure 2.9. In [30], a free falling droplet was used which reveal the fact of changing velocity with a constant gravitational acceleration.

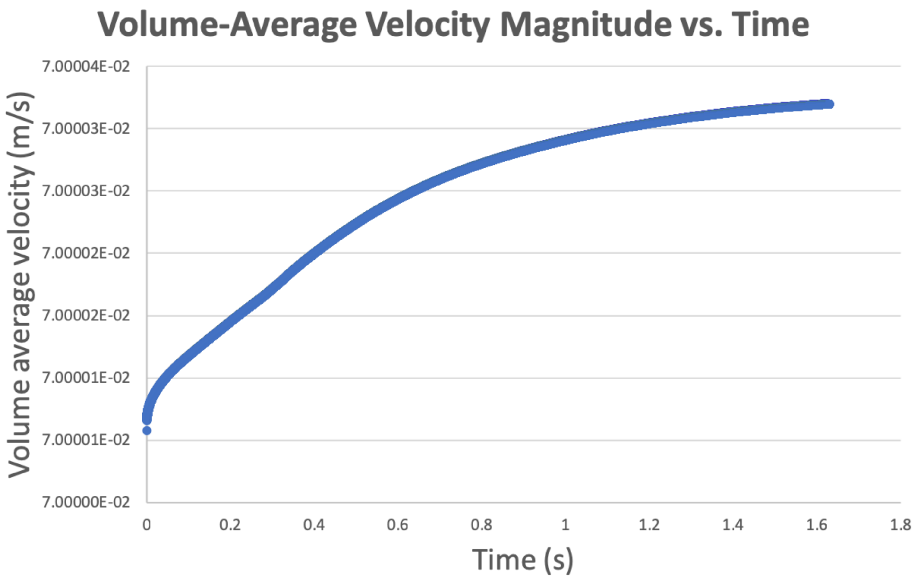

Figure 2.9: CFD result of volume average velocity versus time

We have excluded the data before 1s in the experimental curve 2.10, as the tail begins to form only about 1s after release [2]. In order to make these two sets of

data comparable, we start all data plot at 1s 2.11. The literature result is plotted into the curve 2.10

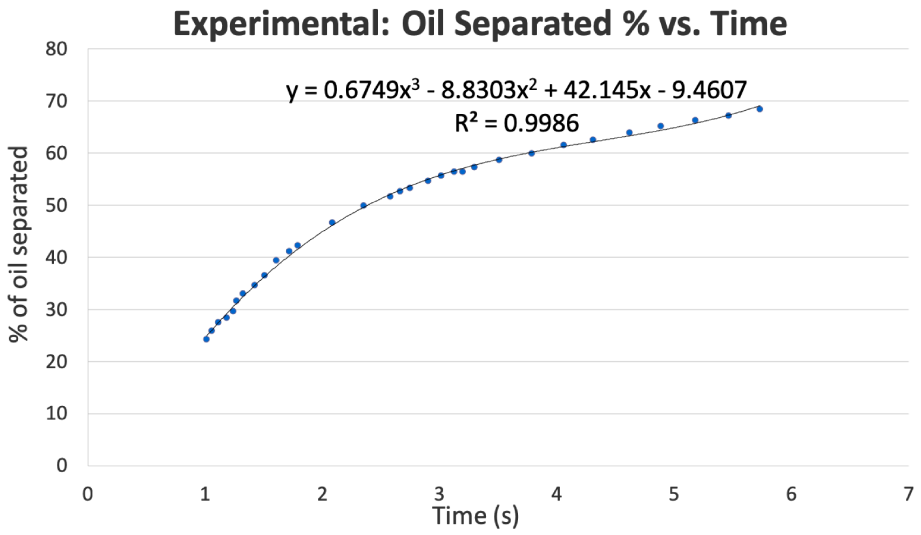

Figure 2.10: Experimental data of the percentage of oil separated versus time, results regenerated from [2] by using WebPlotDigitizer

The CFD result is plotted into the curve 2.11.

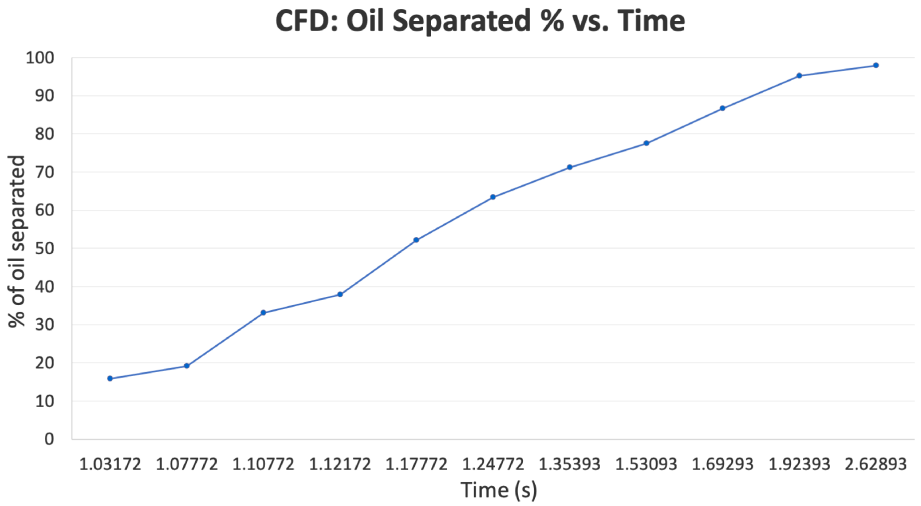

Figure 2.11: CFD result of the percentage of oil separated versus time, results generated from FLUENT ANASYS [1]

Both graphs indicate the same trend, but different values. It is due to a combination of different reasons. First of all, the experiment in the literature defines the

percentage of oil separated as the portion which is exclusive of elongated oil tail.

However, in the VOF modeling, the interface between oil and aqueous phase is a bit ambiguous than the actual experiment. Even the current mesh CV is very fine (control volume of 130,000), it is still hard to distinguish the point where the tail got broken up. Thus, for the purpose of validation only, we defines the percentage of oil separation in a different way. All CFD percentage of oil separated is calculated the difference from the initial state as Figure 2.12. This explains the large and inconsistent difference between the volume of oil separated in the experiment and CFD model. The difference is actually part of oil tail.

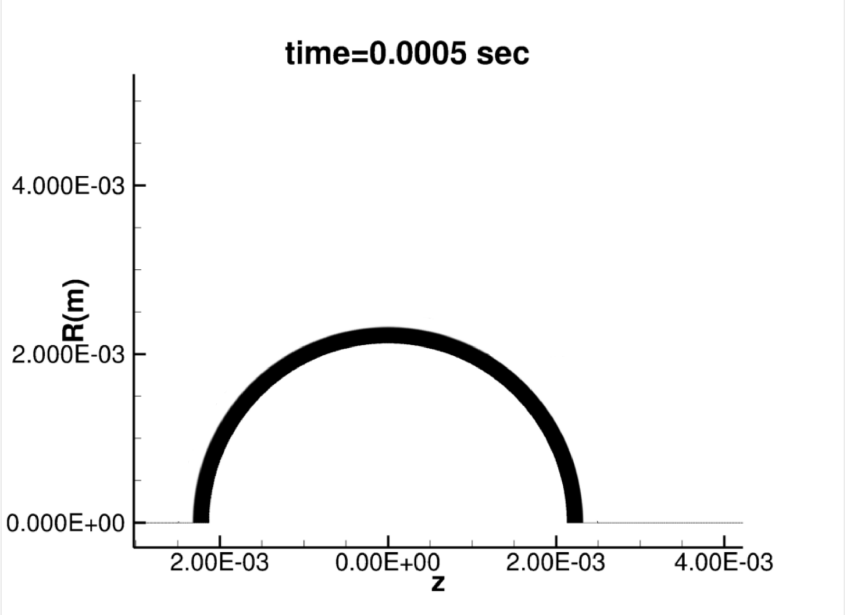

Figure 2.12: Snapshot of the initial oil status of CFD model at time 0.0005 s

Secondly, the average velocity in the CFD model has always been a bit larger than 0.07 m/s which is faster than the particle velocity in the experiment. In the reality, a free-falling droplet has a changing velocity versus time. As the oil being separated from the droplet, the overall droplet mass will decreases. Then the velocity and shear stress change variously. This is another major contribution to the difference between CFD and experimental results. Conversely, modeling has a constant 0.07 m/s velocity inlet at all times. This maintains a more stable rate than the experiment. When the tangential velocity reaches the highest point, the separation process is at a relatively rapid rate. In the CFD modeling, such rapid process happens from about 1.5 s to 1.8 s. This curve reflected the portion of 1-2 s in the experiment.

Thirdly, when transferring a 2D simulation results into a 3D problem would cause some bias. The method of calculating the oil separated volume in this CFD model is not super accurate, since there is no volume data given by the software automatically. When calculating by hands with predicting resultant shapes of a liquid phase is challenging. The general method can be described into four classifications.

1. Starting stage: Due to the small amount changing in the beginning, it is easy to get oil removed on the surface. As Figure 2.13, we have calculate the removed portion by estimating the shape to be a half ring. Then the volume would be half of the difference between two circles with radius of 2.32 mm and 2.20 mm.

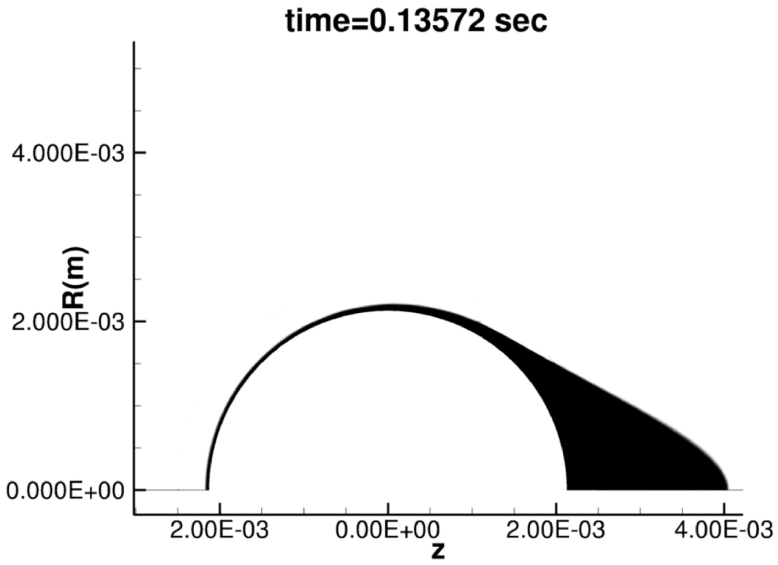

Figure 2.13: Snapshot of the oil status of CFD model at time 0.13572 s

2. When the tail just formed, and no oil drops formed yet: The total volume is divided into two shapes. As Figure 2.14, the red portion is assumed to be a ring shape, also can be calculated by getting the difference between two circles with radius of 2.13 mm and 2.22 mm. Another blue part is assumed to be a cylinder with height of (2.32-2.22=0.1 mm) and the radius of the oil tail's height around 1.1 mm.

3. Once some small oil drops formed and remained on the surface, as Figure 2.15: In the case, it is easier to estimate the total oil remained on the surface by adding all oil drops' volume plus the portion of the tail which lays in the original circle (radius of 2.32 mm). This portion's shape is assumed to be cylinder with the height of original oil film thickness (0.19 mm) and the radius of tail's height.

4. The last method is used to verified the overall results: Assuming the elongated

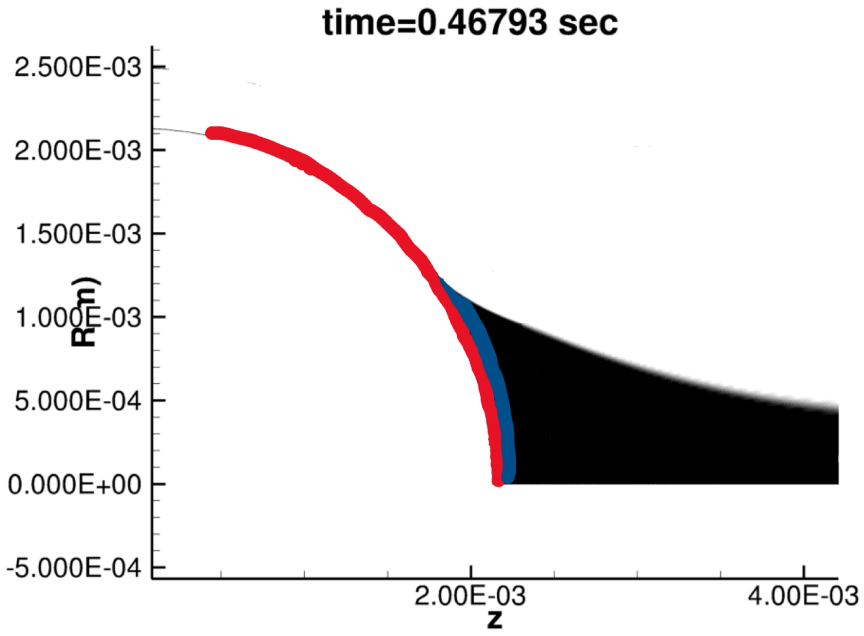

Figure 2.14: Snapshot of the oil status of CFD model at time 0.46793 s

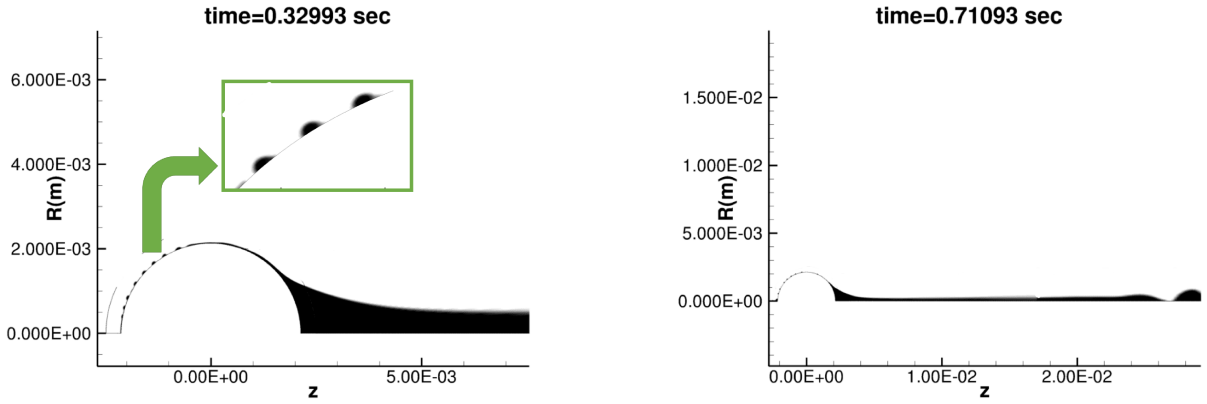

(a) (b)

Figure 2.15: Snapshots of CFD model at time = (a) 0.32993, (b) 0.71093 seconds

oil tail has a cone shape, then adding other oil drops' volume, as shown in Figure 2.16.

The Table 2.4 summarized all CFD data based on the methods introduced above. The error percentage is between $3-4$. It should be noticed that use of the VOF model to predict the oil separation from a spherical droplet movement pattern in

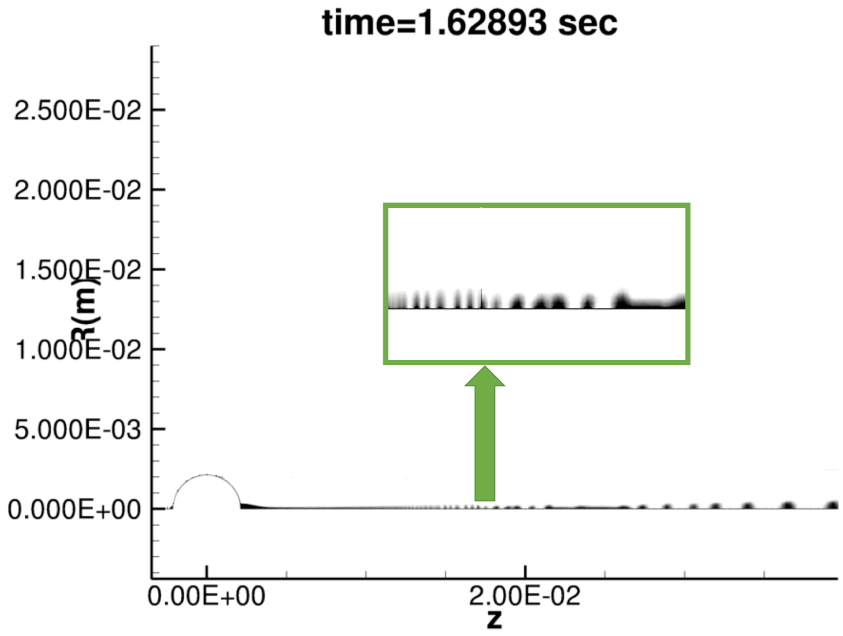

Figure 2.16: Snapshot of the final status of CFD model at time 1.62893 s

such aqueous solution gives comparable results and less time consuming. Meanwhile, with the simulations, we get detailed information about the characteristics of each phases and oil location within nano-second-scale. The disadvantage provided by this CFD model is to predict the arbitrary shaped oil drops.

Table 2.4: Data collected from FLUENT ANASYS

Time	Adjusted time	Volume	Percentage of oil separated
s	s	mm^3	
0.03	1.03	1.93	15.92
0.08	1.08	2.31	19.11
0.11	1.108	4.10	33.09
0.12	1.12	4.59	37.92
0.18	1.18	6.31	52.19
0.25	1.25	7.66	63.36
0.35	1.35	8.62	71.27
0.53	1.53	9.37	77.51
0.69	1.69	10.48	86.68
0.92	1.92	11.51	95.18
1.63	2.63	11.83	97.87

2.5 Conclusions

There are several numerical methods to model water or oil droplet within multi-phases, such as CLSVOF, CSF, VDROP and VOF. Generally speaking, the numerical modeling is a more effective and comprehensive alternative than actual experiments. VOF is chosen as the modeling method in this study. In summary, when applying the same case with the literature, the numerical simulations provide a good agreement with the literature results. Except the one offset is observed in the graph of oil separated percentage versus time. This disagreement is caused by different definitions on the portion of oil being separated; the velocity changing difference between modeling and experiment; the bias from transferring 2D problem into 3D problem. Another important observation is when Re is much less than 1, the complete separation occurs when the water phase has a higher viscosity than oil phase. The optimum viscosity ratio in this case is 0.08. The optimum particle Capillary number is 0.4.

Chapter 3

Modeling and Applications

3.1 2D Modeling for Single Droplet

In this chapter, we start the validation of the 2D multiphase case. The principal scheme is a single particle being placed in a relative large rectangle. The size of the two- dimensional computational domain is 0.01 m by 0.004 m as shown in Figure 3.1, where the initial diameter of the solid particle is 100 μm with the oil thickness of 17.8μm. Fining mesh is one of the key steps. An acceptable mesh must be comparable with the interface between fluids. The initial temperature of the water is 288.16 K (15°C) and to be constant going forward. The top and the bottom boundaries apply symmetrical boundary conditions and the left boundary applies velocity inlet conditions, respectively.

Table 3.1: Sphere dimension

Diameter (μm)	Oil Thickness(μm)	Oil Radius (μm)	Oil Fraction
100	17.86	135.72	0.6

Next, we proceed with a description of the water and oil properties used in the simulations. The water properties have non-linear dependencies on the temperature, which has not to be taken into account in the modeling because we have a constant temperature in this case. It is well-known that most separation techniques involve adding solvent to decrease the density and viscosity of the oil phase. Thus, another simplification is assuming that water and oil have the same density ($1000 kg/m^3$) and viscosity (1 mPa·s). The ratio of oil to (oil + particle) volume is set to 0.6. We have used 90 degree for the contact angle; it has been agreed that oil will be difficult to remove when the contact angle is smaller while everything else being equal [66]. The 2D model does not need to specify the vertical inlet velocity direction. Meanwhile,

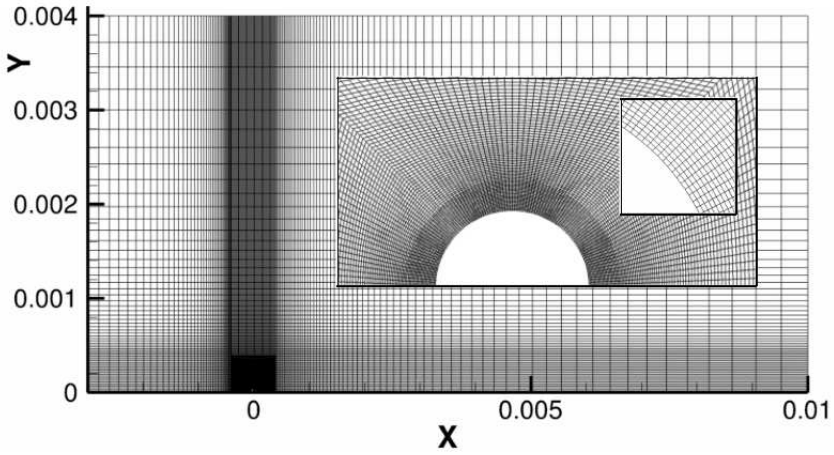

Figure 3.1: Numerical two-dimensional and axisymmetric mesh; X responding to Z axis and Y responding to R (radius); both are in the unit of meters.

we assume a constant interfacial tension σ of 72 mN/m between oil and water. Both the Reynolds number and the Capillary number are essential parameters to determine surface tension. After a series of simulations, there are two critical factors promoting oil/particle separation, namely, the Reynolds number and the contact angle.

3.1.1 Changing Reynolds Number

As Re increases, it results in different inlet velocities. Re represents flow patterns in different fluid flow conditions. While keeping the same droplet model, we apply different inlet velocities to the oil-coated particle. Since we have laminar flow, the starting value of Re is considered to be 1. In this case, the influence of buoyancy and gravity are not considered, due to the small particle size. In order to achieve a complete oil separation from the particle, we apply different velocities and observe the interface movement. The SIMPLE scheme and QUICK momentum as a solution method run up to 200,000 iterations with a time step of $1\mu s$. As a first step, the mesh contains around 22,000 cells first.

In ANSYS [1], different colors indicate the percentage of saturation of each phase. To simplify this, we used a two-color system in which black indicates the oil phase and white indicates the water phase. Figure 3.2 illustrates the different phases and oil movement.

As a result, we ended up reproducing some simulations similar to Fan et al. [66]'s experiment in 2010. However, we also found some differences. At the low inlet velocity (Re=1) in Figure 3.3, the oil film does not move away from the particle due

Table 3.2: Different Re results different velocity

Velocity (m/s)	Reynolds Number	Capillary Number
$\nu(m/s)$	$Re = \frac{\rho_{air}\nu d}{\mu_{air}}$	$Ca = \frac{\mu\nu}{\sigma}$
0.01	1	1.39×10^{-4}
0.02	2	2.78×10^{-4}
0.03	3	4.17×10^{-4}
0.05	5	6.94×10^{-4}
0.1	10	1.39×10^{-3}

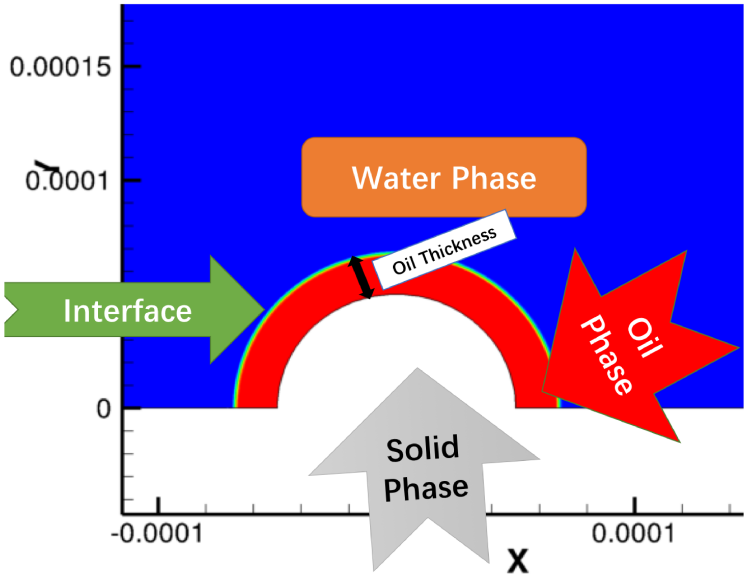

Figure 3.2: Multi-phase scheme

to an insufficient shear force.

De-wetting occurs when inlet velocity reaches 0.02 m/s (Re=2). The snapshots of the simulation shown is Figures 3.4, when Re = 3 with a contact angle of 90^o. The oil portion partially moves downstream. Note that there is a backward motion of the oil droplet moving to the particle in separation. The oil portion sticks to the surface if no other forces are applied, which is caused by a sudden pressure drop between the oil and the particle. The similar movement is shown in Figures 3.5, when Re = 5 with a contact angle of 90°. Finally, a complete separation happens only when Re is approximately 10, as shown in Figures 3.6; in this situation, the oil moves away from the particle permanently.

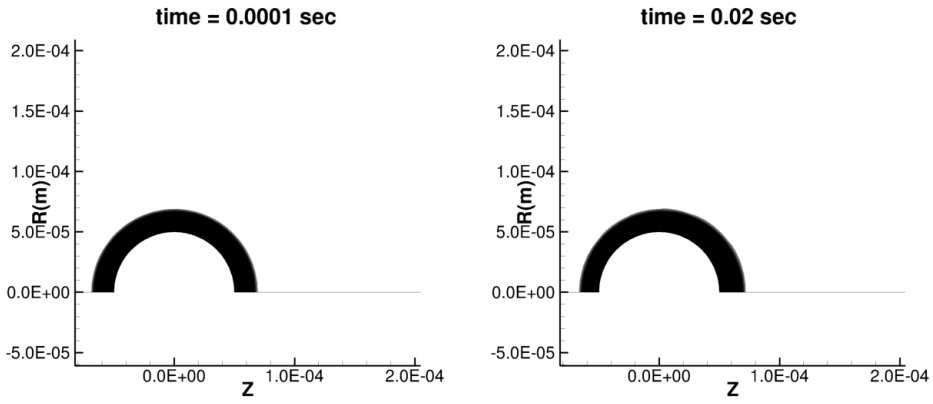

Initial status Final status

Figure 3.3: No oil movement over the times when Re=1

3.1.2 Changing Contact Angle

The second critical factor is the contact angle between the particle and the oil film. In the previous section, 90 degrees is used and is kept as a constant for all simulations. In the following simulation, $0/90/170^o$ of contact angle are applied to the model and observed. The basic motivation for changing the contact angle is to create both hydrophilic and hydrophobic fluids. Chemical coatings are either hydrophilic or hydrophobic [67]. Surfaces with a high contact angle (i.e., greater than 150^o) are defined as hydrophobic while surfaces with a low contact angle (i.e., under 30^o) are hydrophilic [68]. As Figure 3.7 shows below, the contact angle is defined as the interaction angle between the particle surface and the liquid phase [69]. The contact angle is also called a wetting angle [70]. It represents the wettability of a solid by a liquid.

In this work, considering the particle surface and oil phase are shown below as Figure 3.8 and Figure 3.9 separately.

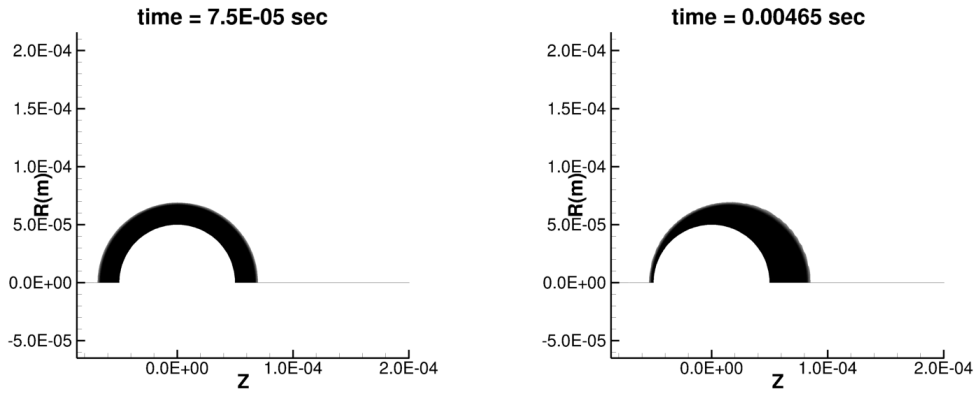

(a)

(b)

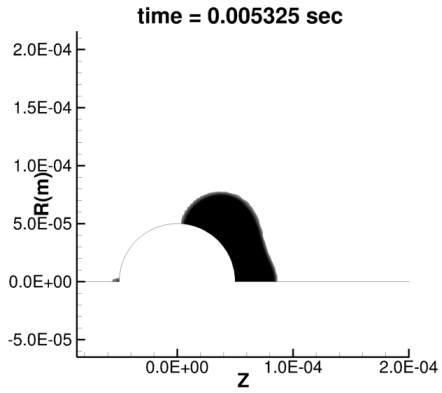

(c)

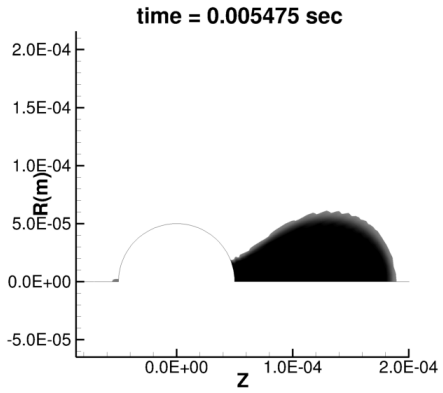

(d)

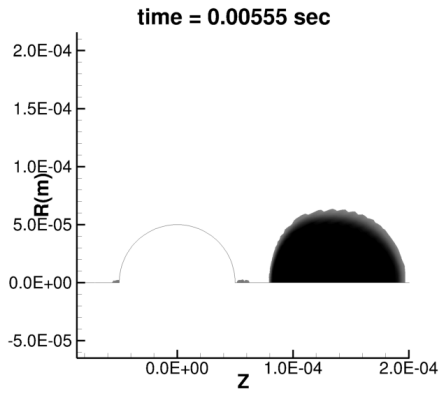

(e)

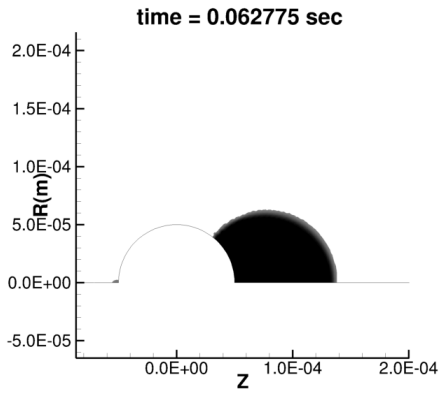

(f)

Figure 3.4: Snapshots of the multi-phase plot of oil movement over the particle when Re=3 at time = (a) 0.000075, (b) 0.00465, (c) 0.005325, (d) 0.005475, (e) 0.00555, (f) 0.062775 seconds

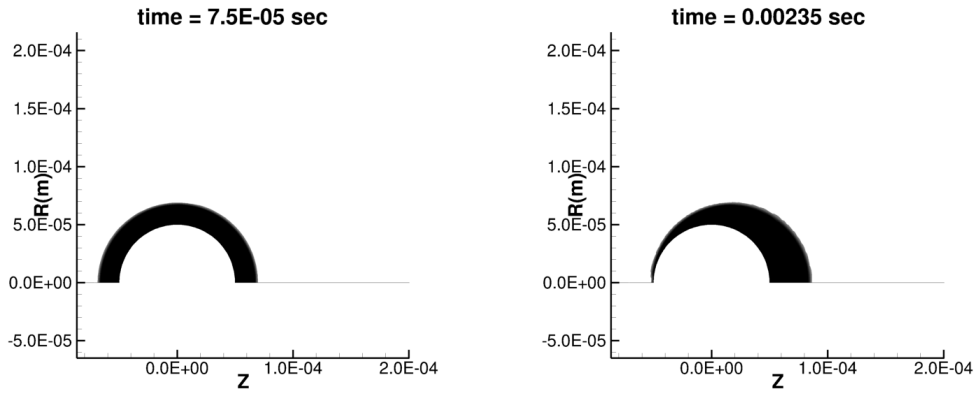

(a)

(b)

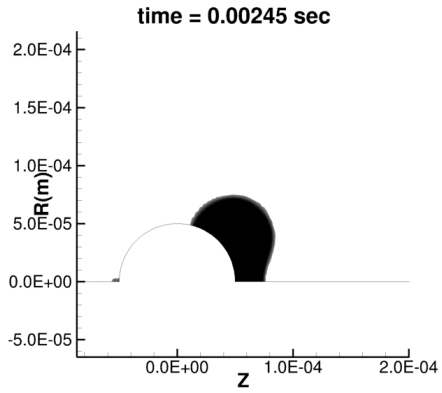

(c)

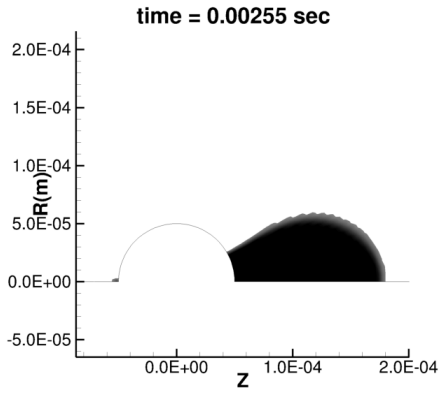

(d)

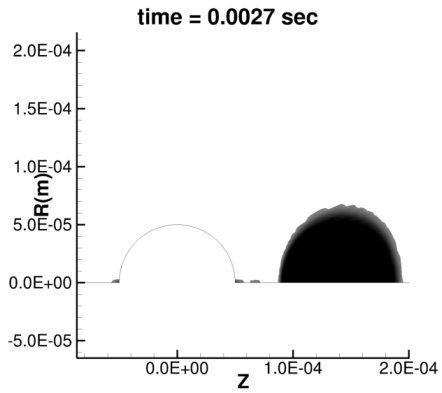

(e)

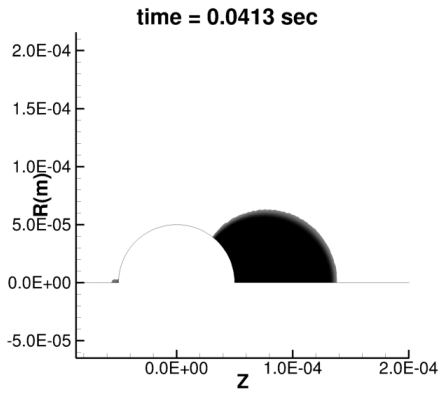

(f)

Figure 3.5: Snapshots of the multi-phase plot of oil movement over the particle when Re=5 at time = (a) 0.00005, (b) 0.00235, (c) 0.00245, (d) 0.00255, (e) 0.0027, (f) 0.0413 seconds

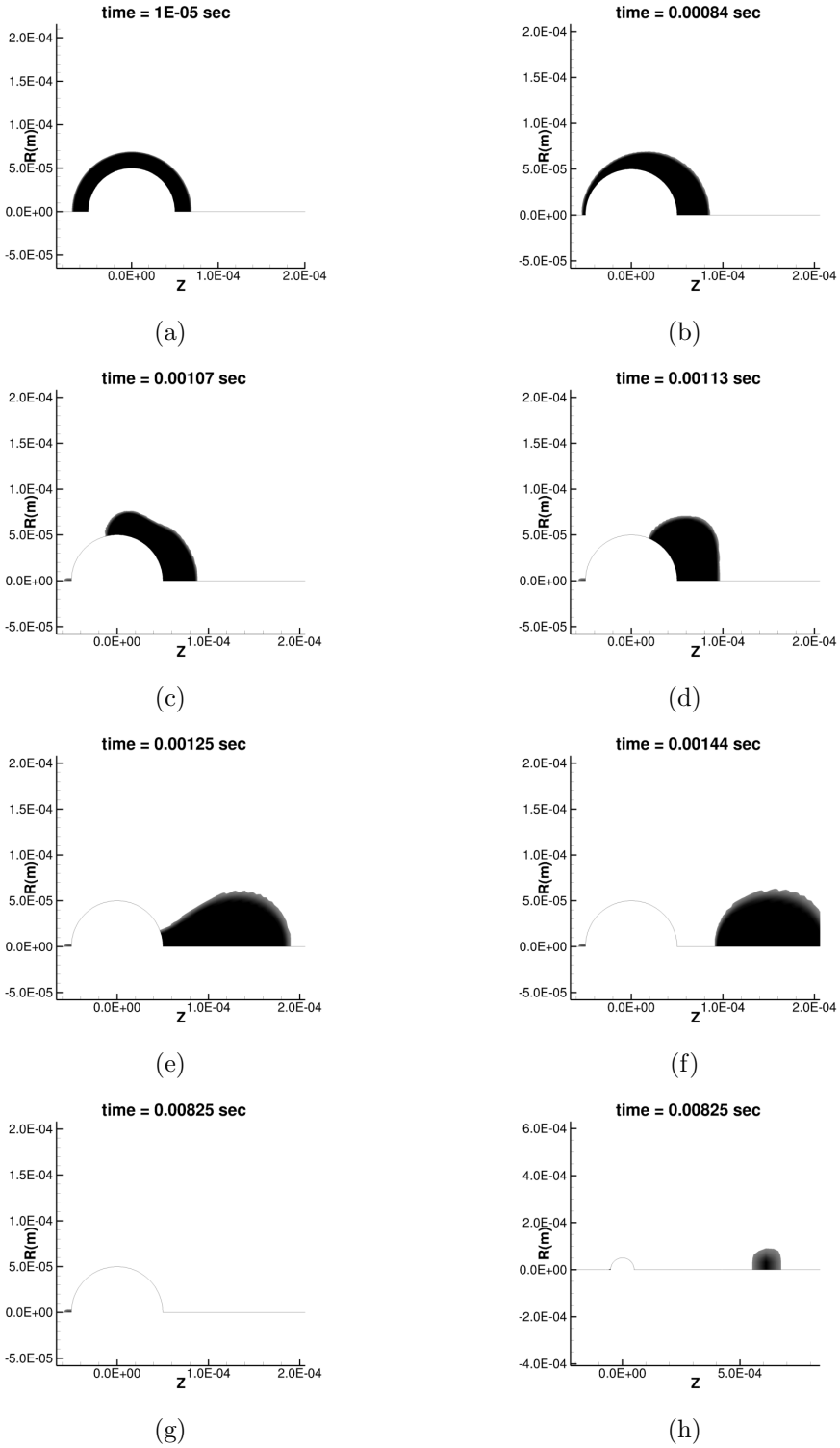

(a) (b) (c) (d) (e) (f) (g) (h)

Figure 3.6: Snapshots of the multi-phase plot of oil movement over the particle when Re=10 at time = (a) 0.00001, (b) 0.00084, (c) 0.00107, (d) 0.00113, (e) 0.00125, (f) 0.00144, (g) 0.00825 zoom-in, (h) 0.00825 zoom-out seconds

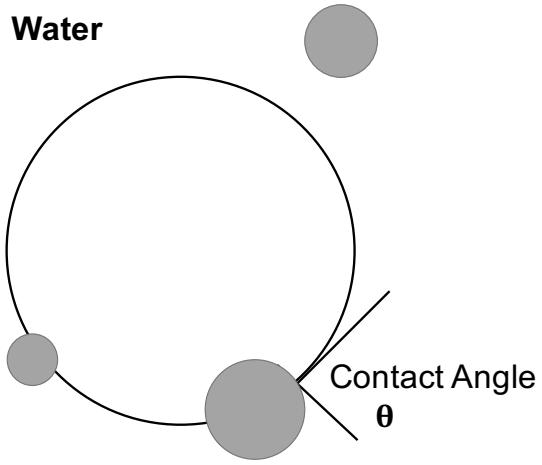

Figure 3.7: Schematic bubble-surface configuration

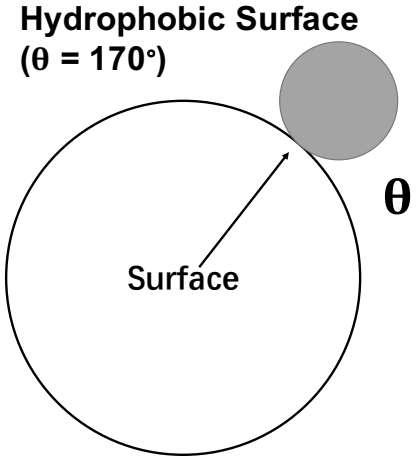

Figure 3.8: Schematic hydrophobic oil-particle surface configuration

In this chapter, the whole domain is fully refined from 22000 Control Volume Cells to 88000 Control Volume Cells in Figures 3.10. The whole domain is about 4 times finer than the previous mesh so that a much more accurate result would be delivered. It aims to find out how it reacts when the contact angle changing among 0/90/170 ^{o}. This model uses the same numerical methods and dimension of the oil-coated particle as well as the surrounding conditions. Thus, the only variable is the contact angle.

After all simulations, the following figures are generated by ANSYS FLUENT combined with TEC360 (Tecplot, Inc.). De-wetting does not occur when the contact angle is 0 ^{o}. De-wetting starts to occur when the contact angle is 90 ^{o} with the oil being initially separated. Meanwhile, there is a backward motion of the oil moving

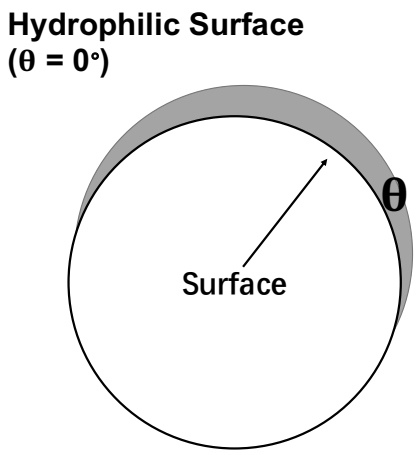

Figure 3.9: Schematic hydrophilic oil-particle surface configuration

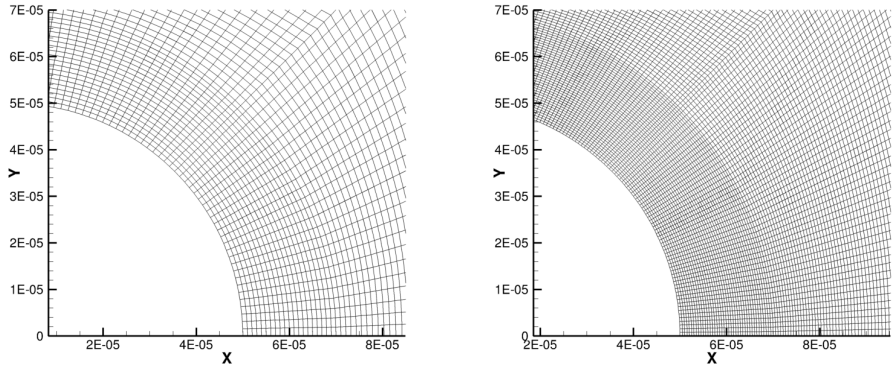

Grid size of mesh with 22000CV cells Grid size of mesh with 88000CV cells

Figure 3.10: Comparison of two meshes; X responding to Z axis and Y responding to R (radius); both in meters

to the particle at around 0.00213 s. The oil portion remains connected to the surface if no other forces are applied. This bounce-back phenomenon will be discussed in the next section. The complete separation occurs when the contact angle is 170 ^{o}; in this situation, oil moves away from the particle permanently. For the purpose of simplification, based on the previous section, we identify three physical stages of oil separation from a solid particle within water phase, including no separation Fig. 3.11, pseudo-separation Fig. 3.12, and complete separation Fig. 3.13. Full sets of simulation figures will be in the Appendix section. The characteristics of these periods are carefully studied by viewing the velocity vector map in the following section. Numerical results are shown below.

Based on the results, it is reasonable to assume that hydrophobicity is another

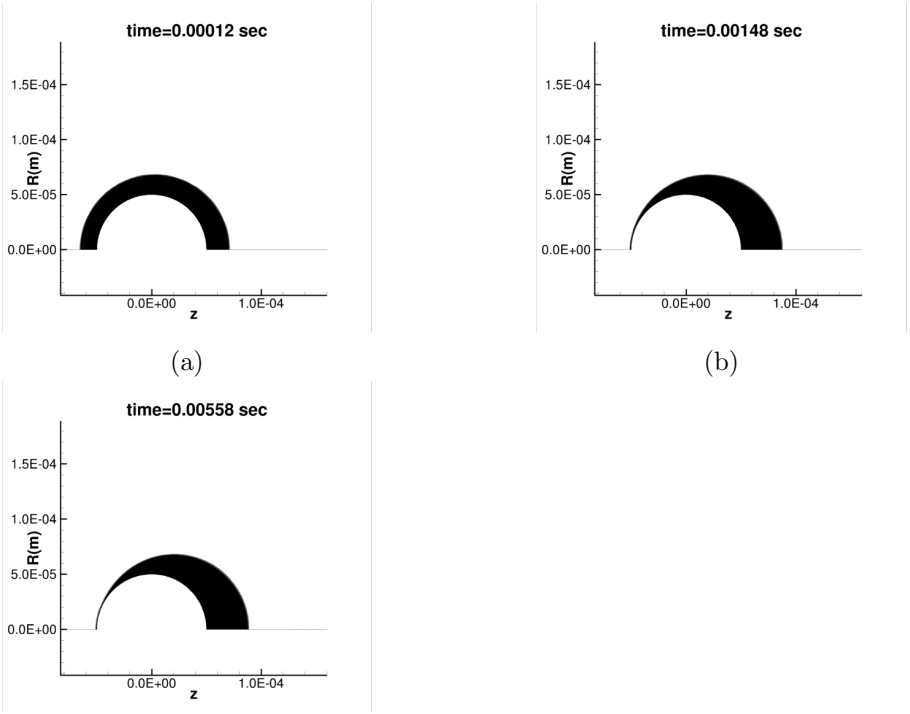

Figure 3.11: Snapshots of the multi-phase plot of oil movement over the particle when Re=10, contact angle is 0 degree at time = (a) 0.00012, (b) 0.00148, (c) 0.00558 seconds

important factor in oil separation. The greater the hydrophobicity of the contact surface, the easier the separation process would be. Another oil-water separation experiment shows the same the result in Sann et al. [71]. The experiment tested ZIF-8 (zinc-methylimidazolate framework-8) to remove oil from water. The study was aimed to support oil removal from the water surface and exhibited strong hydrophobicity with a water contact angle of 142°, ZIF-8 particles combined with highly hydrophobic and superoleophilic properties [71]. A tea bag was made up containing the surface-modified sample and selected oil-water mixture; Sann et al. [71] gently placed the tea bag on the surface of the oil on the Petri dish. They found that the oil portion was completely mopped up by the tea bag leaving behind just water [72]. In all the experiments, the oil to water weight ratio was maintained at 1:10. The experiment results showed that the highly hydrophobic ZIF-8 particles can be used in oil-water separation [71]. Furthermore, this ZIF-8 tea bag can be reused for up to twenty cycles. The tea bag allows the oil to be readily removed from the surfaces of particles through heating combined with a reduced pressure treatment. Its potential applications are similar to our objectives: cleanup of oil

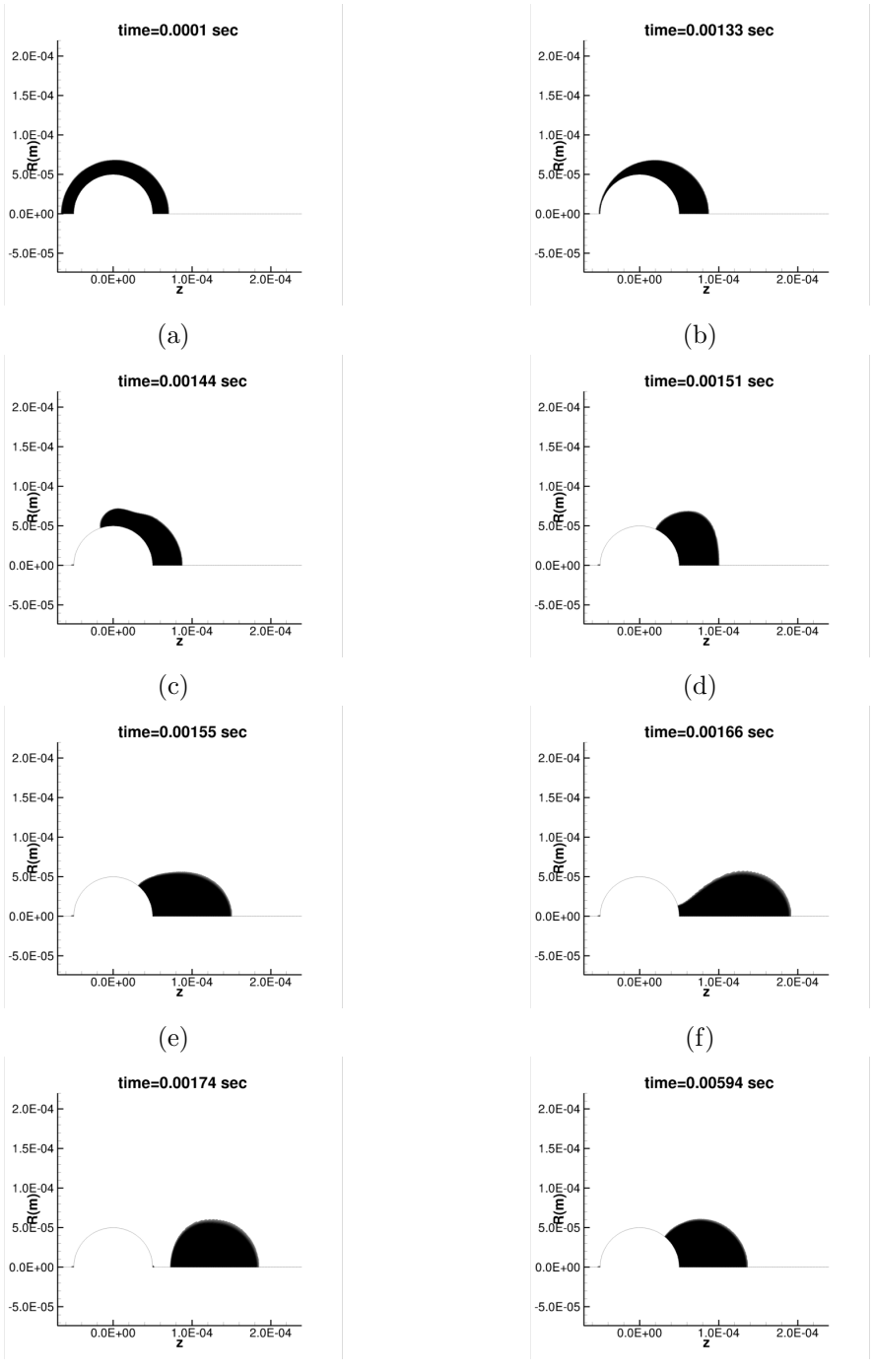

(a) (b) (c) (d) (e) (f) (g) (h)

Figure 3.12: Snapshots of the multi-phase plot of oil movement over the particle when Re=10, contact angle is 90 degree at time = (a) 0.00001, (b) 0.00133, (c) 0.00144, (d) 0.00151, (e) 0.00155, (f) 0.00166, (g) 0.00174, (h) 0.00594 seconds

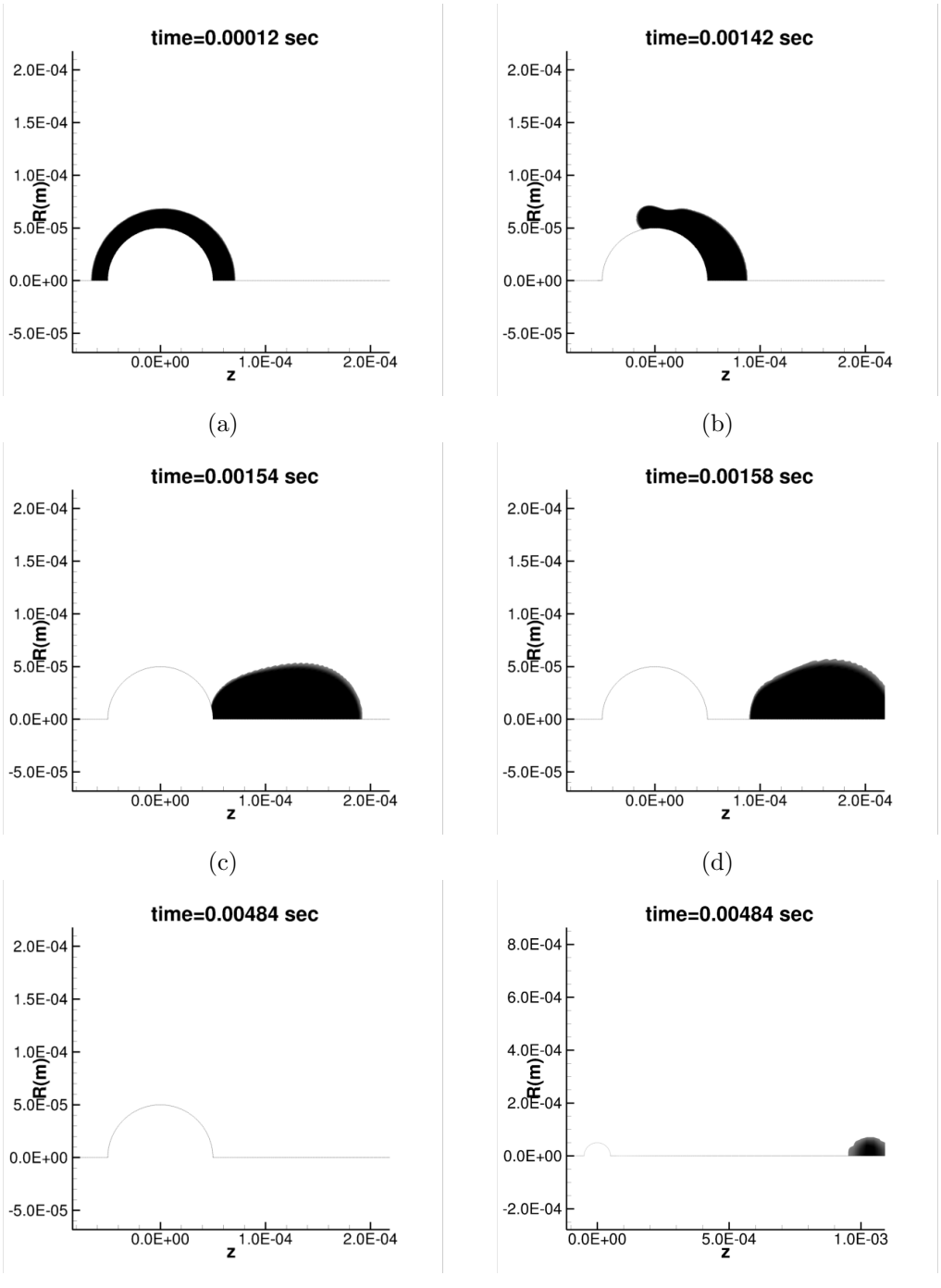

(a) (b) (c) (d) (e) (f)

Figure 3.13: Snapshots of the multi-phase plot of oil movement over the particle when Re=10, contact angle is 170 degree at time = (a) 0.00012, (b) 0.00142, (c) 0.00154, (d) 0.00158, (e) 0.00484 zoom-in, (f) 0.00484 zoom-out seconds

spills and the removal of pollutants on water surfaces [71].

3.1.3 The Bounce-back Phenomenon

As the simulations above show, the oil portion slides back to the particle after detaching when Re is 10 with the contact angle of 90°. This is caused by a sudden pressure drop between the particle and the oil film. Pressure is defined as force applied per unit area and is quantified in Newton per square meter or Pascal [73]. Once the oil portion detaches from the particle, the pressure map becomes unstable, but the pressure imbalance tends to become stable over time. However, the force promoting oil separation acts in the opposite way: the greater the hydrophobicity of the contact surface, the smaller the area of coverage will be, which leads to a larger force acting on the surface. By comparing the following two scenarios (contact angle of 90° and 170°), it can be clearly concluded that the larger the pressure difference between the particle and oil is, the larger tendency of oil separation.

We have generated a set of velocity vector diagrams by using a commercial software called "TEC360" (Tecplot, Inc.). The arrowhead indicates the direction of velocity and the length indicates the magnitude of velocity. In order to make the vectors clear and easy to recognize its direction, we have skipped 40-100 data points in different diagrams. It will not affect the analysis since we focus on changes instead of absolute values. At the initial stage of both cases in Figure 3.14a and 3.15a, the general inlet direction is from left to right with a constant magnitude. The velocities in the free stream that is above the oil film are much larger than the velocities inside the oil phase. It shows that oil lowers the velocity as it has large interfacial forces. As the inlet velocity is applied it pushes the oil film away from the particle. In Figure 3.14b,there is a circulation inside the oil phase. Such circulation provides a force that is strong enough to overcome the interfacial tension. Thus, the motion of moving away happens right after the circulation occurs. However, an interesting motion of bouncing back when Re of 10 with the contact angle at 90^o. In Figures 3.14e, 3.14f and 3.14g, the oil film moves back to the particle and stay in touch for the rest of this simulation. This is also caused by the velocity circulation inside the oil phase. In contrast, with Re of 10 at 170^o contact angle, once the oil moves away from the particle in Figure 3.15e, the oil does not move back to the particle because the velocities inside the oil are generally greater than the velocities in the water phase.

Overall speaking, the bounce-back phenomenon happens when the pressure between the particle and the oil film has suddenly dropped, as well as the velocity circulation inside the oil phase has pushed back oil to the particle. A complete

separation can only happen when the pressure drop is small compared to the shear force of the oil portion. There is no apparent oil movement when Re is 10 with the contact angle of 0^o. The velocity vector map visually explains the oil movement.

3.1.4 Investigating on the Critical Re with Different Contact Angle

The first completed separation simulation with the fine mesh is Re of 10 with the liquid-solid contact angle of 170°. Since there are two major factors influencing the separation process, namely, the Reynolds number and liquid-solid contact angle, the separation process is characterized with respect to a capillary number (ratio of viscous shear stress to interfacial tension) and the viscosity ratio (between the oil phase and the aqueous solution). Although remaining at the same viscosity ratio, only the Re and contact angle are considered in this problem. These simulations are all based on a finer mesh with control volume of 80,000 cells.

First of all, the larger the inlet velocity is, the greater the shear force would occur. When we increase the Re to 20 at the contact angle of 90°, a set of snapshots shown in Figure 3.16 suggests incomplete separation.

Same results from the simulation of Re of 50 at the contact angle of 90°, a set of snapshots shown in Figure 3.17 suggests incomplete separation.

As the results suggested in Figure 3.18, even though Re is reaching 100 (where the inlet velocity is 1m/s), there is no completed separation happening. The contact angle is remained the same of 90°.

The larger the inlet velocity is, the greater the shear force that will occur. When we increase the Re by applying greater inlet velocities, the following simulations are shown below. These simulations are all based on a finer mesh with a control volume of 80,000 cells is 1 m/s), there is no completed separation happening. The contact angle remains the same at 90°, which is caused by a strong interfacial tension. The external shear force is not sufficient enough to separate the oil droplet. It is important to lower the interfacial tension further to create full separation. It was mentioned in Fan et al. [66], that there is a critical Capillary number, $0.2<Ca<1$, where the interfacial tension force can no longer hold the oil drop together. The oil stretches into a long thread, and it is reasonable to assume that the thread will eventually rupture/separate [66].

Secondly, at a low Re/Ca, the shear force is not as noticeable as when the Re is large. The adhesion between the liquid and solid then plays a critical role. The contact angle distributes to the work of adhesion by the Young-Dupre equation [74].

$$\sigma(1 + \cos\theta) = \Delta W_s l \tag{3.1}$$

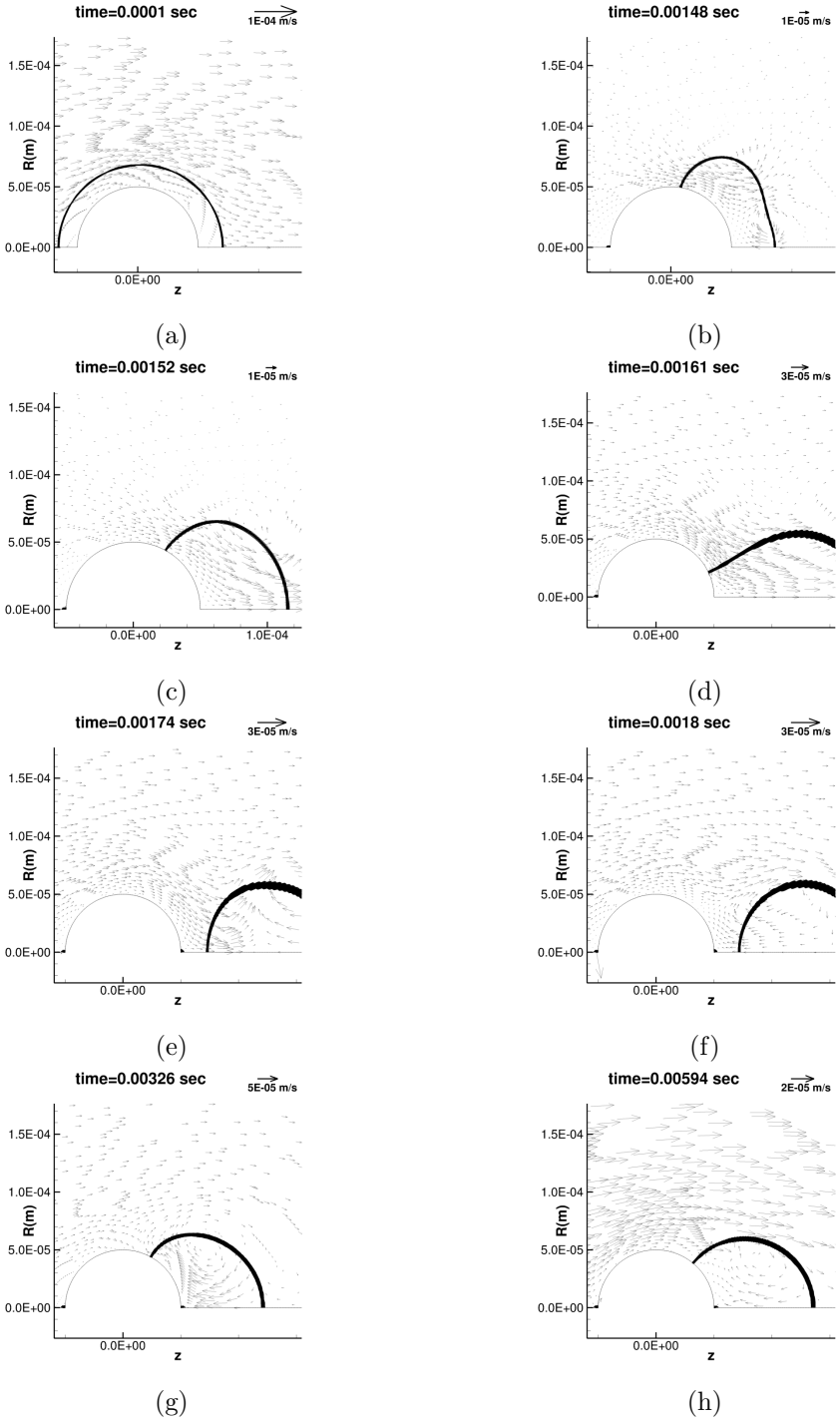

(a) (b) (c) (d) (e) (f) (g) (h)

Figure 3.14: Snapshots of the vector plot of velocity at time = (a) 0.0001, (b) 0.00148, (c) 0.00152, (d) 0.00161, (e) 0.00174, (f) 0.0018, (g) 0.00326, (h) 0.00594 seconds, predicted numerically when Re=10 at contact angle of 90 degree

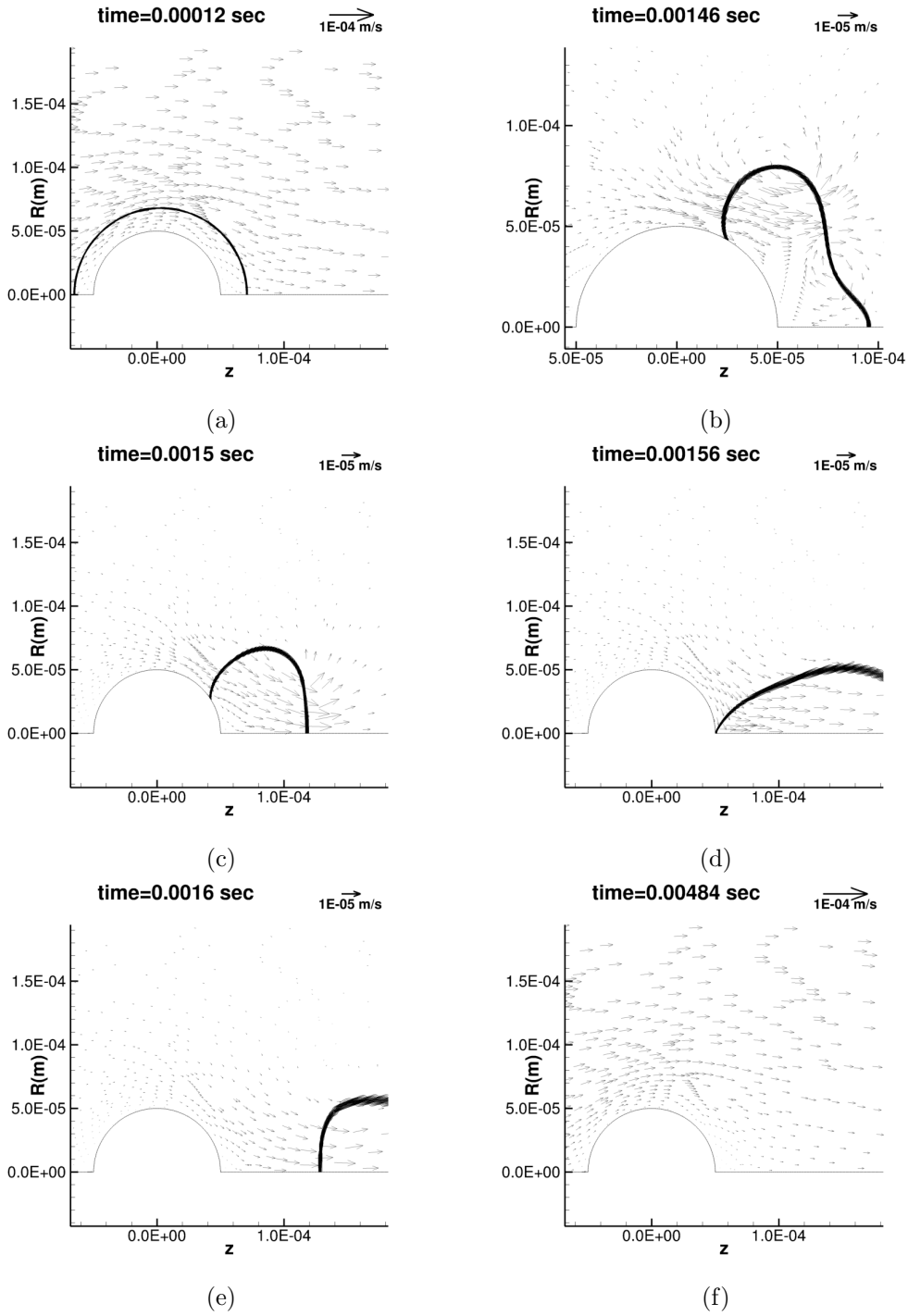

Figure 3.15: Snapshots of the vector plot of velocity at time = (a) 0.00012, (b) 0.00146, (c) 0.0015, (d) 0.00156, (e) 0.0016, (f) 0.00484 seconds, predicted numerically when Re=10 at contact angle of 170 degree

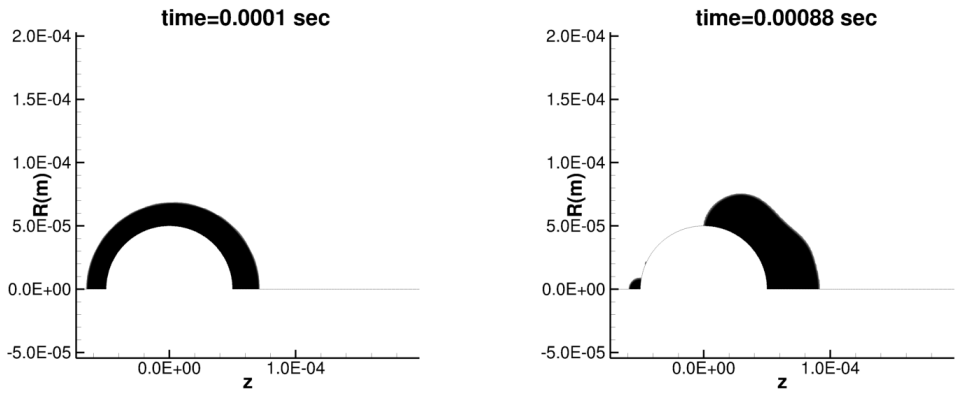

(a)

(b)

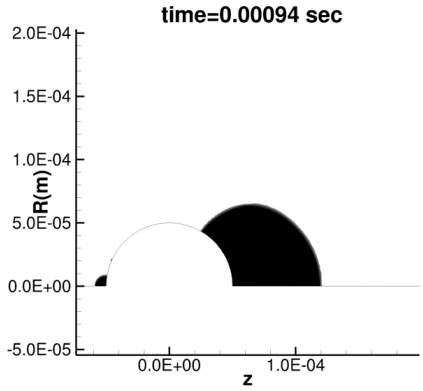

(c)

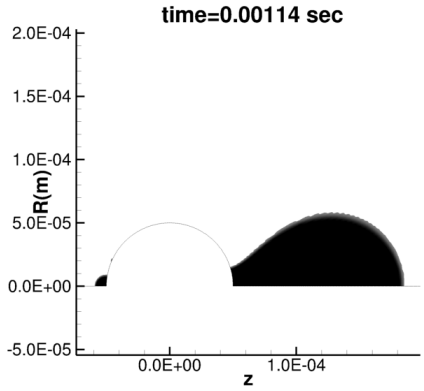

(d)

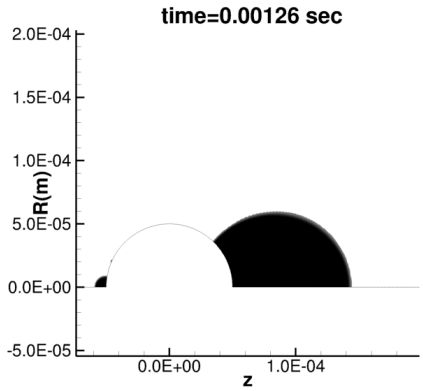

(e)

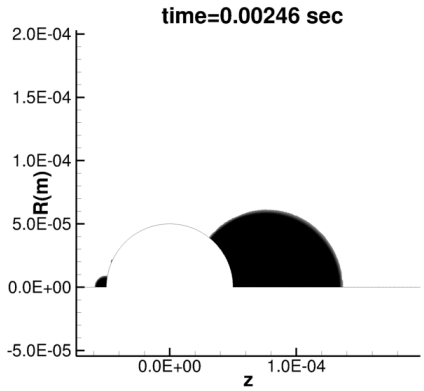

(f)

Figure 3.16: Snapshots of the multi-phase plot of oil movement over the particle when Re=20, contact angle is 90 degree at time = (a) 0.0001, (b) 0.00088, (c) 0.00094, (d) 0.00114, (e) 0.00126, (f) 0.00246 seconds

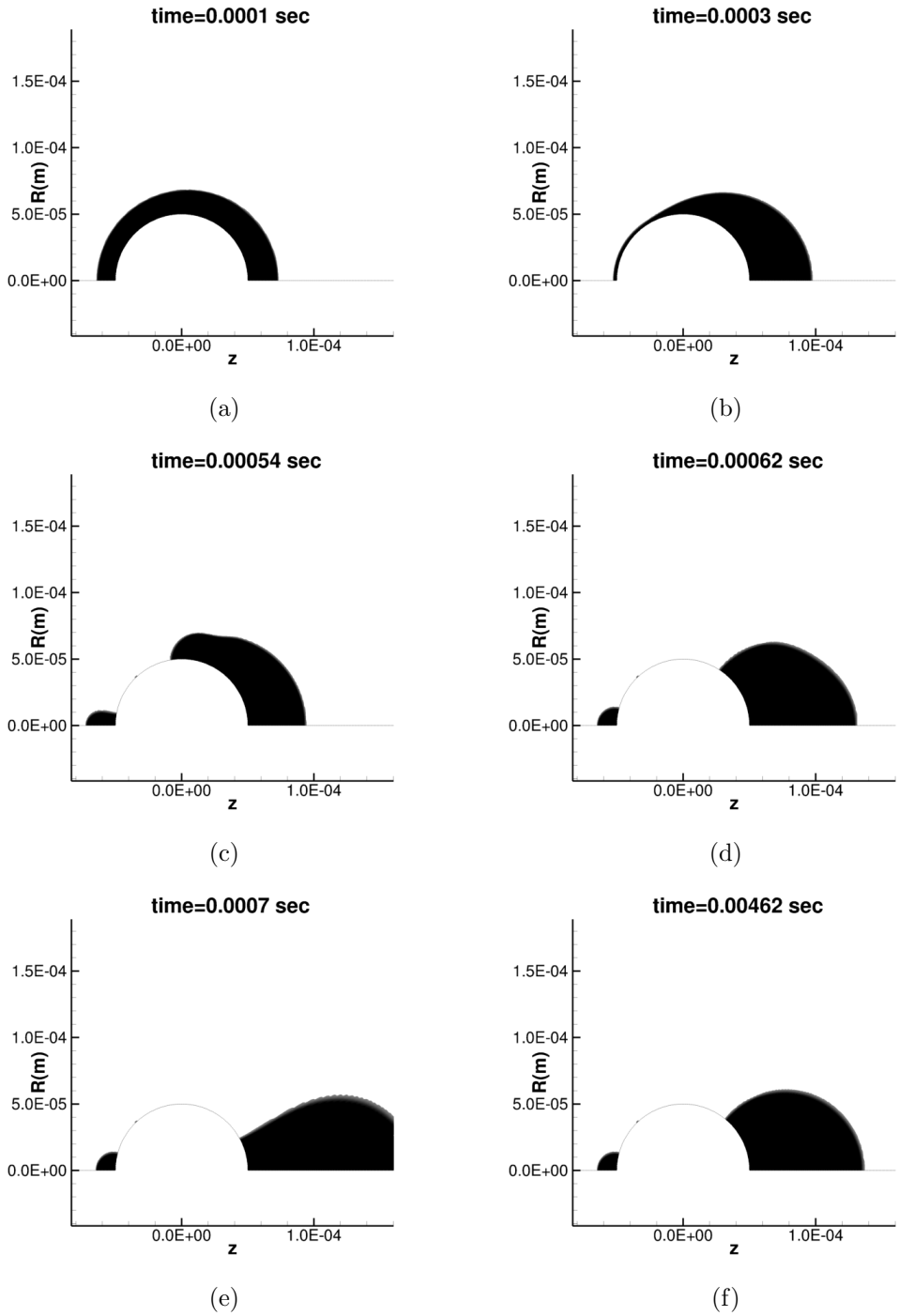

Figure 3.17: Snapshots of the multi-phase plot of oil movement over the particle when Re=50, contact angle is 90 degree at time = (a) 0.0001, (b) 0.0003, (c) 0.00054, (d) 0.00062, (e) 0.0007, (f) 0.00462 seconds

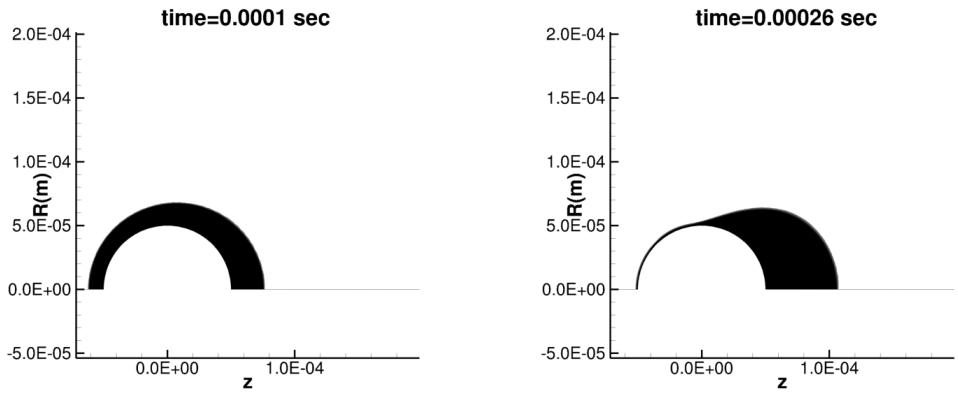

(a)

(b)

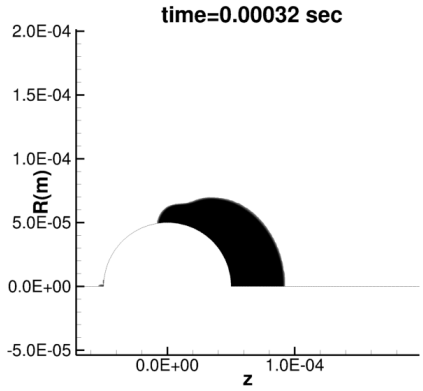

(c)

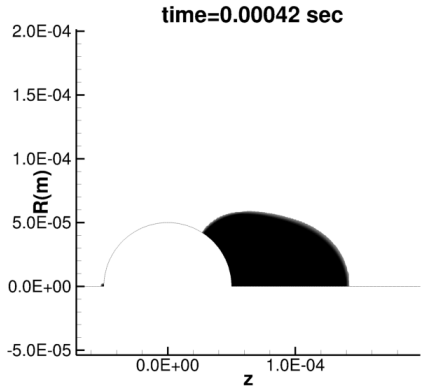

(d)

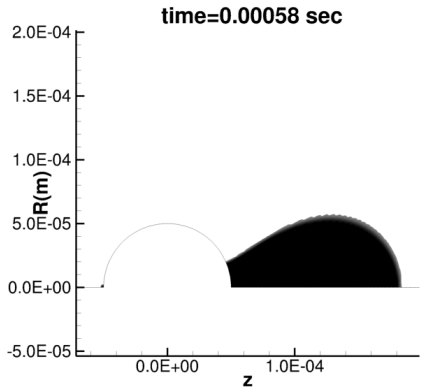

(e)

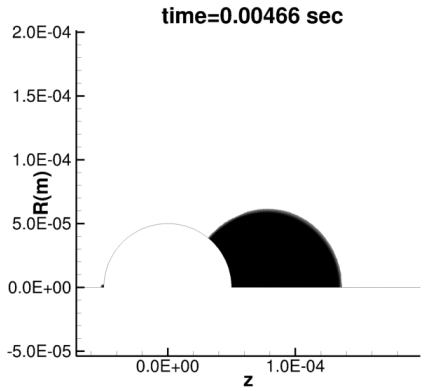

(f)

Figure 3.18: Snapshots of the multi-phase plot of oil movement over the particle when Re=100, contact angle is 90 degree at time = (a) 0.0001, (b) 0.00026, (c) 0.00032, (d) 0.00042, (e) 0.00058, (f) 0.00466 seconds

where σ is the interfacial tension which is assumed to be a constant; θ is the contact angle between the liquid and solid phases; $\Delta W_s l$ is the adhesion force in a medium (water in this work).

By plotting the contact angle with 0, 90, and 180 degrees, then the solid-liquid adhesion in the water phase results to 2σ, σ and 0. As the contact angle gets larger, the adhesion force between the solid and liquid gets smaller. It promotes a much easier separation/de-wetting process.

Last but not least, as the diameter becomes greater, a smaller curvature is formed. Meanwhile, there is a larger surface covered by liquid. Even though the shear force is still small, there will still be a larger area for the shear to be acted upon. In these simulations, we do not add any high-pressure devices, thus the pressure is the atmospheric pressure. There are gravitational effect and capillary effect [75]. As mentioned previously, gravity is ignored. Therefore, the capillary pressure dominates.

In conclusion, for each extreme case, there might be an optimal point. In order to find the range of each factor, the following plan table is made for future simulations.

Table 3.3: Inlet velocity with corresponding Ca and Re

	Diameter=100μm		Diameter=1000μm	
Re	V(m/s)	Ca	V(m/s)	Ca
1	0.01	1.39×10^{-4}	0.001	1.39×10^{-5}
2	0.02	2.78×10^{-4}	0.002	2.78×10^{-5}
3	0.03	4.17×10^{-4}	0.003	4.17×10^{-5}
5	0.05	6.94×10^{-4}	0.005	6.94×10^{-5}
7	0.07	9.72×10^{-4}	0.007	9.72×10^{-5}
10	0.1	1.39×10^{-3}	0.01	1.39×10^{-4}
20	0.2	2.78×10^{-3}	0.02	2.78×10^{-4}
50	0.5	6.94×10^{-3}	0.05	6.94×10^{-4}
100	1	1.39×10^{-2}	0.1	1.39×10^{-3}
150	1.5	2.08×10^{-2}	0.15	2.08×10^{-3}
200	2	2.78×10^{-2}	0.2	2.78×10^{-3}

We have performed Re values up to 200, because 2D modeling is not sufficient for any Re that is greater than 200. 3D modeling is not in this study's objective. The following Simulation Work Plan 3.4 aims to find each critical Re value when the contact angle is 0, 90 and 170 degrees.

There is no de-wetting happening when Re equals to 3 with the contact angle of 170^o, as seen in Figure 3.19. The complete separation happens when Re reaches 5, as well as Re of 7, shown in Figure 3.22. Thus, the critical Reynolds number is 5 (shown in Figure 3.21) when the contact angle is 170^o. Additionally, there is a

Table 3.4: Simulation work plan with separation status (xxx: not necessary to model)

Re	θ	D=100μm	D=1000μm	D=100μm oil fraction=0.75	D=100μm $\frac{\mu_{oil}}{\mu_{water}} = 10$
1	0	xxx	xxx		
	90	No movement	No movement		
	170				
3	0	xxx			
	90	Incomplete			
	170	Incomplete			
5	0	xxx		xxx	xxx
	90	xxx		xxx	xxx
	170	Complete		Complete	Incomplete
7	0	xxx			
	90	Incomplete			
	170	Complete			
10	0	No movement	xxx		
	90	Incomplete	Incomplete		
	170	Complete			
20	0	xxx	xxx		
	90	Incomplete	Incomplete		
	170				
50	0	xxx			
	90	Incomplete			
	170				
100	0	xxx			
	90	Incomplete			
	170	Complete			
150	0	xxx			
	90	Incomplete			
	170	Complete			
200	0	xxx			
	90	Complete			
	170	Complete			

zoom out view Figure 3.20 when Re is 5; when Re is 7, the zoom out view shown in Figure3.23. They both show that the oil portion is located far away from the particle at 0.01 seconds.

The following simulations aim to find the critical Re value with the contact angle of 90^o. The simulations are done with higher Re values. The snapshots of the simulation shown is Figures 3.24, when Re = 150 with a contact angle of 90^o.

The snapshots of the simulation shown is Figures 3.25, when Re = 200 with a

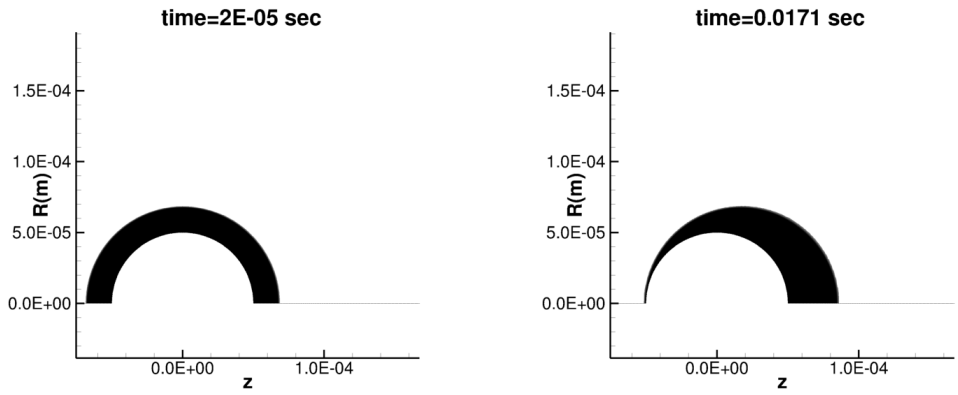

(a) (b)

Figure 3.19: Snapshots of the multi-phase plot of oil movement over the particle when Re=3, contact angle is 170 degree at time = (a) 0.00002, (b) 0.0171 seconds

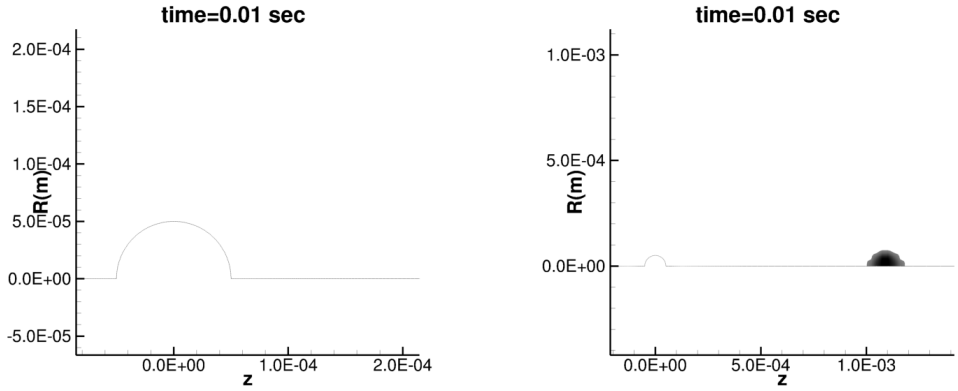

(a) (b)

Figure 3.20: Snapshots of the multi-phase plot of oil movement over the particle when Re=5, contact angle is 170 degree at time 0.01 seconds (a) Zoom in view, (b) Zoom out view

contact angle of 90^o. When Re reaches 200, eventually a compelte separation occurs.

To conclude, de-wetting starts to occur when the contact angle is 90°. However, the complete separation occurs once Re is reaching 200. Re of 200 is also the limit for 2D modeling in this area. It leads to the end for the simulation with 0° contact angle as well. Since there is no oil separated from the particle with Re of 200 at 0°, shown as Figure 3.26. There is no more trial can be done in this research.

Another modeling is to double the oil volume with Re of 5, shown in Figure 3.27 and 3.28. Therefore, the overall oil fraction becomes 0.75. It is the same as

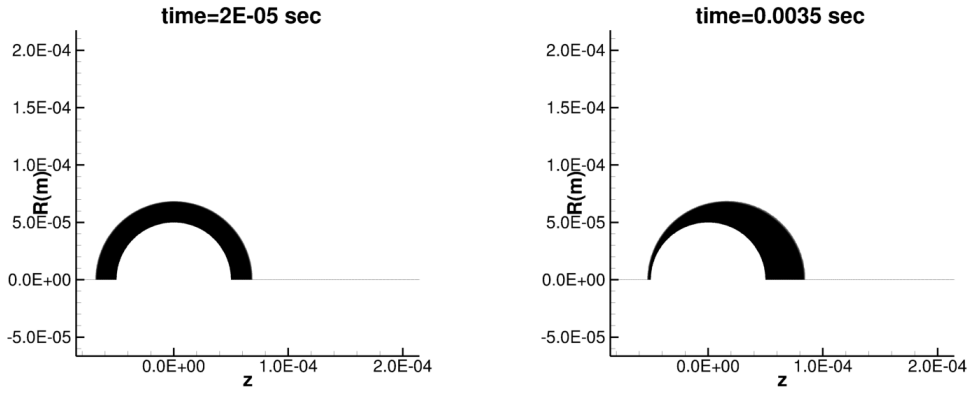

(a)

(b)

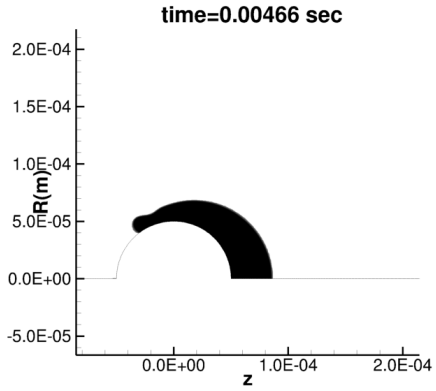

(c)

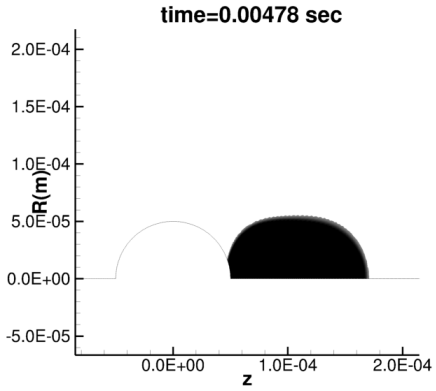

(d)

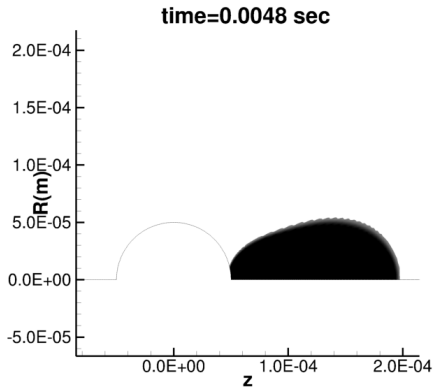

(e)

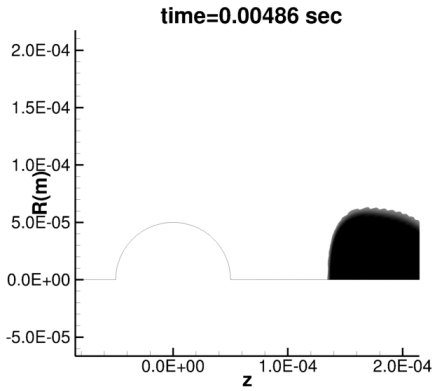

(f)

Figure 3.21: Snapshots of the multi-phase plot of oil movement over the particle when Re=5, contact angle is 170 degree at time = (a) 0.00002, (b) 0.0035, (c) 0.00466, (d) 0.00478, (e) 0.0048, (f) 0.00486 seconds

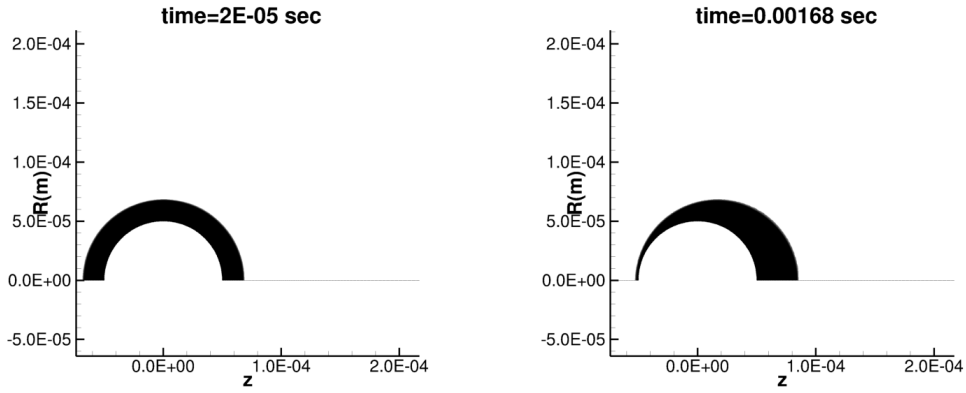

(a) (b)

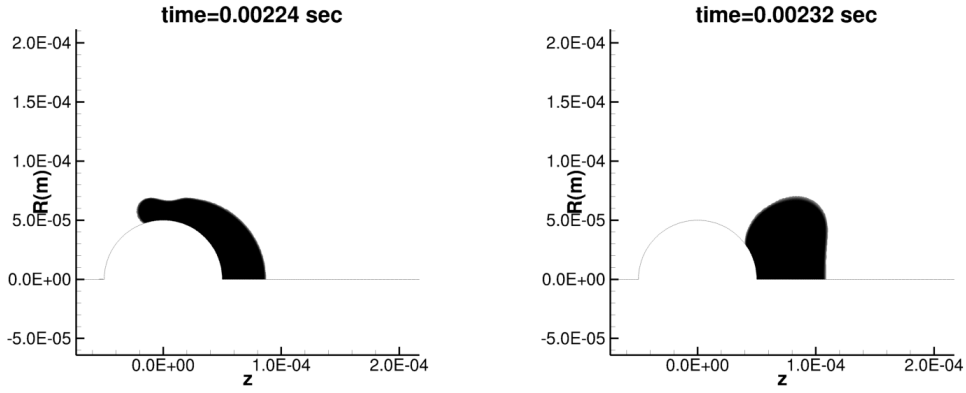

(c) (d)

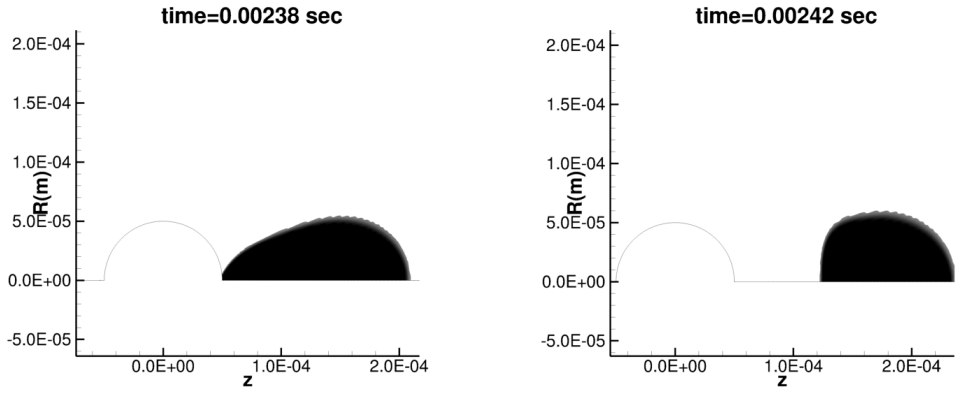

(e) (f)

Figure 3.22: Snapshots of the multi-phase plot of oil movement over the particle when Re=7, contact angle is 170 degree at time = (a) 0.00002, (b) 0.00168, (c) 0.00224, (d) 0.00232, (e) 0.00238, (f) 0.00242 seconds

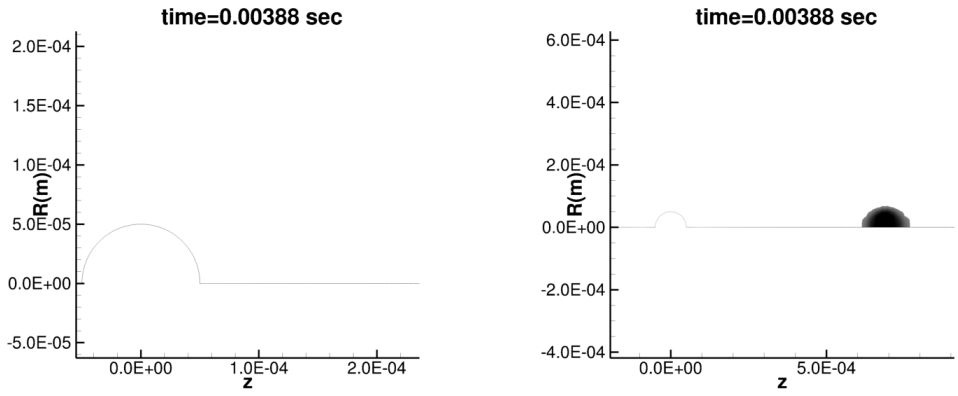

(a) (b)

Figure 3.23: Snapshots of the multi-phase plot of oil movement over the particle when Re=7, contact angle is 170 degree at time 0.00388 seconds (a) Zoom in view, (b) Zoom out view

double the oil thickness. This modeling was done to compare with the experiment by Bussmann et al. [2] in 2016. Bussmann et al. [2] has concluded that as the oil thickness becomes larger, the percentage of oil being separated is much more [2]. The simulation shows a complete separation that is faster than the original case. These results indicate an agreement with Bussmann et al. [2].

The last case with Re of 5 is to increase the oil viscosity to the ratio of 10, shown in Figure 3.29. The petroleum industry is starting to have an interest in untreated oil (no need to add solvent) separated from the particle. Thus, we modeled the oil with a much higher viscosity that is 10 times higher than water viscosity. It is surprising that the oil rarely moved during the simulation; in fact, it leads to no oil separation at all. It might be suggested that a solvent-treatment process [76] is essential for such an oil separation mechanism. Further simulation and deep investigation in this area will be required to achieve a more comprehensive conclusion.

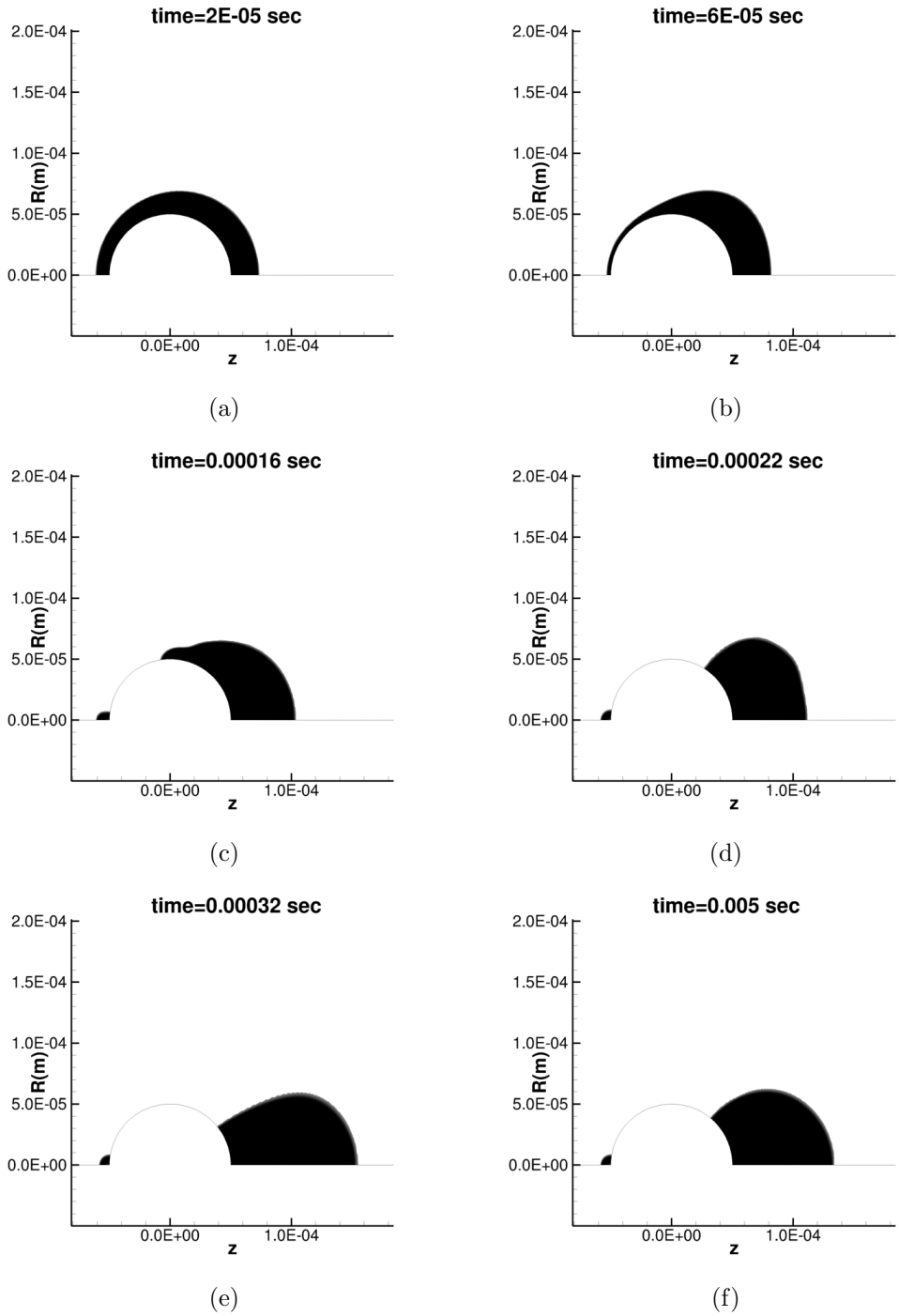

(a) (b) (c) (d) (e) (f)

Figure 3.24: Snapshots of the multi-phase plot of oil movement over the particle when Re=150, contact angle is 90 degree at time = (a) 0.00002, (b) 0.0006, (c) 0.00016, (d) 0.00022, (e) 0.00032, (f) 0.005 seconds

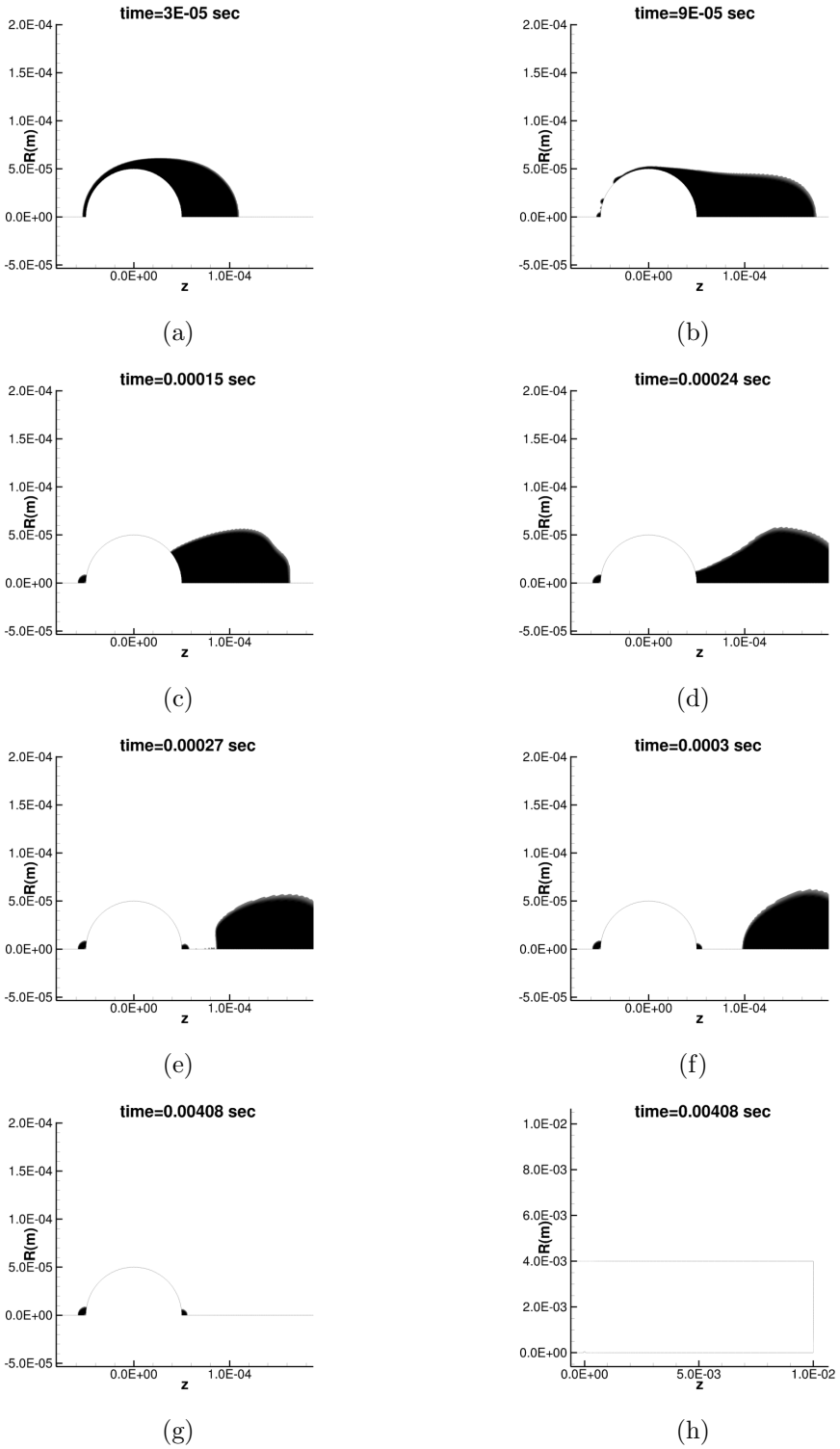

(a) (b) (c) (d) (e) (f) (g) (h)

Figure 3.25: Snapshots of the multi-phase plot of oil movement over the particle when Re=200, contact angle is 90 degree at time = (a) 0.00003, (b) 0.00009, (c) 0.00015, (d) 0.00024, (e) 0.00027, (f) 0.0003,(g) 0.00408 zoom-in, (h) 0.00408 zoom-out seconds

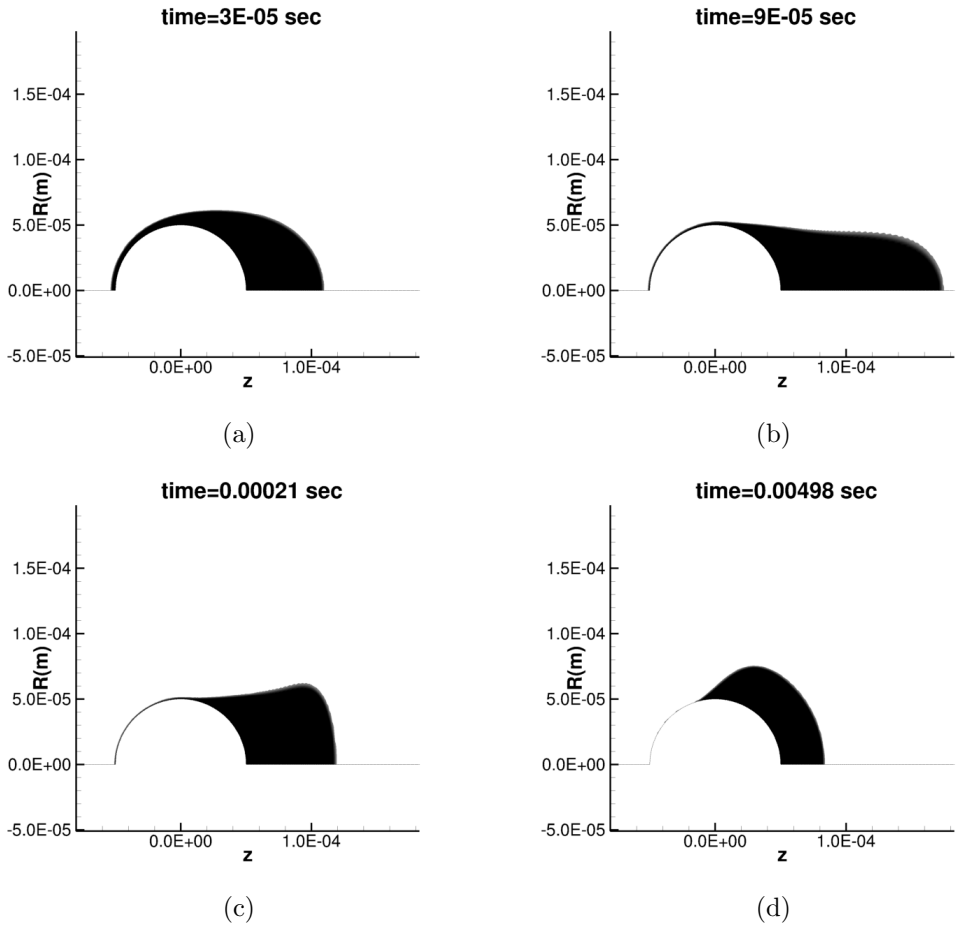

(a) (b)

(c) (d)

Figure 3.26: Snapshots of the multi-phase plot of oil movement over the particle when Re=200, contact angle is 0 degree at time = (a) 0.00003, (b) 0.00009, (c) 0.00021, (d) 0.00498 seconds

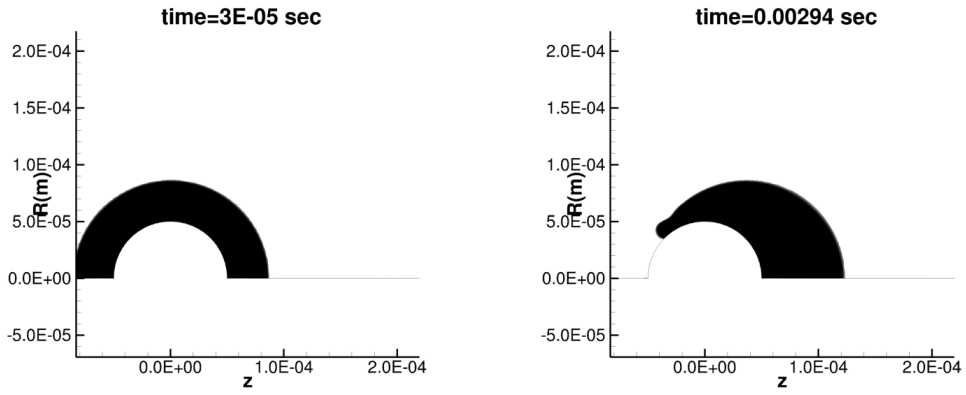

(a)

(b)

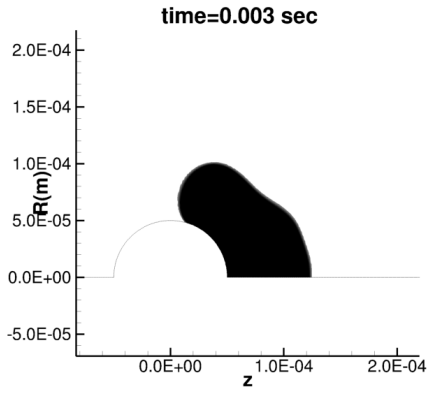

(c)

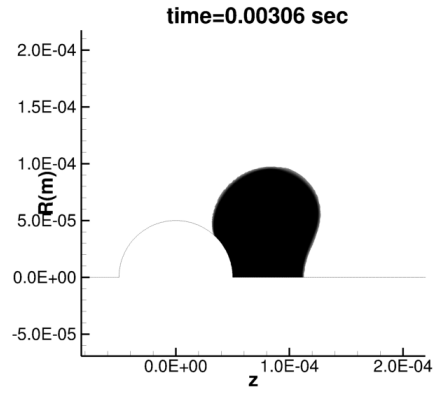

(d)

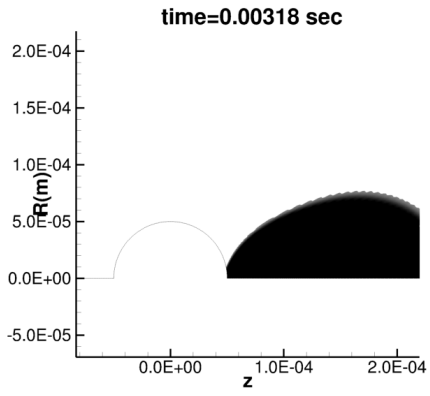

(e)

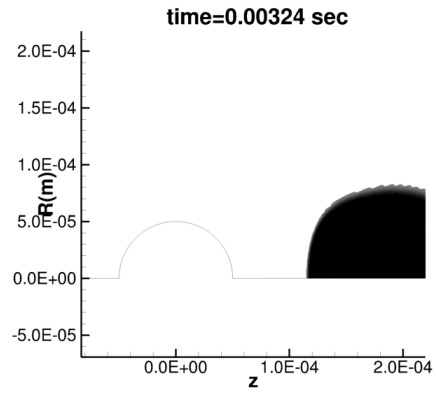

(f)

Figure 3.27: Snapshots of the multi-phase plot of oil movement over the particle when Re=5, contact angle is 170 degree with doubled oil film thickness at time = (a) 0.00003, (b) 0.00294, (c) 0.003, (d) 0.00306, (e) 0.00318, (f) 0.00324 seconds

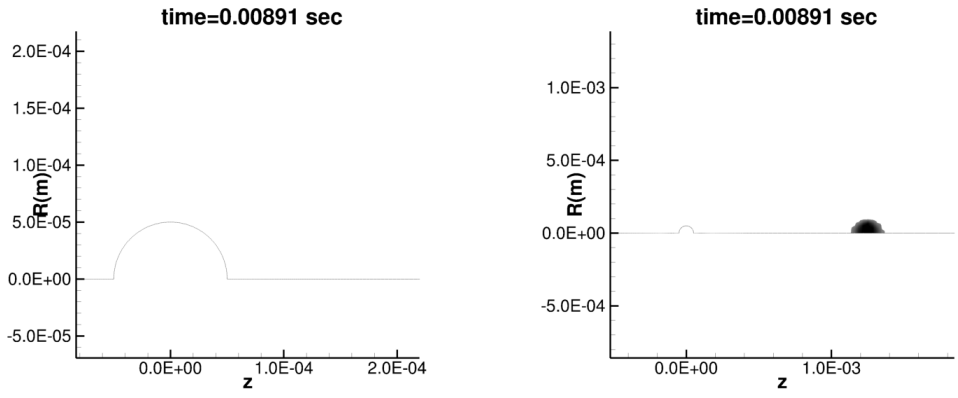

(a) (b)

Figure 3.28: Snapshots of the multi-phase plot of oil movement over the particle when Re=5, contact angle is 170 degree with doubled oil film thickness at time 0.00891 seconds (a) Zoom in view, (b) Zoom out view

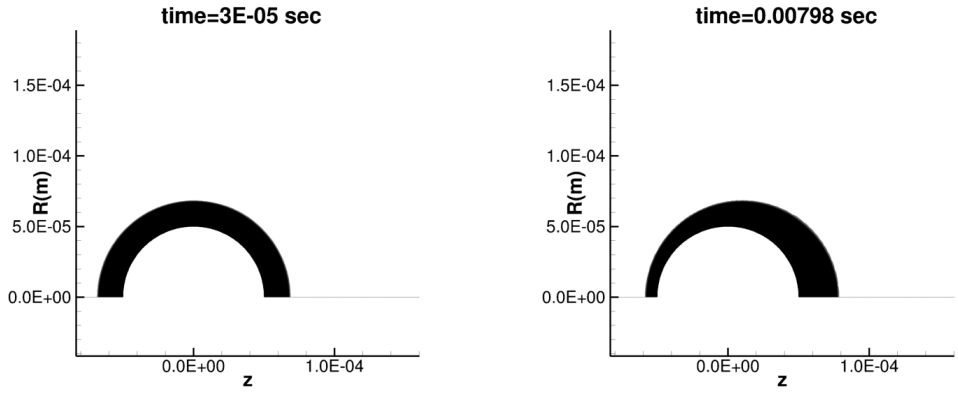

(a) (b)

Figure 3.29: Snapshots of the multi-phase plot of oil movement over the particle when Re=5, contact angle is 170 degree with the oil phase viscosity 10 times higher than water phase viscosity at time = (a) 0.00003, (b) 0.00798 seconds

3.2 Investigating on the Volume Average Velocity of Separation

ANSYS FLUENT [1] can generate a "vol-mon" file in each simulation. Data provided can plot into the following graphs. The peak point in each graph is where the oil gets separated from the particle. We have selected all cases that have complete separations, Re of 5 in Graph 3.30; Re of 7 in Graph 3.31; Re of 100 in Graph 3.32; Re of 200 in Graph 3.33.

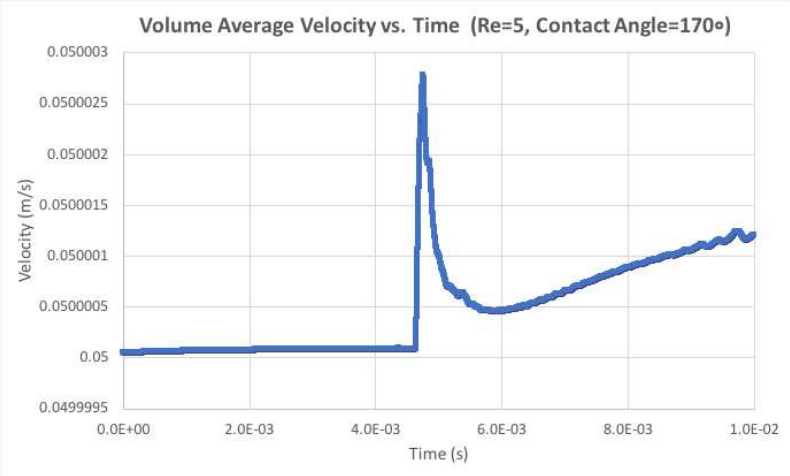

Figure 3.30: Volume average velocity verse time of Re=5

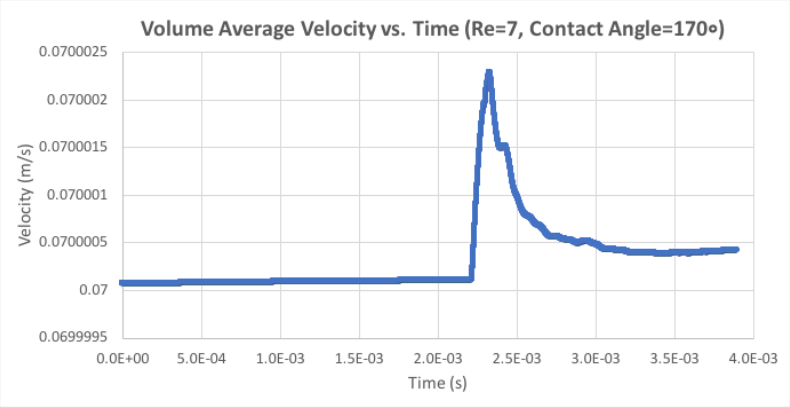

Figure 3.31: Volume average velocity verse time of Re=7

After manipulating all comparable cases, we observe an interesting trend of volume average velocity vs. time. The first step is to create a dimensionless index which involves Re as a factor. The procedure to calculate the dimensionless velocity index is done by using the actual velocity magnitude to divide its corresponding

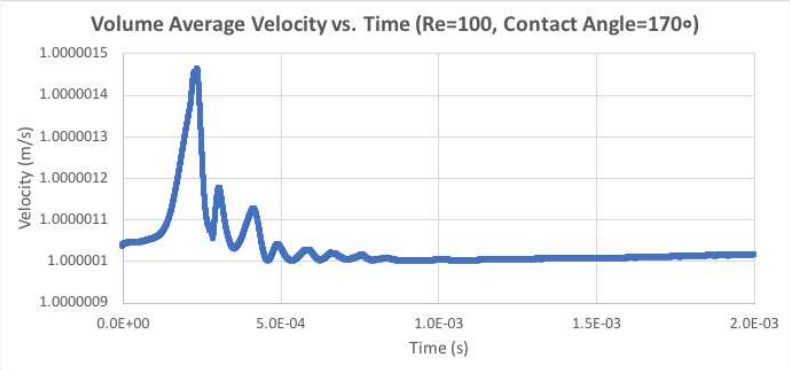

Figure 3.32: Volume average velocity verse time of Re=100

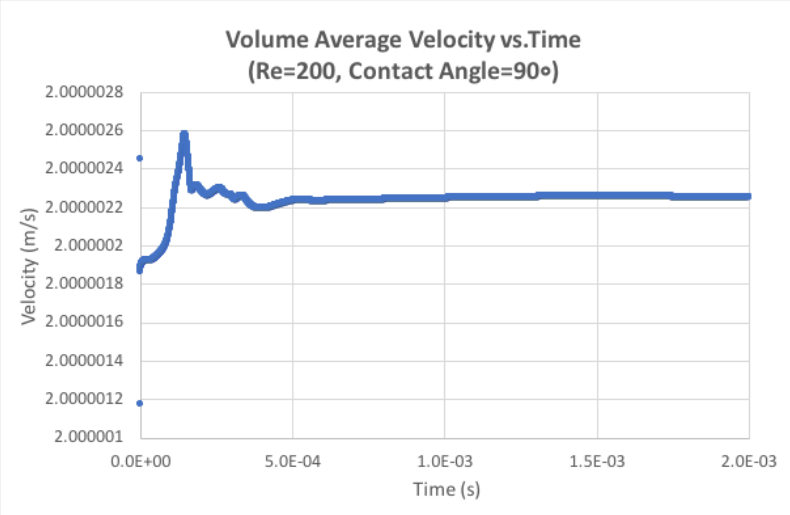

Figure 3.33: Volume average velocity verse time of Re=200

inlet velocity. For example, when Re is 5, the inlet velocity is 0.05 m/s, as shown in Table 3.3. And while its separation time is 0.00480 s, the real-time velocity is 0.0500028 m/s. Thus, its dimensionless velocity index equals to 1.00056. The second step is to plot the index versus its separation time. The third step is to collect as many data points as possible into one graph. The last step is to summarize if there is a certain trend or outstanding features. The trend is shown in Figure 3.34.

In order to verify if this trend indeed applies to other Reynolds numbers, we must find the point of Re of 10 at the contact angle of 170°. From the predictive trend in Graph 3.34, he separation time is approximately 0.00157s. The corresponding dimensionless velocity index is approximately 1.000022. Again, by multiplying 1.000022 by 0.1 m/s (inlet velocity), it gives 0.1000022 m/s as the volume average velocity at the time of 0.00157 s. By using a commercial software "TEC360" (Tec-

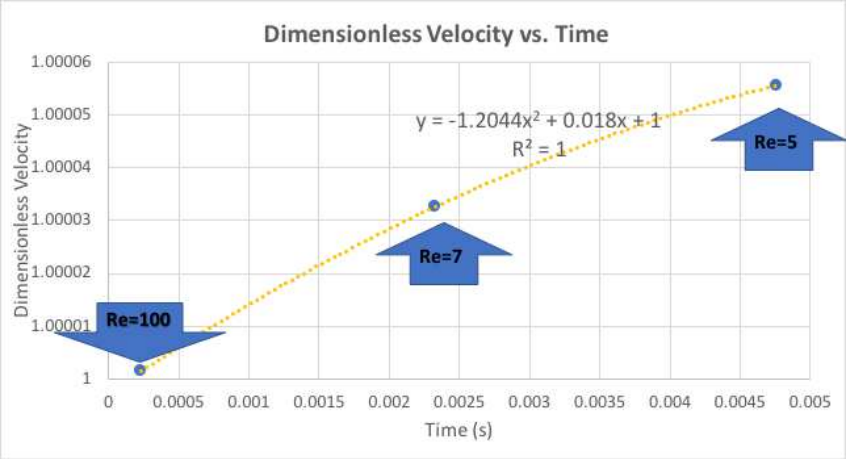

Figure 3.34: Dimensionless velocity verse separation time

plot, Inc.) to generate a velocity diagram, it is shown a velocity where the oil is just about separated from the particle at the time of 0.00156 s. The real-time velocity is between 0.09 m/s and 0.105 m/s which corresponds with the trend in Graph 3.34.

3.3 Results

The separation of oil from a single oil-coated spherical particle immersed in water is evaluated as a function of viscosity ratio and interfacial tension [30]. A physical model for a single particle separation process from oil is presented. The mechanism of this model is to apply a constant inlet velocity in order to achieve complete separation. The model is applied to the VOF approach and coded by commercial ANSYS Fluent [1]. We selected VOF as a modeling technique and SIMPLE scheme and QUICK momentum as a solution method while running up to 200,000 iterations with a time step of 1 μs. Lastly, we monitored the movement of oil portion.

In this study, we address the differences in the particle-oil separation mechanisms and characterize the similarities and differences in the changing Reynolds number and contact angles within the same surrounding environments. Based on the simulations above, it is clear enough to conclude that oil-particle interactions greatly depend on the inlet velocity and oil-particle contact angle. Firstly, at the low inlet velocity (Re=1), because of inadequate shear force, the oil film does not move away from the particle. De-wetting occurs when inlet velocity reaches 0.02 m/s (Re=2). However, the complete separation happens only when Re is approximately 10. Thus, we conclude there is a critical Re in each case. Secondly, within a finer mesh, the separation process is more sensitive to the changing contact angle. In this case, the

higher the hydrophobicity of the contact surface, the less wettability the solid by the liquid is, which leads to an easier separation.

There is complete separation at Re of 5 with the 170° contact angle. With the contact angle of 90°, complete separation only happens once the Re value reaches 200. As Re becomes greater, the separation happens faster. However, due to accessibility, 2D-modeling can only be applied up to Re of 200. Within this range, there is no separation when the contact angle is at 0°. The greater the oil fraction is, the easier the separation.

3.4 Porous Particle Modeling

3.4.1 2D Modeling for Porous Particle

In reality, there is not always a perfect spherical solid particle. Many naturally occurring sands or mud are permeable and porous [77]. In this chapter, we start the modeling of a 'saw-tooth' shaped spherical solid particle that is covered by a thin oil film while immersed in water. While remaining the 2D modeling, a rough particle is used to present the porous particle. It is also a two-dimensional multiphase case. Identical to the modeling in the previous chapter, the size of this two-dimensional computational domain is 0.01 m by 0.004 m as shown in Figure 3.35. In order to compare both particles, where the diameter of the solid particle is remained to be 100 μm with the oil thickness of 17.8μm.

Since the particle is not smooth, the overall volume is 1% less than the previous case. The rough particle is shown in Figure 3.35. It leads to a slightly higher oil fraction (0.61) than the previous case (0.6). A fine mesh with an 80,000-control volume is used. The initial temperature of the water is 288.16 K (15°C) and to be constant going forward. The top and the bottom boundaries apply symmetrical boundary conditions and the left boundary applies velocity inlet conditions, respectively.

Again, we proceed with the same water and oil properties that we used in Chapter 3. The water properties have non-linear dependencies on the temperature, which are not to be taken into account in the modeling because we have a constant temperature in this case. At the same time, we will keep the same assumptions that water and oil have the same density ($1000 kg/m^3$) and viscosity (1 mPa·s) as well as the assumption of a constant interfacial tension of 72 mN/m between oil and water.

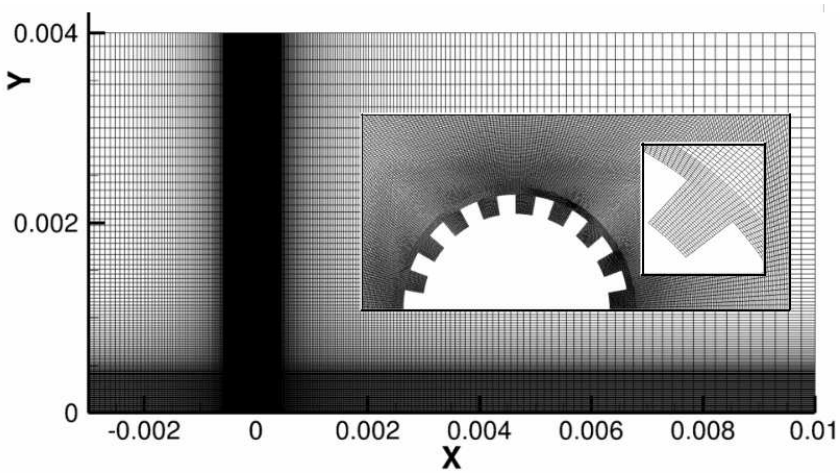

Figure 3.35: Numerical two-dimensional and axisymmetric mesh of rough particle; X responding to Z axis and Y responding to R (radius); both in meters

3.4.2 Changing Reynolds Number and Contact Angles

From the results for the smooth particle, the critical Re with a contact angle of 170^o is 5; meanwhile, the critical Re value with a contact angle of 90° is 200. For the purpose of this study, if the critical Reynolds number is applied to differently shaped particles (solid particle and porous particle), the same critical Re values have been used for the simulations. Aa a first step, there are four simulations on rough particle has been performed. They are cases that (1) Re = 5 at 170^o contact angle, shown in Figure 3.36; (2) Re = 200 at 0^o contact angle, shown in Figure 3.37; (3) Re = 200 at 90^o contact angle, shown in Figure 3.38; (4) Re = 200 at 170^o contact angle, shown in Figure 3.39.

As the simulations shown above, there is no separation happening among all cases. Those pores inside the particle catch oil as the inlet velocity applies. By comparing the Re of 5 and 200 at the 170^o contact angle, it indicates that the higher the inlet velocity is, the more oil would be trapped into the pores. At the same Re value of 200, oil movement at the different contact angles (0^o and 90^o) does not show a distinguishable difference.

3.4.3 Velocity Vector Analysis

Similar to the solid particle, a set of velocity vector changing study is discussed in this section. The velocities in the free stream are generally greater than the pressures in the oil phase. This continuous velocity supply moves the oil away from the particle. Once the velocity circulation forms inside the oil phase, it competes

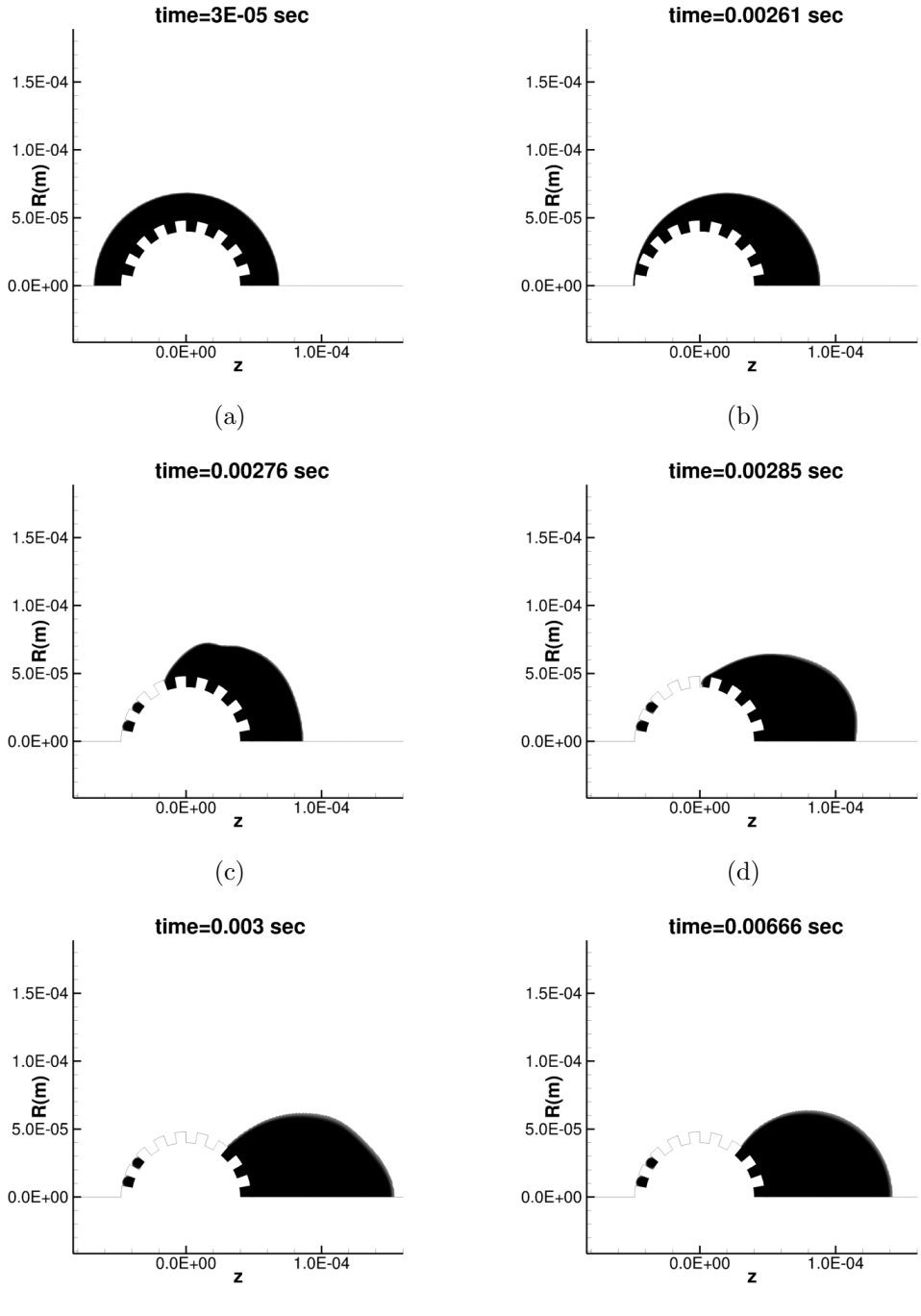

(a) (b) (c) (d) (e) (f)

Figure 3.36: Snapshots of the multi-phase plot of oil movement over the particle when Re=5, contact angle is 170 degree of a porous particle at time = (a) 0.00003, (b) 0.00261, (c) 0.00276, (d) 0.00285, (e) 0.003, (f) 0.00666 seconds

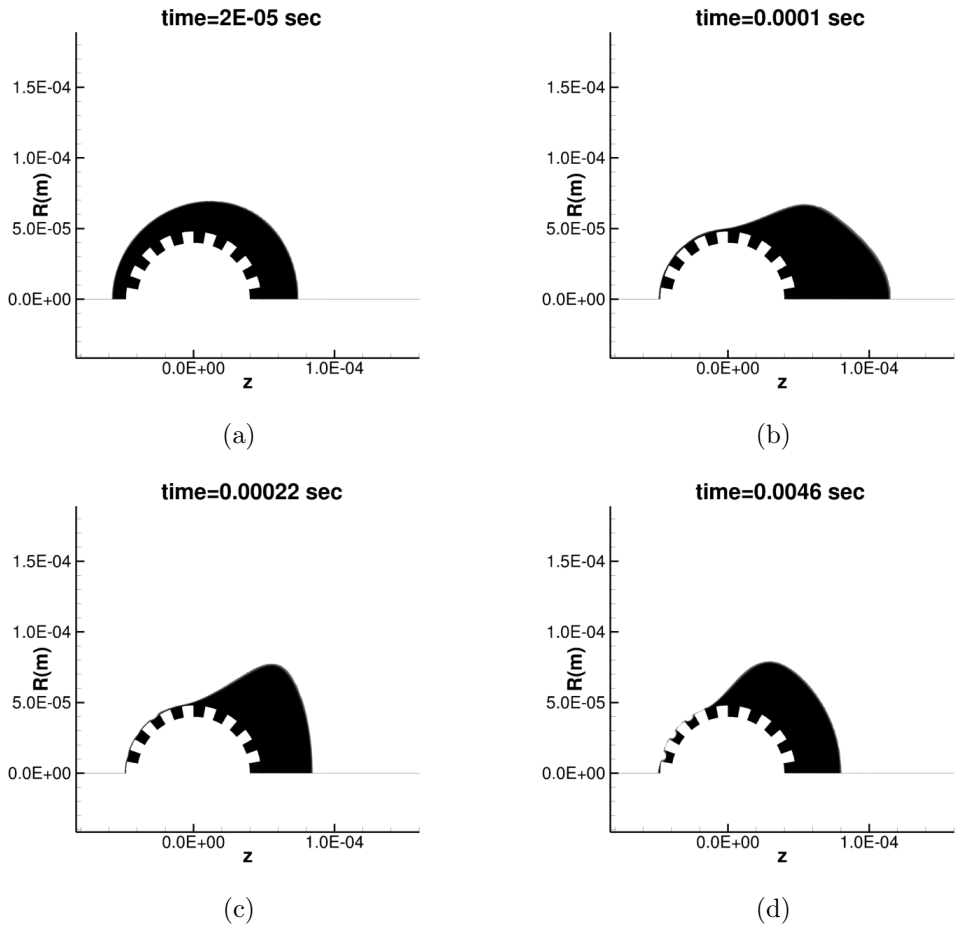

Figure 3.37: Snapshots of the multi-phase plot of oil movement over the particle when Re=200, contact angle is 0 degree of a porous particle at time = (a) 0.00002, (b) 0.0001, (c) 0.00022, (d) 0.0046 seconds

with the interfacial tension between the oil and particle. In conclusion, there is no oil separation for all four cases. By comparing Figure 3.41, 3.42 and 3.43, as the contact angle becomes greater, the circulation also becomes greater in terms of area, indicating an easier moving motion. In the final diagram of Figure 3.40, there are some outstanding high-velocity vectors at the edge of the oil film. These vectors suggest a longer simulation period needed to reach an equilibrium status. Apparently, Re of 5 requires much longer to be settled than Re of 200.

When the contact angles are 0^o and 90^o, the oil portion tends to being stick together through the whole observation period. By contrast, when the contact angle is 170^o, the larger oil portion still has enough energy to move further away from the particle. We might expect some oil separation with an even larger inlet velocity. It

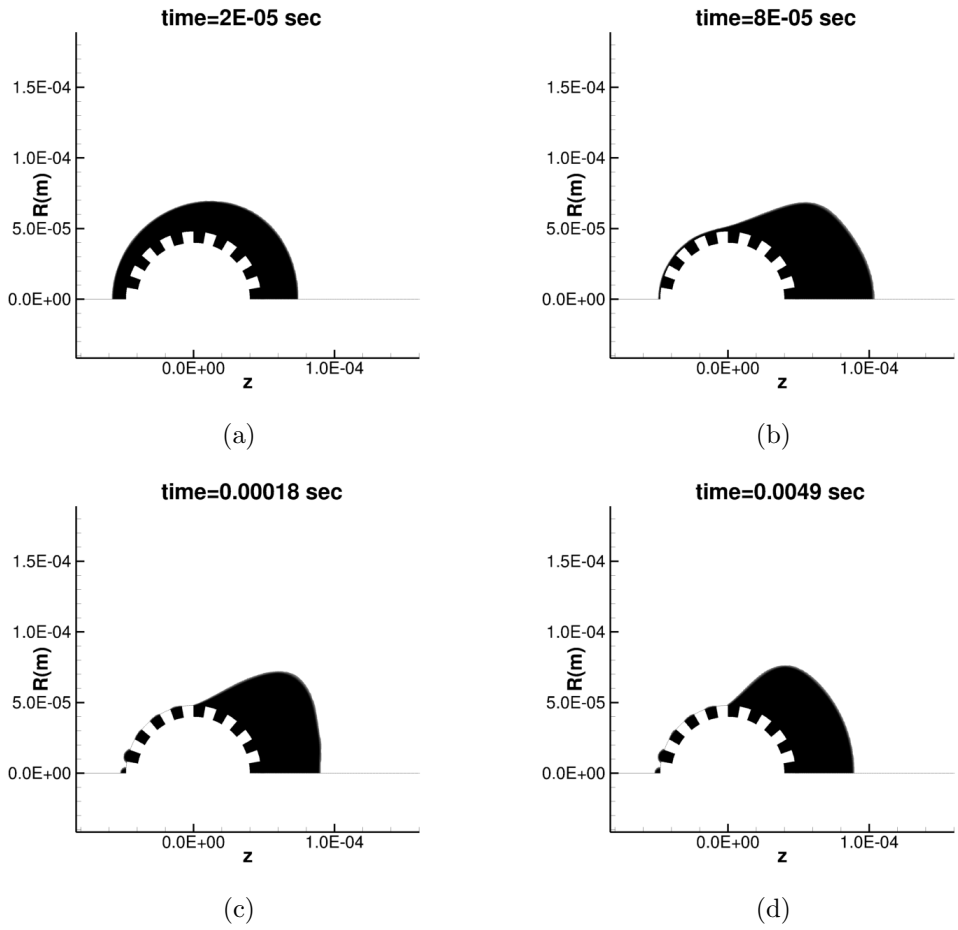

Figure 3.38: Snapshots of the multi-phase plot of oil movement over the particle when Re=200, contact angle is 90 degree of a porous particle at time = (a) 0.00002, (b) 0.00008, (c) 0.00018, (d) 0.0049 seconds

confirms the same idea as in the last section, that the greater the hydrophobicity of the contact surface, the smaller the area of coverage. Thus, it leads to a larger force acting to the surface.

3.4.4 Results

By comparing these four scenarios (contact angle of 0^o, 90^o, and 170^o at Re of 5 and 200), it is clear to conclude that the porous particles are more difficult than smooth particles for oil separation. The pressure difference between the particle and oil shows the tendency of oil separation would be larger. There is no oil separation among the four cases in this modeling. As the pores trap oil inside, the remaining oil portion would move alone when the contact angle is at 170^o. In other words,

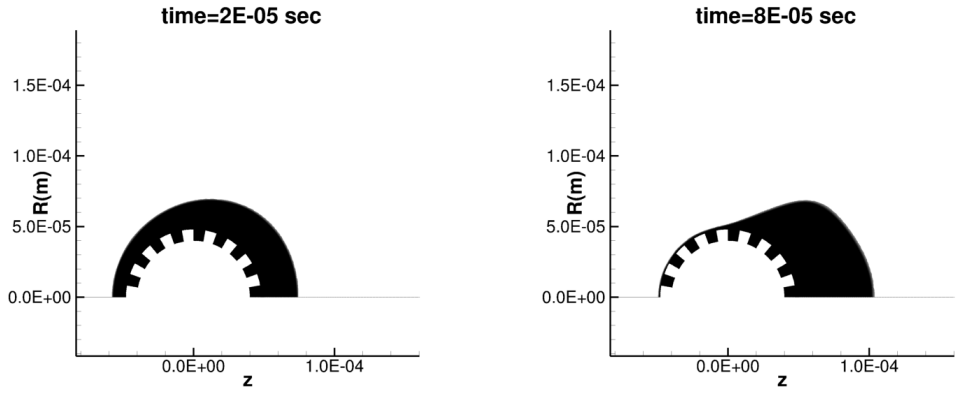

(a)

(b)

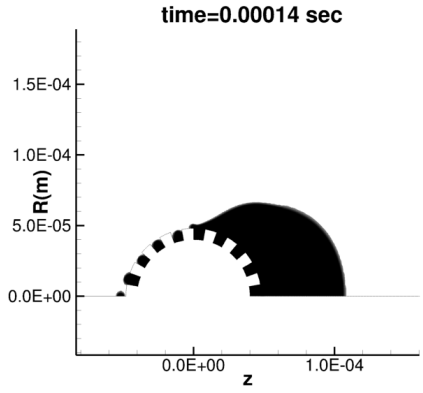

(c)

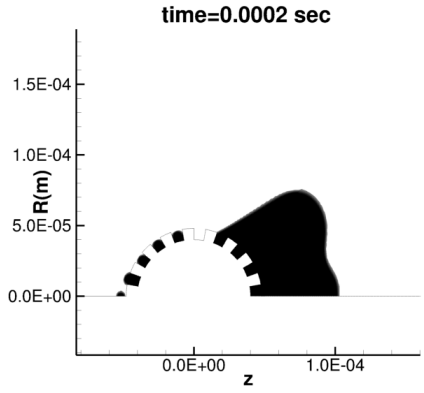

(d)

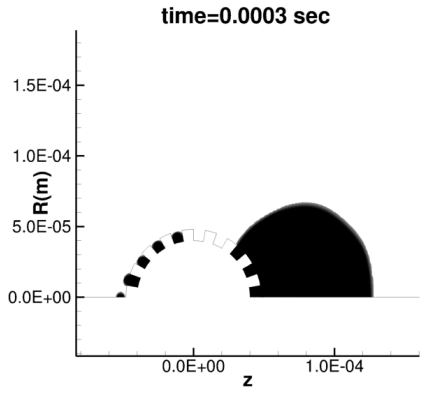

(e)

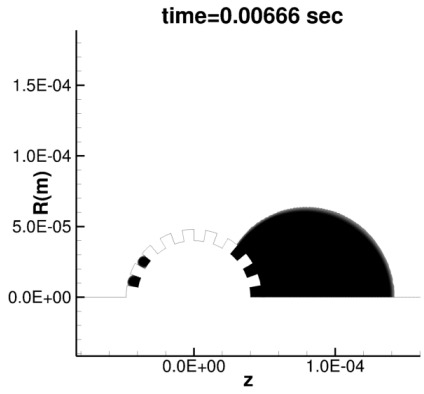

(f)

Figure 3.39: Snapshots of the multi-phase plot of oil movement over the particle when Re=200, contact angle is 170 degree of a porous particle at time = (a) 0.00002, (b) 0.00008, (c) 0.00014, (d) 0.0002, (e) 0.0003, (f) 0.00666 seconds

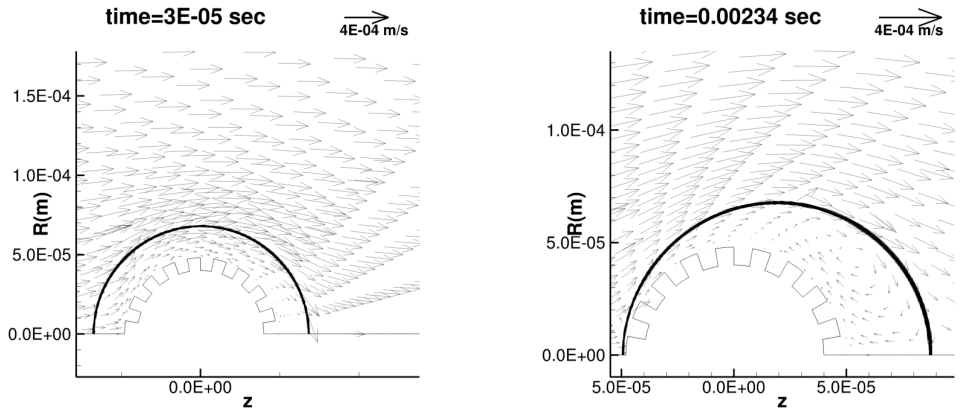

(a)

(b)

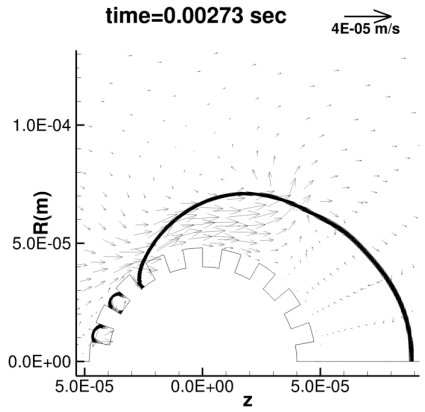

(c)

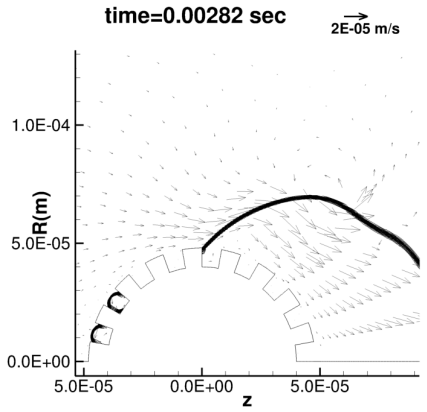

(d)

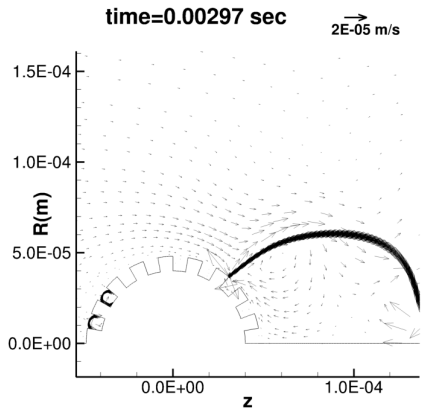

(e)

Figure 3.40: Snapshots of the vector plot of velocity at time = (a) 0.00003, (b) 0.00273, (c) 0.00282, (d) 0.00303, (e) 0.00666, predicted numerically when Re=5 at contact angle of 170 degree

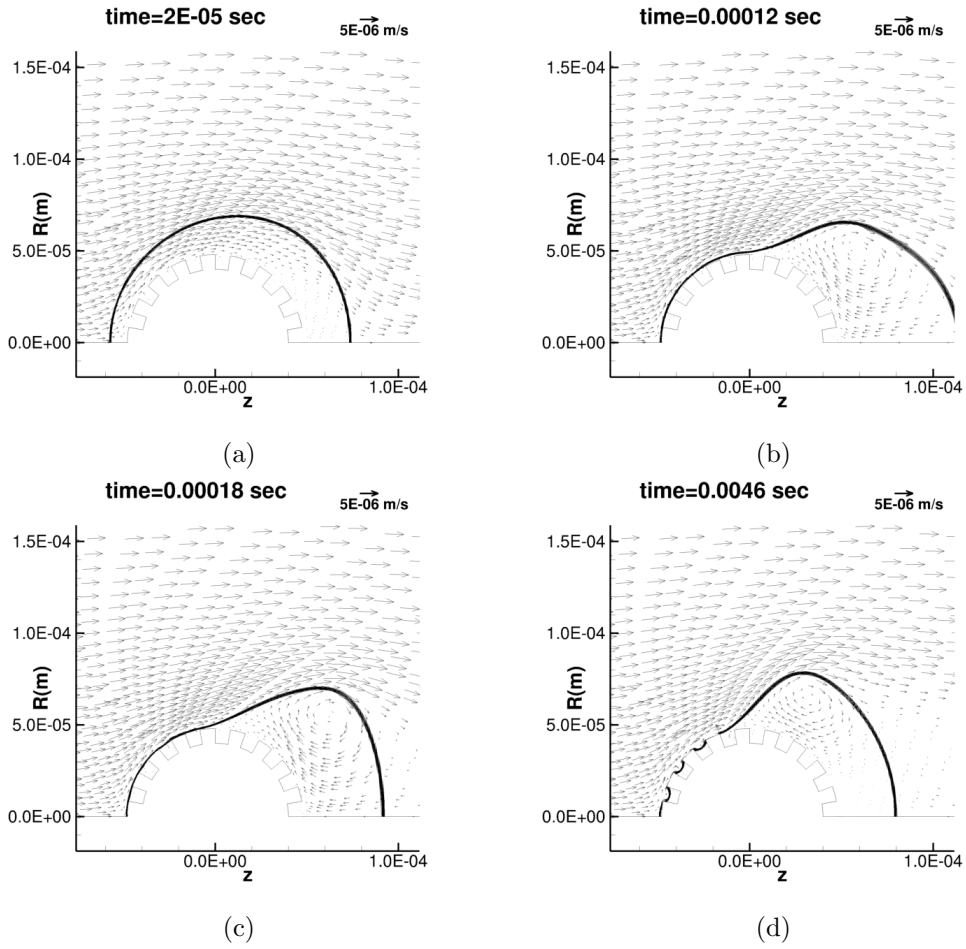

Figure 3.41: Snapshots of the vector plot of velocity at time = (a) 0.00002, (b) 0.00012, (c) 0.00018, (d) 0.0046, predicted numerically when Re=200 at contact angle of 0 degree

although we expect some oil separation with larger Re values, not all oil will be separated in the process. It does not show a tendency for a complete oil separation.

3.5 Conclusions

In summary, as the inlet velocities apply to the oil film increasing, the oil separation process gets easier and faster, except in the case of a 0° contact angle. In the investigation of effect in hydrophobicity, the higher the hydrophobicity, the easier the oil separation process, while holding the same Reynolds number. There is a critical Reynolds number for each modeling case. Due to the limitation of 2D-modeling, all cases above Re of 200 are not able to be performed in this study. Moreover, the

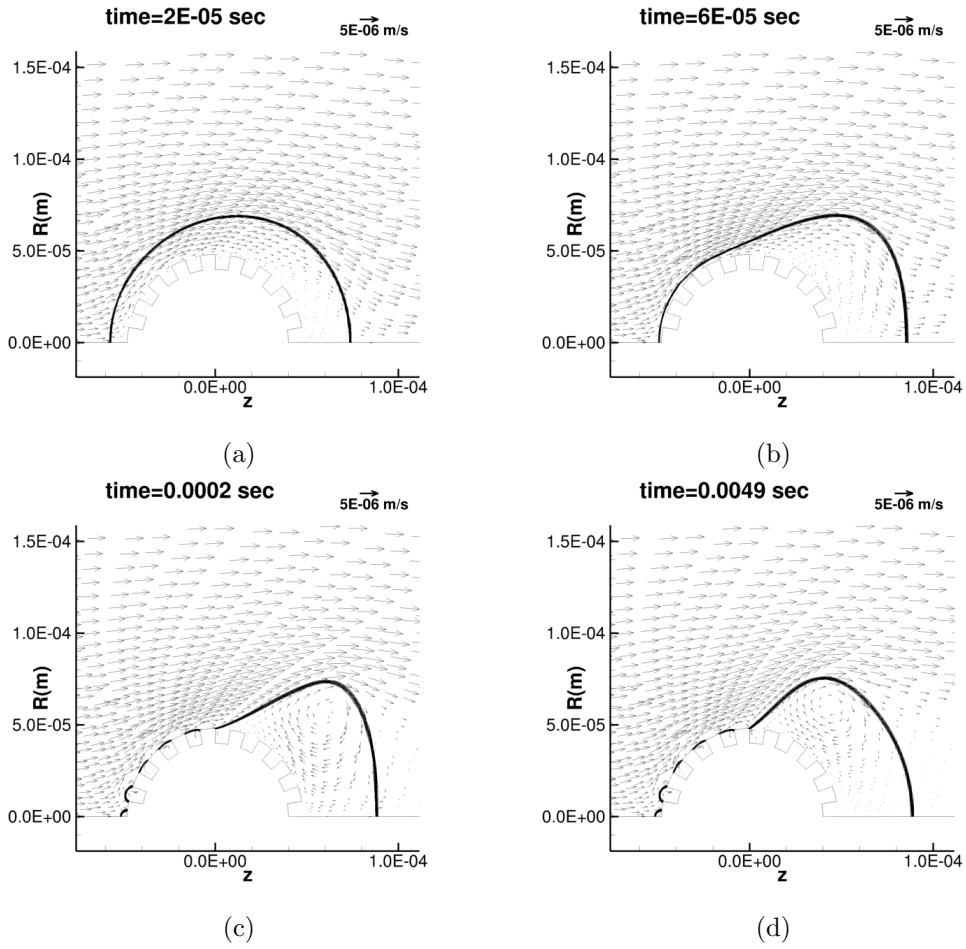

Figure 3.42: Snapshots of the vector plot of velocity at time = (a) 0.00002, (b) 0.00006, (c) 0.0002, (d) 0.0049, predicted numerically when Re=200 at contact angle of 90 degree

bounce-back phenomenon is observed when Re is 10 with a 90° contact angle. This phenomenon has previously not been described in other literature. Additionally, a porous particle is also modeled and analyzed. However, the porous particles are more difficult than smooth particles during the oil separation process. There is no oil separation being observed in this study.

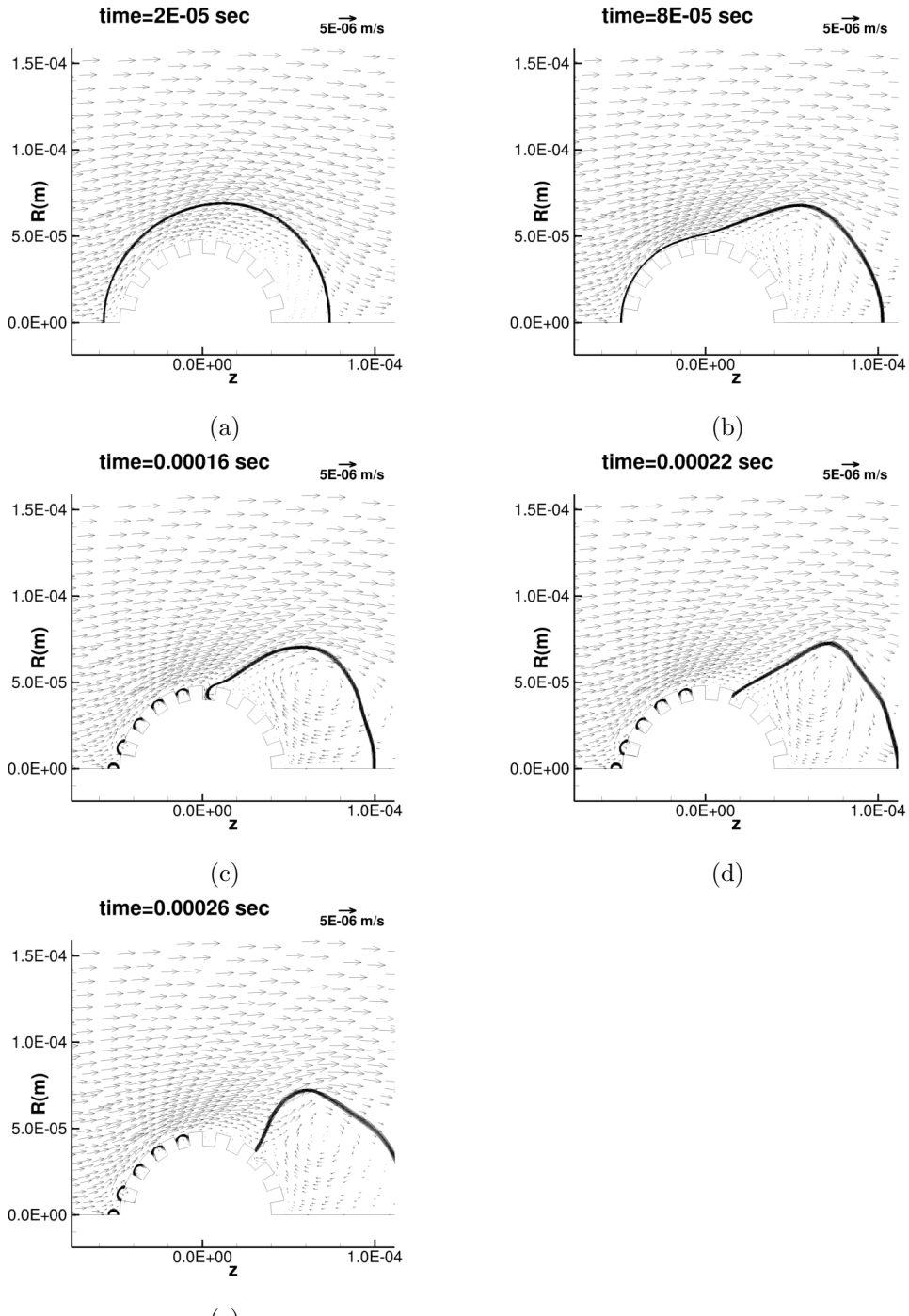

Figure 3.43: Snapshots of the vector plot of velocity at time = (a) 0.00002, (b) 0.00008, (c) 0.00016, (d) 0.00022, (e) 0.00026, predicted numerically when Re=200 at contact angle of 170 degree

Chapter 4

Conclusions and Future Work

4.1 Conclusions

A CFD-based model was provided to analyze the mechanism behind the oil-particle separation process and to understand the influencing factors in the separation process for a micro-scaled fine spherical particle. In this project, the commercial computational fluid dynamics (CFD) software ANSYS Fluent 14.5 [1] was used with 2D multi-phase modeling. The results of the VOF model for a thin-oil-film-covered spherical particle and a similar porous particle immersed in water were validated against the literature data in Bussmann et al. [2] with good agreement. The influence of two-dimensional Laminar flow regimes, model parameters (interfacial tension, thickness of oil film, physical and chemical properties of particles, chemical properties of fluids and hydrophobicity), and computational grids were studied. Based on this model, the completed separation process was predicted at different contact angles and different inlet velocities (Reynolds number). There are generally three separation stages, namely, no separation, pseudo-separation, and complete separation. In addition, the influence of porosity within the particle has been briefly investigated by using four sets of simulation.

The following are the main conclusions from this study:

- It is numerically confirmed that the greater the hydrophobicity of the contact surface (i.e. the greater the contact angle), the easier the separation process.
- When the water phase has a higher viscosity than the oil phase, the separation process occurs at lower Reynolds numbers ($\sim$0.1) when compared to normal water properties. Otherwise, the separation only happens when the Reynolds number is larger.

- There is a critical Reynolds number for each case; the separation only takes place once the critical Reynolds number is reached. In this study, at a contact angle of 90 degrees, the critical Re is 200; at the contact angle of 170 degrees, the critical Re is 5. No critical Re value was found when the contact angle was at 0 degrees due to the limitation of 2D-modeling.

- While retaining the same situation, the higher the thickness of oil film, the easier the separation.

- The pseudo-separation stage occurs as a bounce-back phenomenon. This is an uncompleted separation due to insufficient shear force.

- Since there were only four simulations for the porous particle, we cannot make a sufficiently strong conclusion on this phenomenon. However, based on the oil movement diagrams and the tendency, it is reasonable to state that the porous particle is more difficult to become fully separated from oil than the smooth solid particle.

- When the Reynolds number is too small (< 1), the oil tends to form an elongated tail first, then breakage occurs due to capillary wave instabilities.

- Potential applications can be used widely in tailings pond treatment, wastewater treatment, etc.

4.2 Future Work

The present work attempts to develop and validate the oil separation mechanism by using the VOF model, specifically, for micro-scaled particles immersed in the water phase. More work is required to elaborate on this topic.

The following areas are potential future works:

- This 2D model limits to simulations that are under Reynolds number of 200. The simulations with high Reynolds number will be studied under future 3D studies.

- Because of fewer simulations on the porous particle case, more simulations and validation cases will be done in the near future to firm the conclusions on the influence of porosity of particle.

- More validation cases against experimental data for different flow conditions should be done in the future on both smooth and rough particles.

- The changes on both pressure's sudden drop and rise between the particle and the oil film can cause the trap of certain oil portions.
- In the validation case, high water/oil viscosity ratio leads an easier separation process. The influence will be quantitatively investigated in then further.
- The influence of turbulence and modulated oscillations of the flow will be studied in detail.
- The CFD model can be run for other arbitrary shaped particles and potential applications can also be developed with additional submodel equations (including shape characteristic parameters).

Bibliography

[1] ANSYS Inc. *ANSYS Fluent Theory Guide*. ANSYS INC., 2014.

[2] S. Mehrabian, E. Acosta, and M. Bussmann. Oil–particle separation in a falling sphere configuration: Effect of oil film thickness. *Energy and Fuels*, 30(10): 8776–8786, 2016.

[3] E.S.C. Fan, M. Bussmann, and E. Acosta. Equilibrium configurations of drops attached to spheres immersed in a uniform laminar flow. *The Canadian Journal of Chemical Engineering*, 89(4):707, 2011.

[4] W.L. Oberkampf, T.G. Trucano, and C. Hirsch. Verification, validation, and predictive capability in computational engineering and physics. *Applied Mechanics Reviews*, 57(5):345–384, 2004.

[5] C.E. Lapple and C.B. Shepherd. Calculation of particle trajectories. *Industrial and Engineering Chemistry*, 32(5):605–617, 1940.

[6] A.S. Alshehry and M. Belloumi. Energy consumption, carbon dioxide emissions and economic growth: The case of saudi arabia. *Renewable and Sustainable Energy Reviews*, 41:237–247, 2015.

[7] R.G. Santos, W. Loh, A.C. Bannwart, and O.V. Trevisan. An overview of heavy oil properties and its recovery and transportation methods. *Brazilian Journal of Chemical Engineering*, 31(3):571–590, 2014.

[8] M. Seredkin, A. Zabolotsky, and G. Jeffress. In situ recovery, an alternative to conventional methods of mining: exploration, resource estimation, environmental issues, project evaluation and economics. *Ore Geology Reviews*, 79:500–514, 2016.

[9] J. Masliyah, Z.J. Zhou, Z. Xu, J. Czarnecki, and H. Hamza. Understanding water-based bitumen extraction from athabasca oil sands. *The Canadian Journal of Chemical Engineering*, 82(4):628–654, 2004.

[10] B.D. Sparks, L.S. Kotlyar, J.B. O'Carroll, and K.H. Chung. Athabasca oil sands: effect of organic coated solids on bitumen recovery and quality. *Journal of Petroleum Science and Engineering*, 39(3-4):417–430, 2003.

[11] G.D. Mossop. Geology of the Athabasca oil sands. *Science*, 207(4427):145–152, 1980.

[12] J.A. Bergerson, O. Kofoworola, A.D. Charpentier, S. Sleep, and H.L. MacLean. Life cycle greenhouse gas emissions of current oil sands technologies: surface mining and in situ applications. *Environmental science & technology*, 46(14): 7865–7874, 2012.

[13] J. Drelich, J. Hupka, J.D. Miller, and F.V. Hanson. Water recycle in moderate-temperature bitumen recovery from whiterocks oil sands. *AOSTRA Journal of Research*, 8:139–139, 1992.

[14] F. Rao and Q. Liu. Froth treatment in athabasca oil sands bitumen recovery process: A review. *Energy & Fuels*, 27(12):7199–7207, 2013.

[15] A. Shah, R. Fishwick, J. Wood, G. Leeke, S. Rigby, and M. Greaves. A review of novel techniques for heavy oil and bitumen extraction and upgrading. *Energy & Environmental Science*, 3(6):700–714, 2010.

[16] E.K. Quagraine, H.G. Peterson, and J.V. Headley. In situ bioremediation of naphthenic acids contaminated tailing pond waters in the Athabasca oil sands region-demonstrated field studies and plausible options: a review. *Journal of Environmental Science and Health*, 40(3):685–722, 2005.

[17] M.K. McNutt, R. Camilli, T.J. Crone, G.D. Guthrie, P.A. Hsieh, T.B. Ryerson, O. Savas, and F. Shaffer. Review of flow rate estimates of the deepwater horizon oil spill. *Proceedings of the National Academy of Sciences*, 109(50):20260–20267, 2012.

[18] A.M. Bernabeu, D. Rey, B. Rubio, F. Vilas, C. Dominguez, J.M. Bayona, and J. Albaiges. Assessment of cleanup needs of oiled sandy beaches: lessons from the prestige oil spill. *Environmental Science & Technology*, 43(7):2470–2475, 2009.

[19] R.A. Wuana and F.E. Okieimen. Heavy metals in contaminated soils: a review of sources, chemistry, risks and best available strategies for remediation. *Isrn Ecology*, 2011, 2011.

[20] Y. Liang, Y. Ning, L. Liao, and B. Yuan. Special focus on produced water in oil and gas fields: origin, management, and reinjection practice. *Formation Damage During Improved Oil Recovery*, pages 515–586, 2018.

[21] A. Acock, T. ORourke, D. Shirmboh, J. Alexander, G. Andersen, T. Kaneko, A. Venkitaraman, Lopez de C.J., M. Nishi, M. Numasawa, and etal. Practical approaches to sand management. *Oilfield Rev*, 16(1):10–27, 2004.

[22] Z. Grof, J. Cook, C.J. Lawrence, and F. Štěpánek. The interaction between small clusters of cohesive particles and laminar flow: Coupled dem/cfd approach. *Journal of Petroleum Science and Engineering*, 66(1):24–32, 2009.

[23] M.W. Lim, E.V. Lau, P.E. Poh, and W.T. Chong. Interaction studies between high-density oil and sand particles in oil flotation technology. *Journal of Petroleum Science and Engineering*, 131:114–121, 2015.

[24] Karl Clark. Athabasca oil sands conference in edmonton. *Clark Hot Water Extraction Process*, 1951.

[25] P. Painter, P. Williams, and E. Mannebach. Recovery of bitumen from oil or tar sands using ionic liquids. *Energy & Fuels*, 24(2):1094–1098, 2009.

[26] P.K.A. Hong, Z. Cha, X. Zhao, C. Cheng, and W. Duyvesteyn. Extraction of bitumen from oil sands with hot water and pressure cycles. *Fuel Processing Technology*, 106:460–467, 2013.

[27] John V. Fletcher, Milind D. Deo, and Francis V. Hanson. Fluidized bed pyrolysis of a uinta basin oil sand. *Fuel*, 74(3):311–316, 1995.

[28] H. Pakdel and C. Roy. Recovery of bitumen by vacuum pyrolysis of alberta tar sands. *Energy & Fuels*, 17(5):1145–1152, 2003.

[29] J. Wu and T. Dabros. Process for solvent extraction of bitumen from oil sand. *Energy & Fuels*, 26(2):1002–1008, 2012.

[30] S. Mehrabian, E. Acosta, and M. Bussmann. Oil-particle separation in a falling sphere configuration: Effect of viscosity ratio and interfacial tension. *International Journal of Multiphase Flow*, 98:120–127, 2018.

[31] G.S. Jeong, J. Lee, S. Ki, D. Huh, and C. Park. Effects of viscosity ratio, interfacial tension and flow rate on hysteric relative permeability of co2 and brine systems. *Energy*, 2017.

[32] P.G. Smith and T.G.M. Van De Ven. Shear-induced deformation and rupture of suspended solid/liquid clusters. *Colloids and Surfaces*, 15:191–210, 1985.

[33] P.G. Smith and T.G.M. Van De Ven. The separation of a liquid drop from a stationary solid sphere in a gravitational field. *Journal of Colloid and Interface Science*, 105(1):7–20, 1985.

[34] P.G. Smith and T.G.M. Van De Ven. The effect of gravity on the drainage of a thin liquid film between a solid sphere and a liquid/fluid interface. *Journal of Colloid and Interface Science*, 100(2):456–464, 1984.

[35] U.C. Bandara and P.D. Yapa. Bubble sizes, breakup, and coalescence in deep-water gas/oil plumes. *Journal of Hydraulic Engineering*, 137(7):729–738, 2011.

[36] S. Sheiko, G. Eckert, G. Ignateva, A. Muzafarov, J. Spickermann, H. R.äder, and M. Möller. Solid-like states of a dendrimer liquid displayed by scanning force microscopy. *Macromolecular Rapid Communications*, 17(5):283–297, 1996.

[37] V. Nguyen. Program impact evaluation using a matching method with panel data. *Statistics in Medicine*, 31(6):577–588, 2012.

[38] B. Xia and D.W. Sun. Applications of computational fluid dynamics (cfd) in the food industry: a review. *Computers and Electronics in Agriculture*, 34(1-3): 5–24, 2002.

[39] M. Yazdani, M.C. Soteriou, F. Sun, and Z. Chaudhry. Prediction of the thermo-fluids of gearbox systems. *International Journal of Heat and Mass Transfer*, 81:337–346, 2015.

[40] M. Griebel and M. Klitz. Clsvof as a fast and mass-conserving extension of the level-set method for the simulation of two-phase flow problems. *Numerical Heat Transfer*, 71(1):1–36, 2017.

[41] M. Sussman and E.G. Puckett. A coupled level set and volume-of-fluid method for computing 3d and axisymmetric incompressible two-phase flows. *Journal of Computational Physics*, 162(2):301–337, 2000.

[42] Y. Guo, L. Wei, G. Liang, and S. Shen. Simulation of droplet impact on liquid film with clsvof. *International Communications in Heat and Mass Transfer*, 53: 26–33, 2014.

[43] T. Gal-Chen and R. Somerville. On the use of a coordinate transformation for the solution of the navier-stokes equations. *Journal of Computational Physics*, 17(2):209–228, 1975.

[44] D. Lorenzini and Y. Joshi. Comparison of the volume of fluid and clsvof methods for the assessment of flow boiling in silicon microgaps. *Journal of Heat Transfer*, 139(11):111506, 2017.

[45] D. Li, D. Zhang, and Z. Zheng. Numerical analysis of hollow droplet impacts on a dry flat surface. *International Journal of Heat and Mass Transfer*, 129: 753–763, 2019.

[46] O. Ubbink and R.I. Issa. A method for capturing sharp fluid interfaces on arbitrary meshes. *Journal of Computational Physics*, 153(1):26–50, 1999.

[47] C. Deng, H. Wang, W. Huang, and S. Cheng. Numerical and experimental study of oil-in-water (o/w) droplet formation in a co-flowing capillary device. *Colloids and Surfaces A: Physicochemical and Engineering Aspects*, 533:1–8, 2017.

[48] Q. Wang, S. Liu, H. Wang, J. Zhu, and Y. Yang. Alginate droplets pre-crosslinked in microchannels to prepare monodispersed spherical microgels. *Colloids and Surfaces A: Physicochemical and Engineering Aspects*, 482:371–377, 2015.

[49] V.B. Patravale and S.D. Mandawgade. Novel cosmetic delivery systems: an application update. *International Journal of Cosmetic Science*, 30(1):19–33, 2008.

[50] P. Sanguansri and M.A. Augustin. Nanoscale materials development-a food industry perspective. *Trends in Food Science & Technology*, 17(10):547–556, 2006.

[51] M. Windbergs and D.A. Weitz. Microfluidics: drug dissolution chip (ddc): a microfluidic approach for drug release. *Small*, 7(21):2958–2958, 2011.

[52] Chunxia Zhao. Multiphase flow microfluidics for the production of single or multiple emulsions for drug delivery. *Advanced Drug Delivery Reviews*, 65(11-12):1420–1446, 2013.

[53] J.U. Brackbill, D.B. Kothe, and C. Zemach. A continuum method for modeling surface tension. *Journal of Computational Physics*, 100(2):335–354, 1992.

[54] X. Cai, J. Chen, M. Liu, Y. Ji, G. Ding, and L. Zhang. Cfd simulation of oil–water separation characteristics in a compact flotation unit by population balance modeling. *Journal of Dispersion Science and Technology*, 38(10):1435–1447, 2017.

[55] L. Zhao, M.C. Boufadel, S.A. Socolofsky, E. Adams, T. King, and K. Lee. Evolution of droplets in subsea oil and gas blowouts: Development and validation of the numerical model vdrop-j. *Marine Pollution Bulletin*, 83(1):58–69, 2014.

[56] T.O. Oolman and H.W. Blanch. Bubble coalescence in air-sparged bioreactors. *Biotechnology and Bioengineering*, 28(4):578–584, 1986.

[57] L. Zhao, J. Torlapati, M.C. Boufadel, T. King, B. Robinson, and K. Lee. Vdrop: A comprehensive model for droplet formation of oils and gases in liquids-incorporation of the interfacial tension and droplet viscosity. *Chemical Engineering Journal*, 253:93–106, 2014.

[58] R.H. Kraichnan. Inertial-range spectrum of hydromagnetic turbulence. *The Physics of Fluids*, 8(7):1385–1387, 1965.

[59] R.A. Antonia, B.R. Satyaprakash, and A.K.M.F. Hussain. Measurements of dissipation rate and some other characteristics of turbulent plane and circular jets. *The Physics of Fluids*, 23(4):695–700, 1980.

[60] C. Tsouris and L.L. Tavlarides. Breakage and coalescence models for drops in turbulent dispersions. *AIChE Journal*, 40(3):395–406, 1994.

[61] G. Jun, D. Gong, J. Zhang, L. Wang, Z. Zheng, and K. Li. Studies on mechanism of sand removal from crude oil. *Journal of Hydrodynamics*, 18(3):394–399, 2006.

[62] Loper M. The modeling and simulation life cycle process. *Modeling and Simulation in the Systems Engineering Life Cycle*, 2015.

[63] T. Norton and D. Sun. Computational fluid dynamics (cfd)–an effective and efficient design and analysis tool for the food industry: a review. *Trends in Food Science and Technology*, 17(11):600–620, 2006.

[64] J. Gray, D.T. Liu, M. Nieto-Santisteban, A. Szalay, D.J. DeWitt, and G. Heber. Scientific data management in the coming decade. *Acm Sigmod Record*, 34(4): 34–41, 2005.

[65] W.L. Oberkampf and T.G. Trucano. Verification and validation in computational fluid dynamics. *Progress in Aerospace Sciences*, 38(3):209–272, 2002.

[66] E.S.C. Fan, M. Bussmann, and E. Acosta. Equilibrium configurations of drops attached to spheres immersed in a uniform laminar flow. *The Canadian Journal of Chemical Engineering*, 89(4):707–716, 2011.

[67] A.D. Sommers, C. Gebhart, and C. Hermes. The role of surface wettability on natural convection frosting: Frost growth data and a new correlation for hydrophilic and hydrophobic surfaces. *International Journal of Heat and Mass Transfer*, 122:78–88, 2018.

[68] D. Lee, Y.H. Cho, J.W. Lee, and M.S. Park. Wettability of microstructured pyrex glass with hydrophobic and hydrophilic properties. *Surface and Coatings Technology*, 319:213–218, 2017.

[69] W.A. Ducker, Z. Xu, and J.N. Israelachvili. Measurements of hydrophobic and dlvo forces in bubble-surface interactions in aqueous solutions. *Langmuir*, 10 (9):3279–3289, 1994.

[70] N. Gao and Y. Yan. Modeling superhydrophobic contact angles and wetting transition. *Journal of Bionic Engineering*, 6(4):335–340, 2009.

[71] E. Sann, Y. Pan, Z. Gao, S. Zhan, and F. Xia. Highly hydrophobic zif-8 particles and application for oil-water separation. *Separation and Purification Technology*, 206:186–191, 2018.

[72] A. Sarkar and S. Mahapatra. Novel hydrophobic vaterite particles for oil removal and recovery. *Journal of Materials Chemistry*, 2(11):3808–3818, 2014.

[73] M.N. Orlin and T.G. McPoil. Plantar pressure assessment. *Physical Therapy*, 80(4):399–409, 2000.

[74] P.C. Wayner Jr. Interfacial profile in the contact line region and the young-dupre equation. *J. Colloid Interface Science*, 88(1), 1982.

[75] S.T. Ide, K. Jessen, and F.M. Orr Jr. Storage of co2 in saline aquifers: Effects of gravity, viscous, and capillary forces on amount and timing of trapping. *International Journal of Greenhouse Gas Control*, 1(4):481–491, 2007.

[76] J. Wang, Y. Zheng, and A. Wang. Effect of kapok fiber treated with various solvents on oil absorbency. *Industrial Crops and Products*, 40:178–184, 2012.

[77] R.L. Kleinberg and D.D. Griffin. Nmr measurements of permafrost: unfrozen water assay, pore-scale distribution of ice, and hydraulic permeability of sediments. *Cold Regions Science and Technology*, 42(1):63–77, 2005.